2007

Modeling Of Liquid Crystal Display And Photonic Devices

Zhibing Ge
University of Central Florida

MODELING OF LIQUID CRYSTAL DISPLAY AND PHOTONIC DEVICES

by

ZHIBING GE
B.S. in Electrical Engineering, Zhejiang University, 2002
M.S. in Electrical Engineering, University of Central Florida, 2004

A dissertation submitted in partial fulfillment of the requirements
for the degree of Doctor of Philosophy
in the School of Electrical Engineering and Computer Science
in the College of Engineering and Computer Science
at the University of Central Florida
Orlando, Florida

Fall Term
2007

Major Professors: Shin-Tson Wu

Thomas Xinzhang Wu

ABSTRACT

Liquid crystal (LC) materials have been widely applied in electro-optical devices, among which display is the most successful playground and numerous new applications in photonic areas (such as laser beam steering devices) are also emerging. To well guide the device design for optimum performance, accurate modeling is of prior and practical importance. Generally, the modeling of LC devices includes two parts in sequence: accurate LC molecule deformation extraction under external electric fields and optical calculation thereafter for the corresponding electro-optical behaviors. In this dissertation, first, hybrid finite element method and finite difference method are developed to minimize the free energy of the LC systems. In this part of study, with computer-aided derivation, the full forms of the LC free energy equations without any simplification can be obtained. Besides, Galerkin's method and weak form technique are further introduced to successfully degrade the high order nonlinear derivative terms associated with the free energy equations into ones that can be treated by first order interpolation functions for high accuracy. The developed modeling methods for LC deformation are further employed to study display structures, such as 2D and 3D in-plane switching LC cells, and provides accurate results. Followed is the optical modeling using extended Jones matrix and beam propagation method to calculate the electro-optical performances of different devices, according to their amplitude modulation property or diffractive one.

The developed methods are further taken to assist the understanding, development, and optimization of the display and photonic devices. For their application in the display area, sunlight readable transflective LCDs for mobile devices and the related optical films for wide

viewing angle are developed and studied. New cell structure using vertically aligned liquid crystal mode is developed and studied to obtain a single cell gap, high light efficiency transflective LCD that can be driven by one gray scale control circuit for both transmissive and reflective modes. And employing an internal wire grid polarizer into a fringe field switching cell produces a single cell gap and wide viewing angle display with workable reflective mode under merely two linear polarizers. To solve the limited viewing angle of conventional circular polarizers, Poincaré sphere as an effective tool is taken to trace and understand the polarization change of the incident light throughout the whole LC system. This study further guides the design of high performance circular polarizers that can consist of purely uniaxial plates or a combination of uniaxial and biaxial plates. The developed circular polarizers greatly enhance the viewing angle of transflective LCDs. Especially, the circular polarizer design using a biaxial film can even provide comparable wide viewing angle performance for the same vertically aligned cell as it is used between merely two linear polarizers, while using circular polarizers can greatly boost the display brightness.

As for the beam steering device modeling, the developed LC deformation method is taken to accurately calculate the associated LC director distribution in the spatial light modulator, while beam propagation method and Fourier transformation technique are combined to calculate the near and far fields from such devices. The modeling helps to better understand the origins and formations of the disclinations associated with the fringe fields, which further result in reduced steering efficiency and output asymmetric polarizations between positive and negative diffractions. Optimization in both voltage profile and driving methods is conducted to well tune the LC deformation under strong fringe fields and improve the light efficiency.

ACKNOWLEDGMENTS

I would like to express my gratitude to my advisors Prof. Shin-Tson Wu and Prof. Thomas X. Wu for their dedicated guidance, inspiration, and patience throughout this work. I appreciate and treasure the opportunity to work with them and grow under their guidance.

I would also like to thank my colleagues in the photonics and display group at CREOL, especially Dr. Xinyu Zhu, Dr. Robert Lu, and Dr. Hyang-Yul Kim, for their valuable discussions, and for making themselves available whenever necessary during this work. Without their technical supports, this work would not be so smooth.

Additionally, I would like to thank Toppoly Optoelectronics (Taiwan), Raytheon Company (Boston, MA), and Chi-Mei Optoelectronics (Taiwan) for their financial support of my study and research here at University of Central Florida. Here I would specially thank Dr. Chung-Kuang Wei and Dr. Wang-Yang Li from CMO, and Dr. Terry Dorschner and Dr. Irl Smith from Raytheon for their consistent support and encouragement during my work.

Finally, I would like to express my gratitude to my parents and my wife. They always selflessly offer supports to me, no matter how long and how far I have been away from them.

TABLE OF CONTENTS

LIST OF FIGURES

LIST OF TABLES

CHAPTER 1: INTRODUCTION

Liquid crystal (LC) materials have been used widely in direct-view and projection displays, such as computer monitors and LCD TVs, and photonic devices, such as spatial light modulators and beam steering devices. Accurate and reliable modeling of LC electro-optic behaviors is critical in developing novel display and photonic devices and optimizing the present ones. Generally, the LC modeling includes two steps: evaluation of the LC directors' deformation under external electric fields and calculation of the optical properties thereafter. In this thesis, we will first introduce the numerical methods for both LC director deformation calculation and the related optical calculation, then apply these methods to develop and optimize novel LC devices, such as sunlight readable transflective LCDs for display applications and spatial light modulators (SLM) for laser beam steering.

As a prerequisite for reliable device design and subsequent optical analysis, the dynamic modeling of the LC director formations can be implemented by finite difference method (FDM)[1, 2], finite element method (FEM)[3, 4], or a combination of both. These methods have demonstrated their success in accurate modeling of LC devices. Presently, several groups have been working in the liquid crystal modeling software development, such as LC3D[2], DIMOS[5], LCD Master[6], Techwitz LCD[7], LCD-DESIGN[8], LCQuest[9], and others.

Among various methods, the increasing complexity of LC device structures makes the FEM a good candidate for efficient solvers, owing to its versatility in modeling arbitrary structures with adaptive meshing technique. Further, as a direct solver, this method can generate accurate solutions from solving large sparse matrix system. Since efficient algorithms for large

sparse matrix system in other areas such as mathematics, mechanics, and electromagnetics are well developed, they can be introduced to the LC device modeling without much extra effort. In addition, as the computer aided symbolic derivation techniques are being more and more maturely developed, the automatic FEM formula derivations in LC simulations have become possible, which were previously the main obstacles to introduce FEM into LC modeling. Several publications have already exploited the FEM in the study of advanced LC devices[10-16]. However, approximation in the FEM formulations is usually taken and their focus is more device physics oriented. To the best of our knowledge, no literature has ever reported a comprehensive mathematical derivation and formulation of the FEM in LCD modeling. The lack of accurate, detailed and open-source FEM derivations and formulations in LCD simulators has hindered the research as well as applications of LCD technologies. Therefore, one of the major objectives of this work is to propose a comprehensive accurate dynamic modeling of LC deformations by FEM. In addition, a special technique, the weak form to greatly simplify derivations while maintaining accuracy, is introduced as well. Several examples of current display devices are studied with the derived method.

Following the deformation modeling, we further studied the optical characterization of liquid crystal devices with pre-knowledge of the director distribution. According to distinct device characteristics, such as display devices or beam steering devices, different optical modeling methods need to be considered. Basically, for display applications, the liquid crystal cell along with two linear polarizers usually works as a means of optical valve to obtain amplitude modulation for different gray levels. Therefore the polarization change of the light throughout the liquid crystal cell is of interest. On the other hand, in some beam steering devices,

the liquid crystal cell works as a phase modulator in periodic structures, thus the phase change profile and diffraction patterns of the light through the liquid crystal cell is of prior importance. In this section, the extended Jones matrix method is studied to characterize display devices. And, for modeling the diffractive typed devices, we introduced the beam propagation method (BPM)[17, 18], which can account for the transverse variation of LC directors, to calculate the near field of the incident laser beam. Combined with Fourier transformation, we can further obtain the far-field diffraction patterns.

With the preparations of the numerical methods, we investigated designing and optimizing novel display and photonic devices, such as developing high performance sunlight readable transflective LCDs and its related optical films, and modeling a multi-electrode spatial light modulator for laser beam steering and boosting its steering efficiency.

With the merit of sunlight readability, low power consumption, compact size, and light weight, transflective LCD is one of the most successful display technologies for mobile devices. Usually a transflective LCD device combines a transmissive region and a reflective region in each pixel area to have both functions simultaneously. In such devices, one of the major challenges is to develop a single cell gap structure that can have high transmittance and reflectance, as well as a good overlap between the voltage dependent transmittance and reflectance curves (which is preferred for driving the cell with a single gray-scale controller). We have developed several TFT LC cells to achieve this target. The example illustrated in this thesis is a transflective LCD using a vertically aligned LC cell with patterned reflectors that are commonly biased with certain voltages.

Another important requirement for the transflective LCDs is the need for wide viewing

angles. Conventionally, the viewing angle is limited by the inclusion of circular polarizers. Understanding this issue, we conducted our researches from two directions: 1) designing wide-viewing angle transflective LCDs without using circular polarizers, and 2) developing high performance wide-viewing angle circular polarizers. For the first direction, the challenge is the difficulty to design a reflective mode with good dark state. We proposed a solution by combing fringe-field switching (FFS, an inherently wide-viewing angle LC mode) LC mode[20] for the transmissive part and an internal wire grid polarizer[21] for the reflective part in a transflective LCD. On the other direction, with the assistance of Poincaré sphere[22, 23] to trace the polarization of incident light throughout the LC system, we developed several new circular polarizers that greatly enhance the viewing angle of a transflective LCDs using a vertically aligned LC cell. We believe these works will greatly benefit the display technology.

For the laser beam steering, a spatial light modulator with periodic multi-electrode phase ramps[24, 25, 26] is studied with our developed modeling methods. The major issue of SLM structure using LC material is the existence of strong fringe fields that generate LC disclinations for non-desired phase profiles, which greatly impairs the steering efficiency. As real a laser beam steering system usually takes a cascade structure that employs several separate SLMs to have omni-directional scanning capability, the efficiency of each single SLM becomes critical. In this section, we applied our modeling tools to analyze the detailed LC deformation in such structures and proposed optimization methods to improve the steering efficiency. Besides, we also introduced a special driving method to guide the reorientation of LC molecules under external electric fields, which successfully reduces the chance for disclination formations and boost up the efficiency.

In this work, the numerical modeling of LC devices for both LC director deformation and optical characterization are systematically investigated and developed. With the assistance of these methods, the physics and optics of LC devices are better understood. Besides, these methods are applied to developing and optimizing novel devices, such as transflective LCDs and laser beam steering devices. We believe this work associated with the LC device modeling and the novel device and system development will greatly benefit the display and photonics area.

1. 1. References

1. A. Taflove, "Computational Electrodynamics: The Finite-Difference Time-Domain Method," Artech House Publishers, (1995).
2. J. E. Anderson, P. Watson, P. J. Bos, "LC3D: Liquid Crystal Display 3-D Directory Simulator, Software and Technology Guide," Artech House Publishers, (1999).
3. J. Jin, "The Finite Element Method in Electromagnetics," 2nd Edition, Wiley-IEEE Press, (2002).
4. Y. W. Kwon and H. Bang, "The finite element method using MATLAB," CRC Press, (2000).
5. Autronic-MELCHERS GmbH, available: http://www.autronic-melchers.com/index.htm
6. SHINTECH. Inc., available: http://www.shintech.jp/eng/index_e.html
7. SANAYI System Co., Ltd., available: http://www.sanayisystem.com/introduction.html
8. V. G. Chigrinov, H. S. Kwok, D. A. Yakovlev, G. V. Simonenko, V. I. Tsoy, " Invited Paper: LCD Optimization and Modeling," SID Symp. Dig., 28.1, pp. 982-985, (2004).
9. LCQuest, available: http://www.eng.ox.ac.uk/lcquest/

10. J. B. Davies, S. E. Day, F. Di Pasquale, and F. A. Fernandez, “Finite-element modeling in 2-D of nematic liquid crystal structure,” Electron. Lett., vol. 32, pp. 582-583, (1996).
11. F. Di Pasquale, F. A. Fernandez, S. E. Day, et al. “Two-dimensional finite-element modeling of nematic liquid crystal devices for optical communications and displays,” IEEE J. Select. Topics Quantum Electron., vol. 2 , pp.128-134, (1996).
12. F. A. Fernandez, S. E. Day, P. Trwoga, H. F. Deng, and R. James, “Three-dimensional modeling of liquid crystal display cells using finite elements,” Mol. Cryst. Liq. Cryst., vol. 375, pp. 291-299, (2002).
13. F. A. Fernandez, H. F. Deng, and S. E. Day, “Dynamic modeling of liquid crystal display cells using a constant charge approach,” IEEE Trans. on Magn., vol. 38, pp. 821-824, (2002).
14. H. J. Yoon, J. H. Lee, M. W. Choi, J. W. Kim, O. K. Kwon, and T. Won, “Comparison of numerical methods for analysis of liquid crystal cell: in-plane switching,” SID Symp. Dig., 50.1, pp. 1378-1381, (2003).
15. S. H. Yoon, C. S. Lee, S. I. Yoon, J. H. Lee, H. J. Yoon, M. W. Choi, J. W. Kim, and T. Won, “Three-dimensional numerical simulation for understanding the fringe field effect on the dynamic behavior of liquid crystal,” Mol. Cryst. Liq. Cryst., vol. 413, pp. 333/[2469]-343/[2479], (2004).
16. Yao, J. J. Wu, and S. H. Chen, “Three-dimensional simulation of the homeotropic to planar transition in cholesteric liquid crystals using the finite elements method,” Jpn. J. Appl. Phys., vol. 43, pp. 705-708, (2004).
17. E. E. Kriezis and S. J. Elston, “A wide angle beam propagation method for the analysis of

tilted nematic liquid crystal structures," J. Mod. Opt. 46, 1201–1212 (1999).

18. E. E. Kriezis and S. J. Elston, "Wide-Angle Beam Propagation Method for Liquid-Crystal Device Calculations," Appl. Opt. 39, 5707-5714 (2000).
19. X. Zhu, Z. Ge, T. X. Wu, and S. T. Wu, "Transflective liquid crystal displays," J. Display Technology 1, 15 (2005).
20. S.H. Lee, S. L. Lee, and H. Y. Kim, "Electro-optic characteristics and switching principle of a nematic liquid crystal cell controlled by fringe-field switching," Appl. Phys. Lett. 73, 2881 (1998).
21. S. T. Wu, "Reflective and transflective liquid crystal display using a wire grid polarizer," U. S. Patent 6,977,702 B2 (2005).
22. S. Huard, *Polarization of Light* (Wiley, New York, 1997).
23. X. Zhu, Z. Ge, and S. T. Wu, "Analytical solutions for uniaxial-film-compensated wide-view liquid crystal displays," J. Display Technology 2, 2-20 (2006).
24. T. A. Dorschner and D. P. Resler, "Deflector for an optical beam," US Pat. No. 4,964,701, (Oct. 1990).
25. T. A. Dorschner et al, "Liquid crystal beam steerig: an optical phase array for lasers," presented at the *1991 Meet. IRIS Specialty Group on Active Syst.*, (Oct. 1991).
26. D. P. Resler, D. S. Hobbs, R. C. Sharp, L. J. Friedman, and T. A. Dorschner, "High-efficiency liquid-crystal optical phased-array beam steering," Opt. Lett. 21, 689 (1996).
27. P. F. McManamon, T. A. Dorschner, D. L. Corkum, L. J. Friedman, D. S. Hobbs, M. Holz, S. Liberman, H. Q. Nguyen, D. P. Resler, R. C. Sharp, and E. A. Watson, "Optical phased array technology," Proc. IEEE 84, 268-298 (1996).

CHAPTER 2: MODELING OF LIQUID CYSTAL DEFORMATION AND OPTICS

2. 1. Liquid Crystal Deformation Modeling

In this section, we first introduce the theory and derivation of update equations for LC director and potential profiles, as well as the iteration scheme associated with the dynamic process. Then, FEM is employed to solve the above derived highly nonlinear equations based on the Galerkin's method1[1] for director profile and Ritz's method[1] for potential profile. Derivations of the nonlinear equations show that the highest order spatial derivative is in the second order (e.g., $\frac{\partial^2}{\partial x \partial y}$). Therefore, we apply the weak form method[1] to degrade these update equations into first order partial different equations. This technique makes the first order 3D FEM interpolation function (tetrahedron shaped) accurate enough. To verify our derivations, a 2D in-plane-switching (IPS) structure[2] is then studied by the above-derived method, and results are compared with the FEM-based software 2dimMOS[3]. Finally, a 3D super IPS structure with zigzag electrodes[4] is simulated using our FEM and results are verified by those derived from FDM.

2. 1. 1. Theory and Mathematical Formulation

2. 1. 1. 1. Dynamic Vector Model of Liquid Crystal Directors

Modeling of the dynamic process of LC directors in response to external voltages

generally starts from minimizing the Gibbs free energy[5] within the LC cell. However, owing to the high nonlinearity of the free energy expressions of LC and the coupling between kinetic and electric energies, a direct solution of the LC director deformation from the free energy equation is almost impossible. Therefore, the dynamic modeling usually involves an iteration process[6]: minimizing the Gibbs free energy to update the LC director profile and solving the Gauss law (or minimizing the electric energy) to update the potential profile interactively. In modeling the LC directors, both vector representation[7], as shown in Fig. 2.1, and Q tensor[8, 9, 10] methods can be employed. Detailed comparison of these two methods is provided in Ref. 6. Owing to its mathematical simplicity, fast computing speed, and reliability, the vector method is widely employed in LCD simulations. In this work, we also employ the vector method in the detailed derivations.

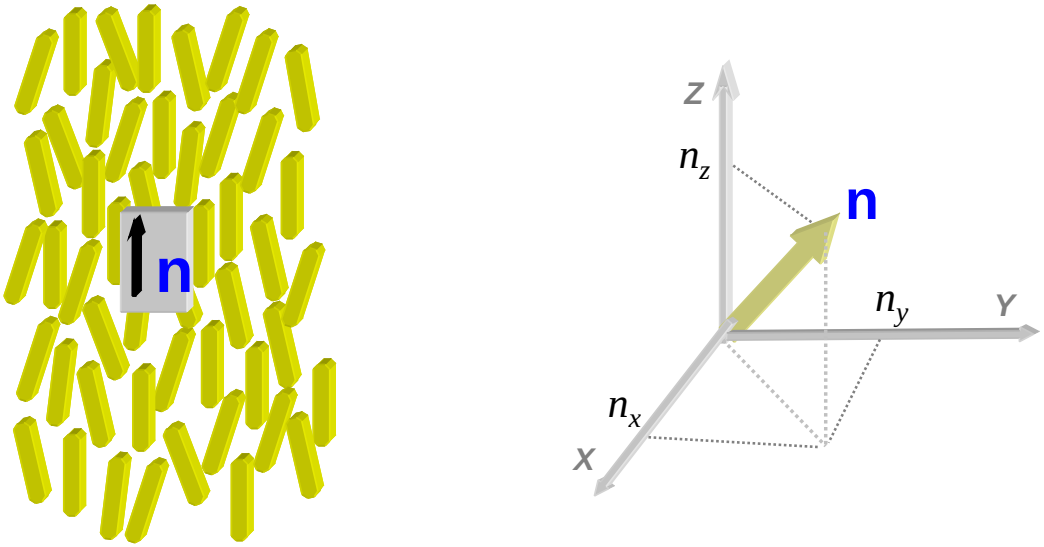

Figure 2.1: Vector representation of a LC director

2. 1. 1. 2. Director Profile Update Theory

Numerically simulation of LC transient state at each time step under constant voltage is based on minimizing Gibbs free energy by solving the Euler Lagrange equation[5, 6]. The Gibbs free energy includes both Frank-Oseen free energy density[11, 12, 13] and the electric energy density in the LC cell can be expressed as

$$f = \frac{1}{2}K_{11}(\nabla \cdot \mathbf{n})^2 + \frac{1}{2}K_{22}(\mathbf{n} \cdot \nabla \times \mathbf{n} + q_0)^2 + \frac{1}{2}K_{33}|\mathbf{n} \times \nabla \times \mathbf{n}|^2 - \frac{1}{2}\mathbf{D} \cdot \mathbf{E}, \quad (1)$$

where

$$\mathbf{D} = \varepsilon_0 \vec{\varepsilon}\mathbf{E}, \quad (2)$$

$$\mathbf{E} = -\nabla\Phi, \quad (3)$$

and $\mathbf{n} = (n_x, n_y, n_z)$ is the unit vector form of LC directors in the given coordinates, as shown in Fig. 2. 1; q_0 is the chiral wave number, which is a parameter specifying the equilibrium twist state of the LC; K_{11}, K_{22}, and K_{33} are the elastic constants of the LC materials; and **D**, **E**, Φ are the electric displacement, electric field, and potential function in the entire system region, respectively; $\vec{\varepsilon}$ is the dielectric tensor of LC which correlates **D** and **E**. It is known that minimizing the above free energy by solving Euler Lagrange equation will result in[5, 6]

$$\left(\frac{\partial f}{\partial n_l} - \frac{d}{dx}\frac{\partial f}{\partial(dn_l/dx)} - \frac{d}{dy}\frac{\partial f}{\partial(dn_l/dy)} - \frac{d}{dz}\frac{\partial f}{\partial(dn_l/dz)}\right) = -\gamma\frac{dn_l}{dt}, \quad (4)$$

where n_l represents n_x, n_y, and n_z. The unit length of the LC director $n_x^2 + n_y^2 + n_z^2 = 1$ should be enforced at each iteration step. Here the flow effects are ignored. Equation (4) specifies the iterative relation of LC directors under external applied voltages, which can be further simplified as the following form

$$\frac{dn_l}{dt}+\frac{1}{\gamma}[f]_{n_l}=0 \quad (l = x, y, z), \tag{5}$$

where

$$[f]_{n_l}=\left(\frac{\partial f}{\partial n_l}-\frac{d}{dx}\frac{\partial f}{\partial(dn_l/dx)}-\frac{d}{dy}\frac{\partial f}{\partial(dn_l/dy)}-\frac{d}{dz}\frac{\partial f}{\partial(dn_l/dz)}\right). \tag{6}$$

By taking a time-difference $\frac{dn_l}{dt}=\frac{n_l^{t+\Delta t}-n_l^t}{\Delta t}$, Eq. (5) can be further expressed as

$$n_l^{t+\Delta t}=n_l^t-\frac{\Delta t}{\gamma}[f]_{n_l} \quad (l = x, y, z). \tag{7}$$

Since the dielectric tensor $\tilde{\varepsilon}$ includes the LC director $\mathbf{n}=(n_x,n_y,n_z)$, the potential and the director functions in $[f]_{n_l}$ are coupled with each other as indicated by Eqs. (1)-(3). Computer assisted derivations show $[f]_{n_l}$ has a highly nonlinear form containing the highest spatial derivative of n_l with respect to *x, y,* and *z* up to the second order (e.g., $\frac{\partial^2 n_l}{\partial x\partial y}$). In order to use the first order 3D tetrahedral basis function (which has the simplest form with least number of variables for fast computing) to evaluate these second order derivatives, weak form method is introduced, as will be discussed later.

2. 1. 1. 3. Potential Profile Update Theory

At any given LC director distribution profile and fixed electrode voltage, the potential profile Φ can be determined by solving the Gauss law

$$\nabla\cdot\mathbf{D}=0. \tag{8}$$

The displacement D can be expressed by the potential Φ as indicated in Eqs. (2) and (3). Here solving the above equation is equivalent to minimizing the electric energy $F_e = \int_{\Omega} \frac{1}{2} \mathbf{D} \cdot \mathbf{E} d\Omega$ in the bulk from the variational principle. The bulk region defined here includes the LC cell and other regions, such as the substrates. Both direct solver (e.g., FEM with Ritz's method or Galerkin's method) and iterative approach (e.g., FDM with iterations) can be applied to solve the desired potential profile. Due to the simplicity in implementation and the inherited accuracy of direct solver, we will take FEM with Ritz's method in the following derivations.

2. 1. 1. 4. Dynamic Modeling Flowchart

As explained in Sections 2.1.1.2 and 2.1.1.3, the coupling between director and potential profiles makes it almost impossible to get a direct solution of the stable profile. However, this challenge can be overcome by the iteration approach. A detailed iterative flowchart is illustrated in Fig. 2.2. The initial LC director profile can usually be set by its boundary conditions. The stability of this iterative updating scheme is an important issue[14], which relies on a proper selection of updating time step Δt in Eq. (7).

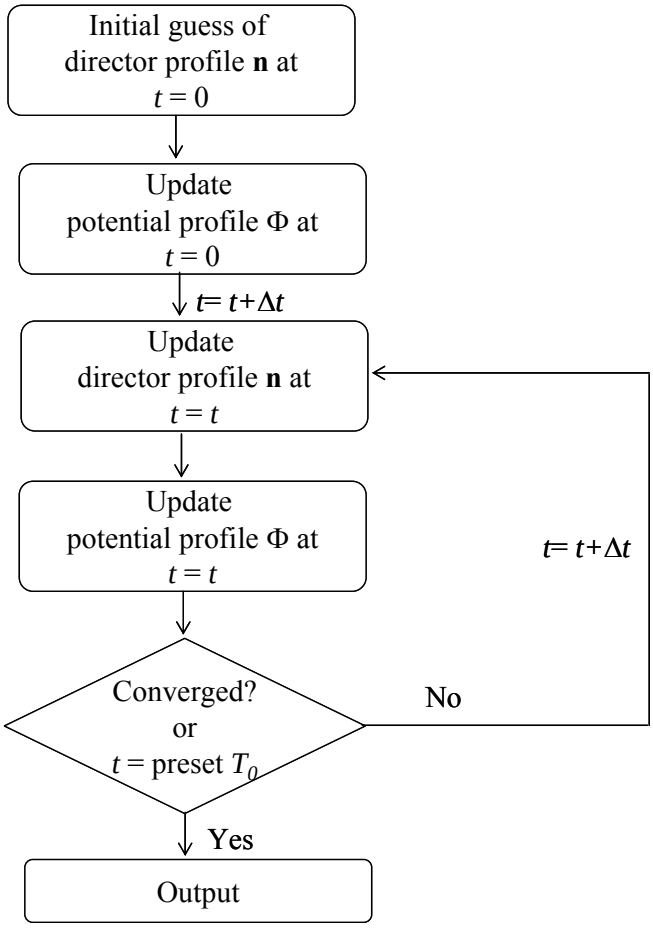

Figure 2.2: Iteration flow chart of the dynamic modeling

2. 1. 2. Finite Element Formulations

The solution for the abovementioned iteration scheme includes two steps: 1) solving the potential distribution at a given director profile, and 2) solving the director profile at a given potential distribution. The FEM is employed to derive these iteration formulations.

2. 1. 2. 1. Galerkin's Method for Director Update

The high nonlinearity of Eq. (1) indicates that direct minimization is difficult to obtain. However, Galerkin's method can bypass this difficulty. The Galerkin's method belongs to the family of weighted residual methods, which seek the solution by weighting the residual of the differential equations. Suppose we divide the study region Ω into M element regions with N nodes (applied with the first order interpolation function). Each local element can be a specific shape, such as a tetrahedral block in the 3D FEM case. The general solution of each director component n_x, n_y, or n_z can be approximated by interpolating from the N global node values using global interpolation functions as

$$\tilde{n}_l = \sum_{j=1}^{N} n_{l,j} W_j \qquad (l = x, y, z), \tag{9}$$

where $\tilde{n}_l$ is the approximate solution of n_l. $n_{l,j}$ and W_j are the j-th node value of n_l and interpolation function in the entire region, respectively. The specific form of W_j will be discussed later. After inserting $\tilde{n}_l$ into Eq. (5), the residual R, error of the interpolation, can be written as

$$R = \frac{d\tilde{n}_l}{dt} + \frac{1}{\gamma}[f]_{n_l} \quad (l = x, y, z). \tag{10}$$

The exact solution occurs only when R equals to 0. Due to the above approximation, the residual R always leads to a nonzero value. However, as a routine, with Galerkin's method, the residual R can be minimized through weighting the residual R by interpolation function W_j as

$$\int_{\Omega} \left(\frac{d\tilde{n}_l}{dt} + \frac{1}{\gamma}[f]_{n_l} \right) W_i d\Omega = 0 \quad (i = 1,2,\cdots N \text{ and } l = x, y, z). \tag{11}$$

Here, $\int_{\Omega} d\Omega$ denotes the integral on the study domain Ω, which can be 1D to 3D integrals for different problems. Replacing the $\tilde{n}_l$ by Eq. (9) yields

$$\int_{\Omega} \left(\frac{d\left(\sum_{j=1}^{N} n_{l,j} W_j \right)}{dt} + \frac{1}{\gamma} [f]_{n_l} \right) W_i d\Omega = 0 \quad (i = 1,2,\cdots N \text{ and } l = x, y, z). \tag{12}$$

For each n_l (l =x, y, z), we can obtain N linear equations with N variables $n_{l,j}$ by expanding Eq. (12), which can be further expanded as

$$\sum_{j=1}^{N} \left(\int_{\Omega} W_i W_j d\Omega \right) \frac{dn_{l,j}}{dt} = -\int_{\Omega} \frac{1}{\gamma} [f]_{n_l} W_i d\Omega \quad (i = 1,2,\cdots N \text{ and } l = x, y, z). \tag{13}$$

This equation group can be further written in a matrix form as

$$[A]\left(\frac{dn_l}{dt} \right) = (b) \quad (l = x, y, z), \tag{14}$$

where [ ] denotes a matrix and ( ) denotes a vector, with

$$A_{i,j} = \int_{\Omega} W_i W_j d\Omega, \tag{15}$$

and

$$b_i = -\int_{\Omega} \frac{1}{\gamma} [f]_{n_l} W_i d\Omega. \tag{16}$$

By taking the same forward time-difference scheme $\frac{dn_l}{dt} = \frac{n_l^{t+\Delta t} - n_l^t}{\Delta t}$ as Eq. (7), we can obtain the iteration relation via Galerkin's method as

$$\left(n_l^{t+\Delta t} \right) = \left(n_l^t \right) + \Delta t [A]^{-1} (b) \quad (l = x, y, z). \tag{17}$$

Equation (17) is the final iteration relation of the dynamic model. It shows that once the LC director distribution at a previous time step t (i.e., n_l^t) is known, the director distribution at the next time step $t+\Delta t$ (i.e., $n_l^{t+\Delta t}$) can be obtained with the matrix A and vector b known from the previous time step.

However, the abovementioned matrix A and vector b is still not easy to obtain, because a group of interpolation function W can be defined on the entire domain and it is difficult to assign their appropriate forms. However, the FEM can help to select a good group of interpolation functions.

FEM can be employed to get the solutions for the matrix A and vector b. In the FEM theory, a study domain Ω can be divided into M element domains with N nodes. In each small element domain, there are m nodes with m interpolation functions (first order) as well. In any element domain (e.g., e-th element) the local director value n_l^e can be interpolated by its m local node values using m local basis functions as

$$\tilde{n}_l^e = \sum_{i=1}^{m} n_{l,i}^e W_i^e \quad (l = x, y, z). \tag{18}$$

where $n_{l,i}^e$ and W_i^e are the i-th node value and interpolation function in the e-th local element, respectively. Different from the above general analysis of Galerkin's method, the form of W_i^e can be well-defined. For example, the first order basis function in a 3D tetrahedral element would be

$$W_i^e(x, y, z) = a_i^e + b_i^e x + c_i^e y + d_i^e z \quad (i = 1,2,\cdots m). \tag{19}$$

The coefficients a_i^e, b_i^e, c_i^e, and d_i^e can be determined by the node coordinate values and the volume of the tetrahedron [1]. Detailed expressions of these coefficients are provided in Ref. 1.

Similarly, the residual R_e in each element domain Ω_e can be weighted by the element basis function as

$$\int_{\Omega^e}\left(\frac{d\tilde{n}_l^e}{dt}+\frac{1}{\gamma}\left[f\right]_{n_l}^e\right)W_i^e d\Omega^e=0 \quad \left(i\ =\ 1,\ 2,\ \cdots\ m \text{ and } l\ =\ x, y, z\right). \tag{20}$$

Expanding the above equation with a time-difference scheme leads to

$$\left(n_l^e\right)^{t+\Delta t}=\left(n_l^e\right)^t+\Delta t\left[A^e\right]^{-1}\left(b^e\right) \qquad \left(l=x,y,z\right), \tag{21}$$

where

$$A_{i,j}^e=\int_{\Omega^e}W_i^e W_j^e d\Omega^e, \tag{22}$$

and

$$b_i^e=-\int_{\Omega^e}\frac{1}{\gamma}\left[f\right]_{n_l}^e W_i^e d\Omega^e. \tag{23}$$

By applying the typical assembling process of typical FEM procedure, the global matrix A and global vector b in Eq. (14) can be obtained from the element matrix A_e and element vector b_e. Consequently, under given specific boundary conditions, one can obtain the solution of $\tilde{n}_l$.

The advantage of this method is evident that the global matrix A in Eq. (14) is uniquely determined by the mesh and the forms of interpolation functions, as indicated in Eq. (22). As a result, in updating director profiles from Eq. (17), the matrix A only needs to be calculated at the first iteration step and can be stored for subsequent iteration steps. Utilizing this property greatly reduces the computing time in the director updating procedure.

2. 1. 2. 2. Ritz's Method for Potential Update

From the analysis of the potential update theory, the update of potential is equivalent to solve the Gaussian law of Eq. (8), or minimizing the system electric energy $F_e = \int_{\Omega} \frac{1}{2} \mathbf{D} \cdot \mathbf{E} d\Omega$ from a variational viewpoint. Since the variational form of Eq. (8) is well established, both Galerkin's method and Ritz's method can be employed to solve the desired potential profile provided that the initial director profile is given. However, the physical and mathematical meanings of the Ritz's method are more apparent than those of Galerkin's method. Therefore, we use the Ritz's method in the following potential update formulation derivations.

The free electric energy F_e in the study domain is equal to

$$F_e = \int_{\Omega} \frac{1}{2} \mathbf{D} \cdot \mathbf{E} d\Omega = \int_{\Omega} \frac{1}{2} \varepsilon_0 \left(\vec{\varepsilon} \nabla \Phi \right) \cdot \left(\nabla \Phi \right) d\Omega . \tag{24}$$

Here for those anisotropic media, such as LC layer, $\vec{\varepsilon}$ is a tensor; however, for isotropic materials, such as the glass substrate, it is a scalar. Similarly, the approximate global potential solution $\tilde{\Phi}$ can be expressed by the global node value Φ_j and global interpolation function W_j as

$$\tilde{\Phi} = \sum_{j=1}^{N} \Phi_j W_j \quad . \tag{25}$$

F_e is a function of N global variables Φ_j ($j = 1, 2, \cdots N$), here N could be different with the total node number in the director update. From mathematical theory, its value is minimized where the relative partial derivative of F_e with respect to each Φ_j equals to zero. This leads to N equations

$$\frac{\partial F_e}{\partial \Phi_j} = 0 \qquad (j = 1, 2, \cdots N). \tag{26}$$

This equation group can be further expressed as a matrix representation:

$$[B](\Phi) = (0) \cdot \tag{27}$$

Again, here [] denotes a matrix and ( ) denotes a vector. To derive the definite form of the matrix *B*, we first express the electric field **E** into a vector form as

$$\mathbf{E} = -\left(\frac{\partial \Phi}{\partial x}, \frac{\partial \Phi}{\partial y}, \frac{\partial \Phi}{\partial z}\right)^T . \tag{28}$$

Therefore, the free electric energy F_e can be further expressed as

$$F_e = \frac{1}{2}\varepsilon_0 \int_\Omega \left(\frac{\partial \Phi}{\partial x}, \frac{\partial \Phi}{\partial y}, \frac{\partial \Phi}{\partial z}\right)\left(\vec{\vec{\varepsilon}}\left(\frac{\partial \Phi}{\partial x}, \frac{\partial \Phi}{\partial y}, \frac{\partial \Phi}{\partial z}\right)^T\right) d\Omega . \tag{29}$$

A detailed check of F_e form reveals that it is a quadratic function of the Φ's spatial derivative. Therefore once the $\tilde{\Phi}$ in Eq. (25) is substituted in Eq. (29), the derivative of F_e with respect to Φ_i can be achieved by differentiation in part

$$\frac{\partial F_e}{\partial \Phi_i} = \frac{1}{2}\varepsilon_0 \int_\Omega \left(\frac{\partial W_i}{\partial x}, \frac{\partial W_i}{\partial y}, \frac{\partial W_i}{\partial z}\right)\left(\vec{\vec{\varepsilon}}\left(\frac{\partial \Phi}{\partial x}, \frac{\partial \Phi}{\partial y}, \frac{\partial \Phi}{\partial z}\right)^T\right) d\Omega$$

$$+ \frac{1}{2}\varepsilon_0 \int_\Omega \left(\frac{\partial \Phi}{\partial x}, \frac{\partial \Phi}{\partial y}, \frac{\partial \Phi}{\partial z}\right)\left(\vec{\vec{\varepsilon}}\left(\frac{\partial W_i}{\partial x}, \frac{\partial W_i}{\partial y}, \frac{\partial W_i}{\partial z}\right)^T\right) d\Omega \qquad (i = 1, 2, \cdots N) . \tag{30}$$

From above equation, each element $B_{i,j}$ of matrix B in Eq. (27) can be obtained by differentiating the Eq. (30) with respect to Φ_j:

$$B_{i,j} = \frac{\partial^2 F_e}{\partial \Phi_i \partial \Phi_j} \qquad (i, j = 1, 2, \cdots N). \tag{31}$$

Substituting Eq. (30) to Eq. (31) yields

$$B_{i,j} = \frac{1}{2}\varepsilon_0 \int_{\Omega} \left(\frac{\partial W_i}{\partial x}, \frac{\partial W_i}{\partial y}, \frac{\partial W_i}{\partial z} \right) \left(\vec{\varepsilon} \left(\frac{\partial W_j}{\partial x}, \frac{\partial W_j}{\partial y}, \frac{\partial W_j}{\partial z} \right)^T \right) d\Omega$$

$$+ \frac{1}{2}\varepsilon_0 \int_{\Omega} \left(\frac{\partial W_j}{\partial x}, \frac{\partial W_j}{\partial y}, \frac{\partial W_j}{\partial z} \right) \left(\vec{\varepsilon} \left(\frac{\partial W_i}{\partial x}, \frac{\partial W_i}{\partial y}, \frac{\partial W_i}{\partial z} \right)^T \right) d\Omega . \qquad (32)$$

Here for the nematic LC material, the tensor $\vec{\varepsilon}$ is a symmetric matrix. This symmetric property can further simplify $B_{i,j}$ to the following form:

$$B_{i,j} = \varepsilon_0 \int_{\Omega} \left(\frac{\partial W_i}{\partial x}, \frac{\partial W_i}{\partial y}, \frac{\partial W_i}{\partial z} \right) \left(\vec{\varepsilon} \left(\frac{\partial W_j}{\partial x}, \frac{\partial W_j}{\partial y}, \frac{\partial W_j}{\partial z} \right)^T \right) d\Omega . \qquad (33)$$

However, we still need to select an appropriate group of the global interpolation functions W to get the definite matrix element $B_{i,j}$. Similarly, to select an appropriate group of interpolation functions, we also refer to the FEM.

By applying the similar mesh and derivation as discussed in the FEM implementation of director profile section, we can obtain the element matrix B^e for each element, which has m nodes and m basis functions. The $B^e_{i,j}$ can be written as

$$B^e_{i,j} = \frac{\partial^2 F_e^e}{\partial \Phi_i^e \partial \Phi_j^e} = \frac{1}{2}\varepsilon_0 \int_{\Omega^e} \left(\frac{\partial W_i^e}{\partial x}, \frac{\partial W_i^e}{\partial y}, \frac{\partial W_i^e}{\partial z} \right) \left(\vec{\varepsilon} \left(\frac{\partial W_j^e}{\partial x}, \frac{\partial W_j^e}{\partial y}, \frac{\partial W_j^e}{\partial z} \right)^T \right) d\Omega^e$$

$$+ \frac{1}{2}\varepsilon_0 \int_{\Omega^e} \left(\frac{\partial W_j^e}{\partial x}, \frac{\partial W_j^e}{\partial y}, \frac{\partial W_j^e}{\partial z} \right) \left(\vec{\varepsilon} \left(\frac{\partial W_i^e}{\partial x}, \frac{\partial W_i^e}{\partial y}, \frac{\partial W_i^e}{\partial z} \right)^T \right) d\Omega^e \quad (i, j = 1,2,\cdots m). \qquad (34)$$

From the above equation, one can get a definite $B^e_{i,j}$ value once W_i^e and the coordinate values of the small local domain Ω^e are specified, as illustrated in Ref. 1. By applying the assembling

process of FEM, the global matrix B can be obtained from the element matrix B_e. With specific boundary conditions, the potential profile at given director profile can be directly calculated from Eq. (27).

2. 1. 2. 3. Weak Form and Boundary Conditions

As explained in above sections, the global matrix A, B for director and potential calculations have specific forms and can be directly obtained from their corresponding equations using FEM. Still, the difficulty lies in the derivations of global vector b in Eq. (16), which has a quite complex form. Although approximation of the derivations can be applied[15], still its accuracy in some complex device structures is not guaranteed. However, the state-of-the-art computer software can help to generate FEM based formulation derivations. We find the highest order of spatial derivative of n_l with respect to x, y, and z is up to the second order. Therefore the first order of interpolation/basis function (e.g., Eq. (19)) will lose accuracy due to the fact that it makes terms with second order spatial derivative equal to zero. For example, assume there is one term $\iiint_{\Omega^e} \beta \frac{\partial^2 n_l^e}{\partial x \partial z} W_i^e \, dxdydz$ in b_i^e. After substituting $\tilde{n}_l^e = \sum_{j=1}^{m} n_{l,j}^e W_j^e$ into b_i^e with the first order interpolation function W_j^e, the second order derivative $\frac{\partial^2 n_l^e}{\partial x \partial z}$ leads this term to zero, which does not always hold.

A good solution of this issue is to introduce the weak form method. Derivations of Eq. (6) based on commercial software show that $[f]_{n_l}$ can be summarized as a general expression:

$$[f]_{n_l} = [f_0]_{n_l} + \sum f^l_{i,j,k} \frac{\partial^2 n_i}{\partial j \partial k} \qquad (l,i,j,k = x,y,z). \tag{35}$$

where $[f_0]_{n_l}$ stands for the terms with highest derivatives up to the first order, $f^l_{i,j,k} \frac{\partial^2 n_i}{\partial j \partial k}$ denotes these second order derivative terms (e. g., $f^l_{z,x,x} \frac{\partial^2 n_z}{\partial x \partial x}$), and $f^l_{i,j,k}$ is the coefficient of these second order derivatives. Now we rewrite Eq. (16) in the following form:

$$b = -\frac{1}{\gamma} \iiint_{x,y,z} [f]_{n_l} W dx dy dz . \tag{36}$$

Substituting Eq. (35) into Eq. (36) yields

$$b = -\frac{1}{\gamma} \left(\iiint_{x,y,z} [f_0]_{n_l} W dx dy dz + \iiint_{x,y,z} \sum f^l_{i,j,k} \frac{\partial^2 n_i}{\partial j \partial k} W dx dy dz \right) \qquad (l,i,j,k = x,y,z). \tag{37}$$

In Eq. (37), the first term with derivatives up to first order can be calculated by FEM with first order interpolation function forms *W*. In the left part, although there are many terms with second order derivatives, they can be divided into two categories: 1) either *j* or *k* equals to *z*, and 2) neither *j* nor *k* equals to *z*. As an illustration of taking the weak form in simplifying Eq. (37), we just take two typical terms from these two categories: 1) $\iiint_{x,y,z} f^l_{x,y,z} \frac{\partial^2 n_x}{\partial y \partial z} W dx dy dz$, and 2) $\iiint_{x,y,z} f^l_{z,x,y} \frac{\partial^2 n_z}{\partial x \partial y} W dx dy dz$. Using integration by part, we obtain

$$\iiint_{x,y,z} f^l_{x,y,z} \frac{\partial^2 n_x}{\partial y \partial z} W dx dy dz = -\iiint_{x,y,z} \frac{\partial n_x}{\partial y} \frac{\partial \left(f^l_{x,y,z} W \right)}{\partial z} dx dy dz + \iint_{x,y} \left(\frac{\partial n_x}{\partial y} f^l_{x,y,z} W \right) \Bigg|_{z=0}^{z=z_d} dx dy \ , \tag{38}$$

and

$$\iiint_{x,y,z} f^{l}_{z,x,y} \frac{\partial^2 n_z}{\partial x \partial y} W dx dy dz = -\iiint_{x,y,z} \frac{\partial n_z}{\partial x} \frac{\partial \left(f^{l}_{z,x,y} W \right)}{\partial y} dx dy dz + \iint_{x,z} \left(\frac{\partial n_z}{\partial x} f^{l}_{z,x,y} W \right) \Big|_{y=0}^{y=y_d} dx dz \ , \tag{39}$$

where z_d and y_d denote the boundary coordinates in the vertical (z) and lateral (y) directions. Because the director $\mathbf{n} = \left(n_x, n_y, n_z \right)$ is fixed under strong anchoring assumption in the vertical (z) direction, i.e., $\frac{\partial n_l^e}{\partial i} = 0 \ \ (i = x, y, z)$ at these boundaries, the 2D integral term in Eq. (38) equals to zero. This property further simplifies Eq. (38) into

$$\iiint_{x,y,z} f^{l}_{x,y,z} \frac{\partial^2 n_x}{\partial y \partial z} W dx dy dz = -\iiint_{x,y,z} \frac{\partial n_x}{\partial y} \frac{\partial \left(f^{l}_{x,y,z} W \right)}{\partial z} dx dy dz , \tag{40}$$

which makes $\iiint_{x,y,z} f^{l}_{x,y,z} \frac{\partial^2 n_x}{\partial y \partial z} W dx dy dz$ calculable by the first order interpolation functions using FEM. On the other hand, the 2D integral term $\iint_{x,z} \left(\frac{\partial n_z}{\partial x} f^{l}_{z,x,y} W \right) \Big|_{y=0}^{y=y_d} dx dz$ in Eq. (39) might not be zero on the boundaries in the y direction. However, as illustrated in Fig.2.3, the term $\iint_{x,z} \left(\frac{\partial n_z}{\partial x} f^{l}_{z,x,y} W \right) \Big|_{y=0}^{y=y_d} dx dz$ in Eq. (39) can be further expressed at $y = 0$ and $y = y_d$ planes by

$$\iint_{x,z} \left(\frac{\partial n_z}{\partial x} f^{l}_{z,x,y} W \right) \Big|_{y=0}^{y=y_d} dx dz = \iint_{x,z} \left(\frac{\partial n_z}{\partial x} f^{l}_{z,x,y} W \left(x, y = y_d, z \right) \right) dx dz$$

$$- \iint_{x,z} \left(\frac{\partial n_z}{\partial x} f^{l}_{z,x,y} W \left(x, y = 0, z \right) \right) dx dz . \tag{41}$$

The 3D interpolation function $W(x, y, z)$ decays to a 2D interpolation function on the boundary planes (x-z plane at $y = 0$ and $y = y_d$ in this case), as shown in Figs. 2.4(b) and 2.4(c). To evaluate this term, we need to use 2D FEM on the lateral boundary planes to solve Eq. (41).

This is equivalent to weight $\frac{\partial n_z}{\partial x} f^{l}_{z,x,y}$ on the boundary planes (x-z plane at $y = 0$ and $y = y_d$ in this case) by 2D FEM with 2D interpolation functions generated from $W(x, y, z)$. The lateral derivative terms in x and y directions (e. g., $\frac{\partial n_z}{\partial x}$) can be calculated by a finite difference from the boundary point and its neighboring ones (e.g., $\left.\frac{\partial n_z}{\partial x}\right|_{x=0} = \frac{n_z(x=\Delta x) - n_z(x=0)}{\Delta x}$), or in a periodic boundary condition, we can take a more accurate form as $\left.\frac{\partial n_z}{\partial x}\right|_{x=0} = \frac{n_z(x=\Delta x) - n_z(x=(N-1)\Delta x)}{2\Delta x}$, since $n_z(x=0) = n_z(x=N\Delta x)$. With the assistance of FEM, these 2D integral terms can also be calculated. Other second order terms in Eq. (37) can be calculated similarly in the same way as Eqs. (38) – (41).

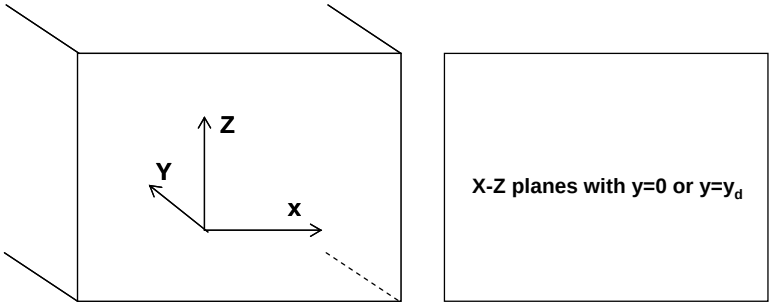

Figure 2.3: 2D boundary planes from a 3D bulk.

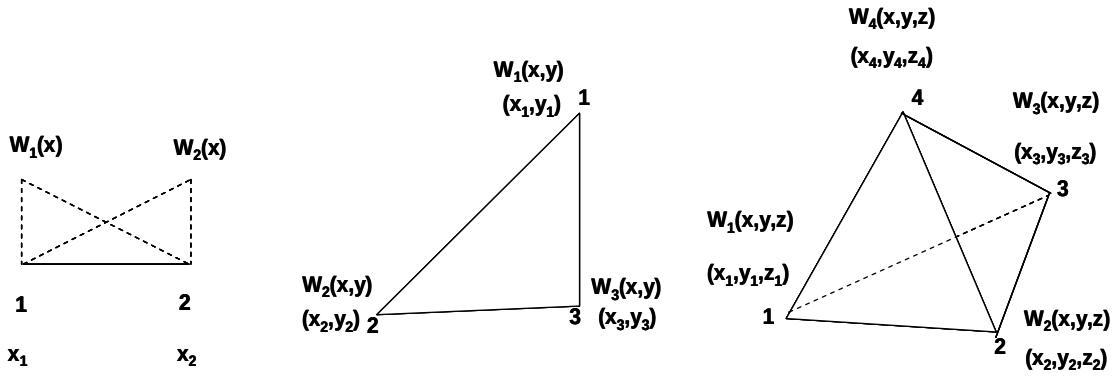

(a) (b) (c)

Figure 2.4: (a) 1D, (b) 2D, and (c) 3D interpolation functions

In other words, by taking the weak form method into derivations of Eq. (16), these second order derivative terms will degrade into the first order ones, which can be calculated by using the first order interpolation functions. Therefore, introducing the weak form greatly facilitates the derivation of vector *b* without any further approximations to sacrifice simulation accuracy.

In solving the LC director and potential profiles, their boundary conditions in the study cell need to be well-defined. As shown in Fig. 2.5, typical boundary conditions for the potential are the Dirichlet boundary conditions on electrodes, i.e., the potential values on electrodes 1 and 2 are fixed to constant voltages. In the far regions along the *z* direction, such as the outer boundaries of the supporting substrates where no electrodes are present, the Neumann condition applies to the potential, i.e., the spatial normal derivative of potential (e.g., $\frac{\partial \Phi}{\partial z}$) equals to zero. In the implementation of these boundary conditions for the potential, the fixed values on the

electrodes can be forced by matrix and vector manipulation in Eq. (27), and the Neumann conditions for potential in the far regions will naturally satisfied in FEM with the assumption that the electric energy is totally confined in the LC cells as well as the substrate regions.

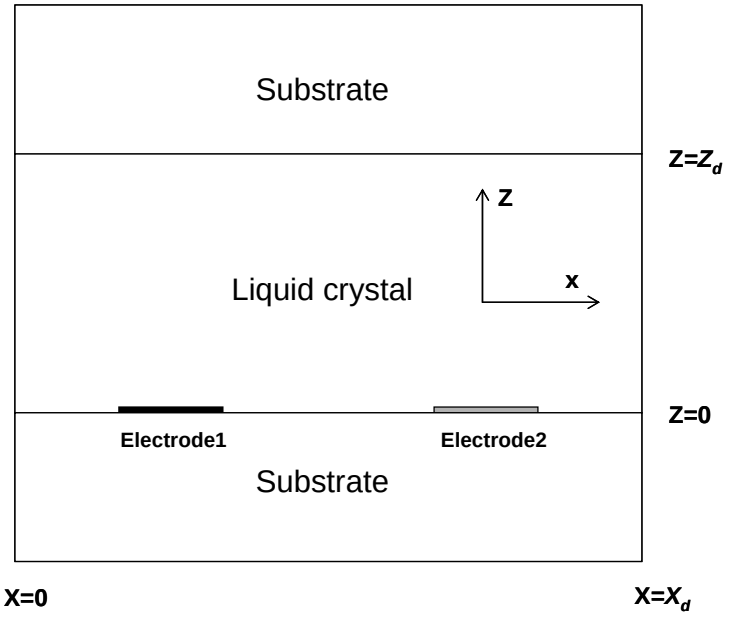

Figure 2.5: A conventional 2D in-plane switching structures

For the LC director calculations, in the vertical direction (z direction), the director $\mathbf{n} = (n_x, n_y, n_z)$ on the top and bottom alignment layer–LC interfaces (at $z = 0$ and $z = z_d$) are usually specified by initial pretilt and azimuthal angle values. With strong anchoring assumption, the director values on these interfaces are fixed. A more general case is to take the surface anchoring energy into consideration. The surface anchoring energy density (J/m^2) from the Rapini-Papoular model[16, 17] should be merged into the Gibbs free energy density (J/m^3) in Eq. (1), while their units should be manipulated to keep same. The surface anchoring energy density on

the vertical boundaries has the following forms:

$$F_s = \frac{1}{2} C_\theta \sin^2(\theta - \theta_r) + \frac{1}{2} C_\Phi \sin^2(\Phi - \Phi_r), \tag{42}$$

where C_θ and C_Φ are the polar and azimuthal anchoring energy coefficients (J/m^2), θ_r and Φ_r are the pretilt polar angle and twist angle, respectively. Equation (42) can be further expanded and expressed by the director components $\mathbf{n} = (n_x, n_y, n_z)$ as

$$F_s = \frac{1}{2} C_\theta \left[n_z^2 \cos^2\theta_r + (1 - n_z^2) \sin^2\theta_r - n_z \sqrt{1 - n_z^2} \sin 2\theta_r \right]$$

$$+ \frac{1}{2} C_\Phi \left[\frac{n_y^2}{1 - n_z^2} \cos^2\Phi_r + \frac{n_x^2}{1 - n_z^2} \sin^2\Phi_r - \frac{n_x n_y}{1 - n_z^2} \sin 2\Phi_r \right]. \tag{43}$$

In the lateral direction (x, y direction), $\mathbf{n} = (n_x, n_y, n_z)$ can be determined by Dirichlet boundary conditions, i.e., the $\mathbf{n} = (n_x, n_y, n_z)$ values are fixed, or by Neumann conditions, i.e., $\frac{\partial n_l^e}{\partial i} = 0$ $(i, l = x, y, z)$ at lateral boundary planes, which is determined by specific device configurations. Another type of lateral boundary condition frequently employed in LCD simulation is the periodic boundary condition. The director $\mathbf{n} = (n_x, n_y, n_z)$ and its derivatives have equal values at two lateral periodic boundaries, such as planes at $x = 0$ and $x = x_d$ in Fig. 2.5. Because the LC cell patterns in the pixel are usually periodically repeated in some devices such as in the IPS mode, the calculation results from one period are enough to represent the entire pixel. The periodic boundary condition greatly reduces the computing load in simulating large size pixels.

Those abovementioned boundary conditions are most widely employed in the LC device

simulations. However, boundary conditions for the potential and director update are not confined to these categories. Instead, they need to be designated in accordance to the specific problems studied.

2. 1. 3. Results and Discussion

To illustrate and validate the FEM-based LC dynamic modeling with the above derived formulations, we use a 2D interdigital IPS structure with rectangular electrodes as an example to compare our own developed method with the FEM-based commercial software 2dimMOS. In addition, we use a 3D super IPS with zigzag electrodes to compare our method with the FDM.

2. 1. 3. 1. Two-dimensional IPS Structure

Figure 2.5 depicts a conventional 2D IPS structure. The LC material employed is MLC-6692 (from Merck) with its parameters listed as follows: $n_e = 1.5644$, $n_o = 1.4794$, $\varepsilon_{//} = 14.2$, $\varepsilon_{\perp} = 4.2$, $K_{11} = 9.6$ pN, $K_{22} = 6.1$ pN, $K_{33} = 14.1$ pN, and rotational viscosity $\gamma_1 = 0.1$ Pa·s. The LC cell gap is 4 μm, the LC pretilt angles on both substrates are 2^o, and the rubbing angles are 80^o away from the *x* axis in the *x*-*y* plane. In Fig. 2.5, the electrodes 1 and 2 are located in the same bottom plane at $z = 0$, with an equal width of 4 μm and a separation distance of 8 μm.

In the simulation, the electrode 1 is applied with 6 V_{rms}, and the electrode 2 is grounded. The LC directors on the vertical boundaries are assumed to be strongly anchored in our simulations. The x direction periodic boundary conditions in Fig. 2.5 are applied to both potential and LC director calculations. In the 2dimMOS, since no periodic boundary conditions are

available, we just expand two more periods in both left and right x directions to approximate the periodicity in the 2dimMOS (a total of five periods). Here we use the center-truncated region (one period) from the 2dimMOS to compare with our simulation based on the derived method in this chapter.

Figures 2.6(a) and 2.6(b) plot the director distribution at 4 ms and 16 ms with 6 V_{rms} applied voltage, respectively. Apparently, the effect of director tilt deformation near the interdigital electrode side regions becomes more and more evident as the time changes from 4 ms to 16 ms. The twist deformation effect in the inter-electrode regions also shows the same tendency. The transmittance dependence on different x positions at 4 ms, 8 ms, 12 ms, and 16 ms are plotted in Fig. 2.7. At t = 16 ms, the transmittance in the curve almost reaches the maximum value which is 35% under real crossed polarizers. Due to the structure symmetry, the directors in the regions above each electrode's surface have little twist in response to the electric fields at different times, which results in dark lines above these regions. As we can see from this figure, they have a very good agreement, which verifies the accuracy of our derivations.

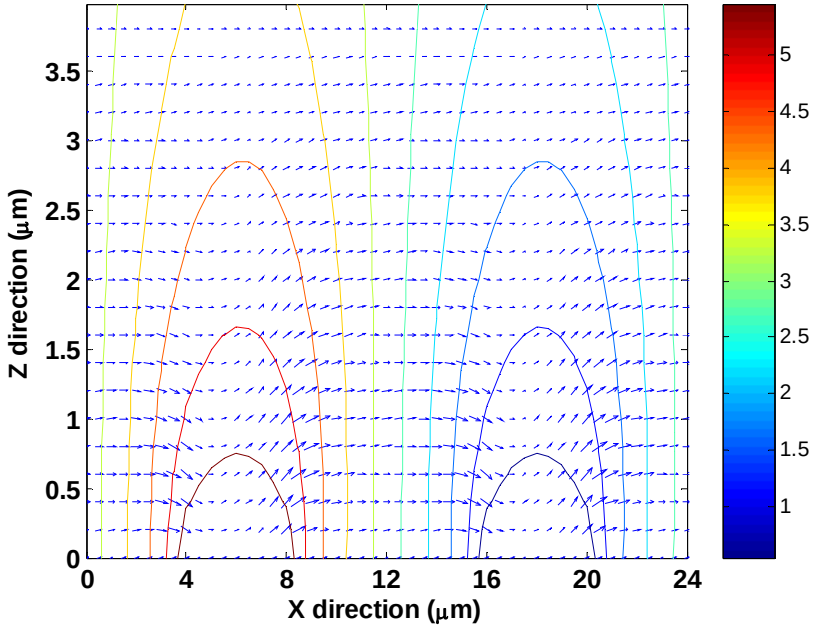

(a)

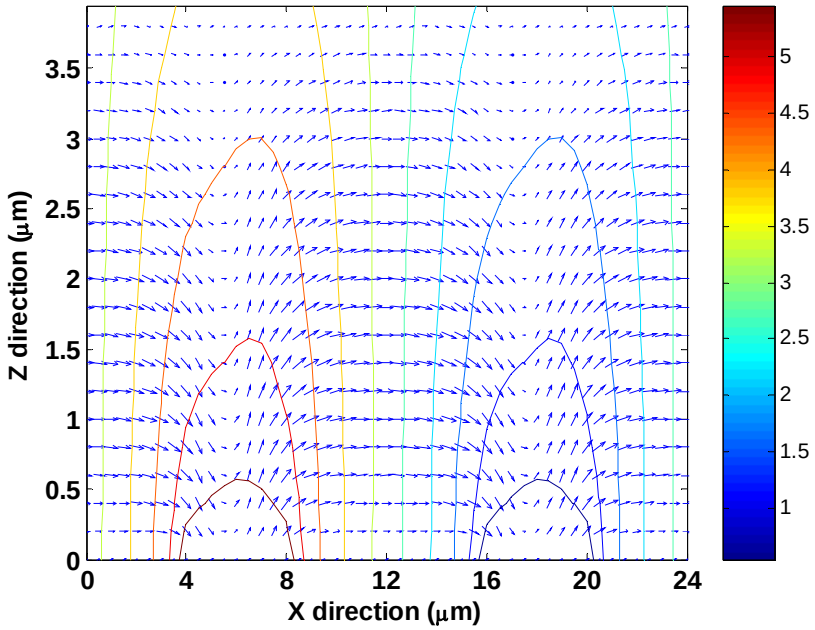

(b)

Figure 2.6: (a) LC director distribution at 4 ms and (b) at 16 ms with 6 V_{rms} applied.

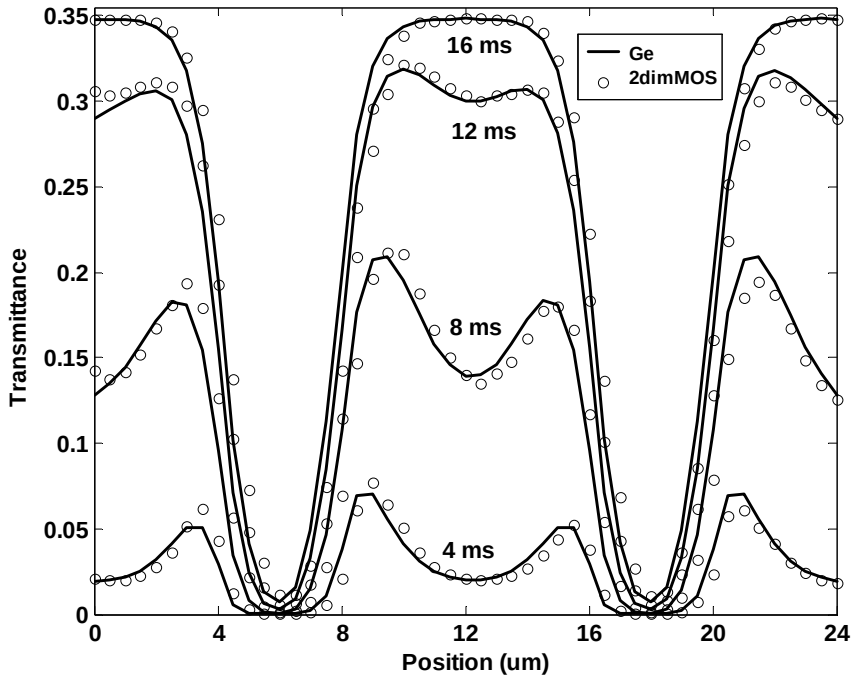

Figure 2.7: Transmittance versus position at time equal to 4 ms, 8 ms, 12 ms, and 16 ms from the derived FEM based method and the 2dimMOS.

2. 1. 3. 2. Three-dimensional Super IPS Structure

The super IPS structure with zigzag electrodes is then simulated by both derived FEM and FDM. The electrode shape and dimension in the bottom *x-y* plane is shown in Fig. 2.8. And the cross-section view of the cell in *x-z* plane is same as Fig. 2.5. In our simulation, same LC material and cell gap as the 2D simulation is taken in this structure. The pretilt angles of LC directors are 2^o from the x-y plane, and the rubbing angles are 90^o away from the x axis in the x-

y plane. 6 V_{rms} are applied on the left electrode, while the right one is grounded to 0 V_{rms}. The LC directors on the vertical boundaries (in *z* direction) are assumed to be strongly anchored in our simulations. Figure 2.8 only shows a single period of the electrode structure within a pixel. The periodic boundary conditions in the lateral directions (both in *x* and *y* directions) is employed in both potential and LC director calculations.

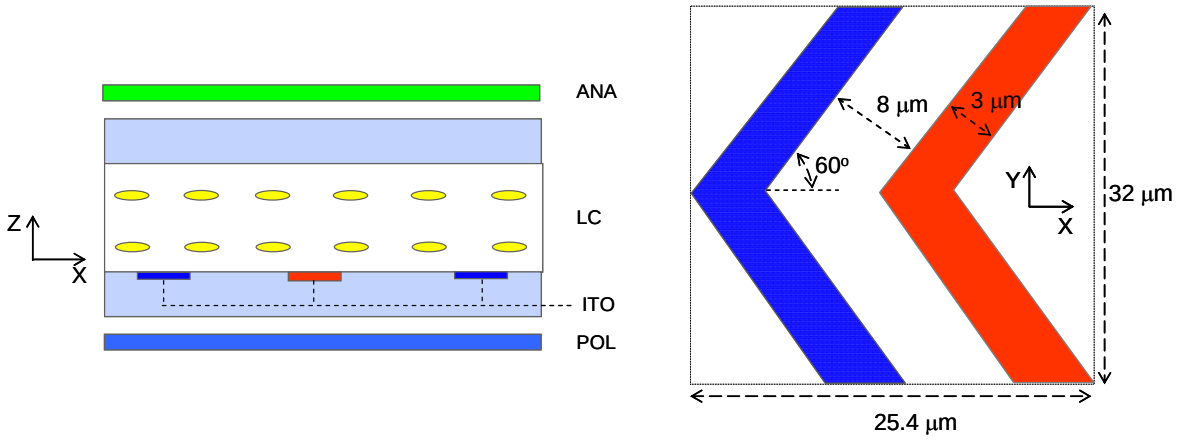

Figure 2.8: Super IPS structure with zigzag electrodes in simulation.

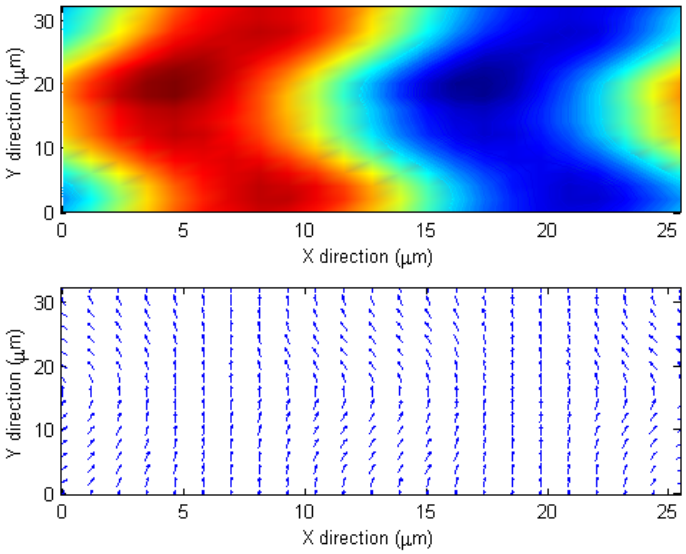

(a)

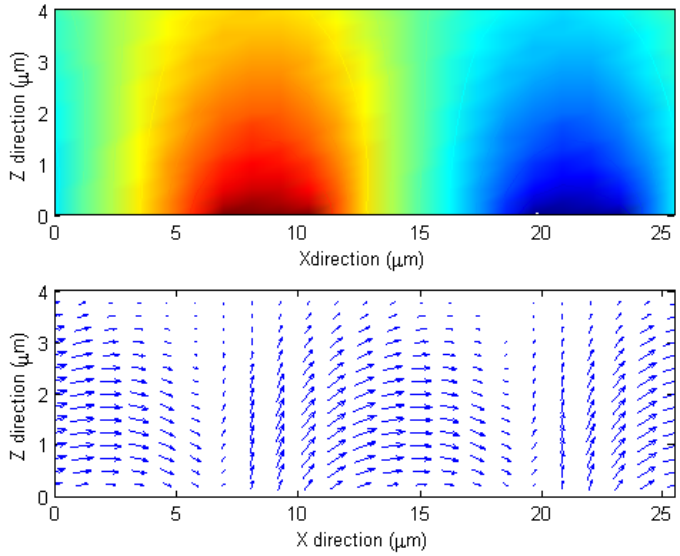

(b)

Figure 2.9: LC potential (top figure) and director (bottom figure) distributions with 6 V_{rms} at t =15 ms in (a) *x*-*y* plane at z = 3 μm and (b) *x*-*z* plane at y = 4 μm.

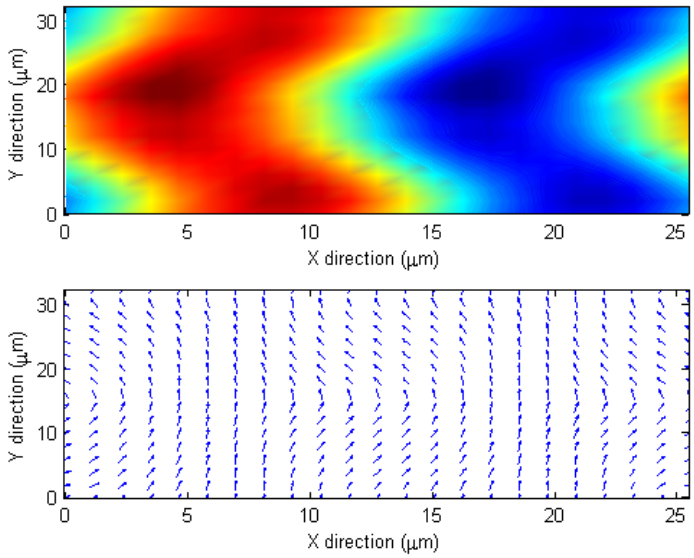

(a)

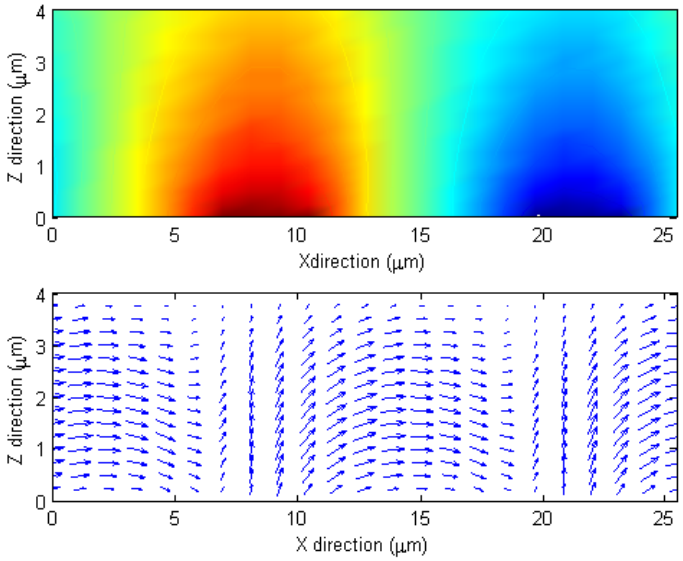

(b)

Figure 2.10: LC potential (top figure) and director (bottom figure) distributions with 6 V_{rms} at t = 60 ms in (a) x-y plane at z = 3 μm and (b) x-z plane at y = 4 μm.

Figures 2.9(a) and 2.9(b) show the cross-section view of the potential and director distributions at t = 15 ms and 60 ms, respectively. In sampling the cross-section view of *x*-*y* plane, the *z* is taken at $z = 3$ μm, and $y = 4$ μm is taken for the sampling of *x*-*z* cross-section view. As we can see from these figures, the LC directors in the regions between the electrodes have been driven to the parallel direction of electric fields in these regions at t = 15 ms. And no much difference is observed for t = 15 ms and t = 60 ms. However, it takes a long time for the directors above the electrode surface to be rotated, as seen from t = 15 ms (Figs. 2.9(a) and 2.9(b)) and t = 60 ms (Figs. 2.10(a) and 2.10(b)). This is because the electric fields above the electrodes are more vertically distributed (z direction), while the electric fields in the inter-electrode regions are mostly along the horizontal direction. The less rotation in these regions generates dark regions as illustrated in Figs. 2.11(a) to 2.11(c).

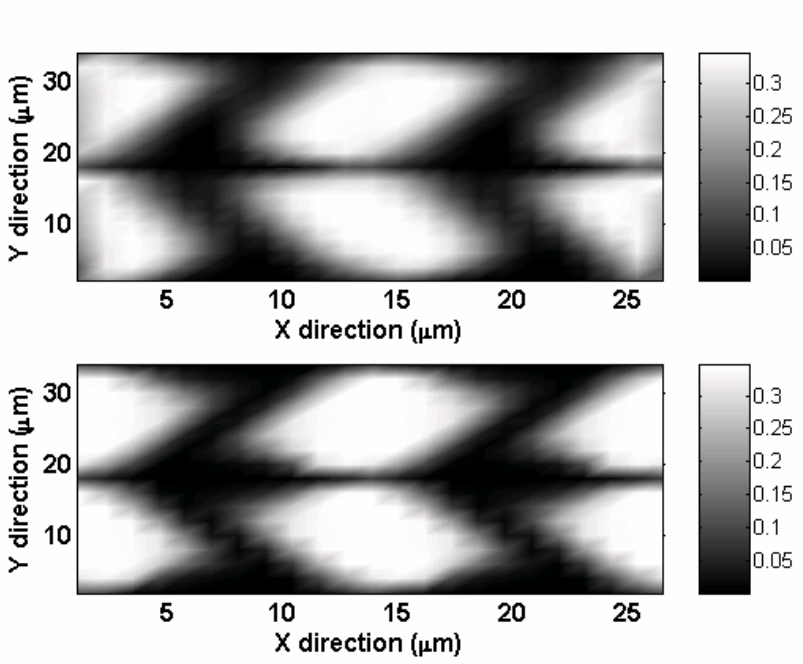

(a)

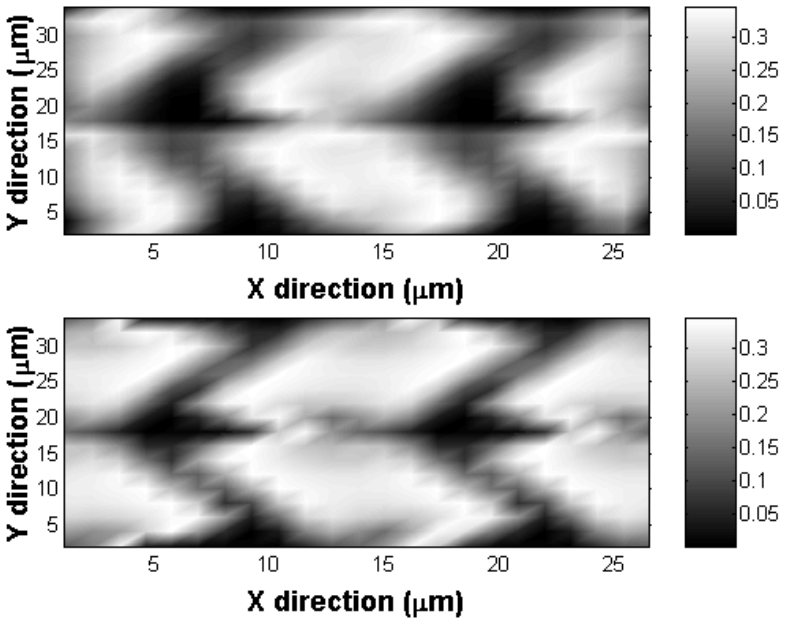

(b)

Figure 2.11: (a). The transmittance pattern in the *x*-*y* plane by FEM (top figure) and FDM (bottom figure) with 6 V_{rms} at (a) t = 15 ms and (b). t = 40 ms.

Figures 2.11(a) to 2.11(b) show the transmittance patterns at different time steps of t = 15 ms and 40 ms from the derived FEM (top) and FDM (bottom). It can be seen that these two methods generate almost the same transmittance patterns. The main discrepancy of these two method comes from the center positions of electrodes (at y = 16 μm), where the electrode angle is very sharp. The FEM and FDM might generate different LC director orientations, i.e., at these positions the LC director might rotate either in the –x direction or in the +x direction. However, in other regions, the results of these two methods match well with each other. Both methods show that the vertically distributed electric fields above the electrodes make these regions have

relative low transmittances. Here the asymmetric dark region patterns in the y direction originate from the 2^{o} pretilt angle in the *y*-*z* plane.

In addition to IPS structure described above, the derived method is also applicable to other complex LCD structures, such as multi-domain vertical alignment (MVA)[18] and patterned vertical alignment (PVA)[19] modes.

2. 2. Optical Modeling for Liquid Crystal Devices

Optical characterization of liquid crystal devices with pre-knowledge of the director distribution is another important aspect of the modeling. Basically, for display applications, the liquid crystal cell is sandwiched between two linear polarizers, usually they together work as a means of optical valve to obtain amplitude modulation for different gray levels. Therefore the polarization change of the light throughout the liquid crystal cell is of major interest. On the other hand, in some beam steering devices, such as a spatial light modulator, the liquid crystal cell works as a phase modulator and the phase change profile of the light through the liquid crystal cell is of prior importance. Accordingly, appropriate optical theory and method should be chosen to address their different characteristics. Presently, matrix form based method, such as Jones matrix method[20-24], 4×4 matrix method[25-28], are typically employed for display applications. Beam propagation method (BPM)[29, 30], finite difference in time domain (FDTD) method[31-32] are usually taken for diffraction problems in liquid crystal devices.

2. 2. 1. Optical Methods for Liquid Crystal Displays

For a liquid crystal display device, its electro-optic properties such as voltage-dependent transmittance/reflectance, iso-contrast for display viewing angle, angular dependent light leakage/brightness, and angular dependent gray-level plots, etc., are of great interest and importance to characterize its performance. The system configuration of a typical transmissive LCD and a reflective LCD are illustrated in Fig. 2.12(a) and 2.12(b). For the transmissive typed LCD, the liquid crystal layer is sandwiched between two linear polarizers, and incident light comes from the backlight unit on a different side of the viewer. For the reflective LCD, the liquid crystal layer is interposed between a single polarizer and a reflector (usually a metal mirror), and the incident light impinges on the display from the ambient, that is on the same side as the viewer.

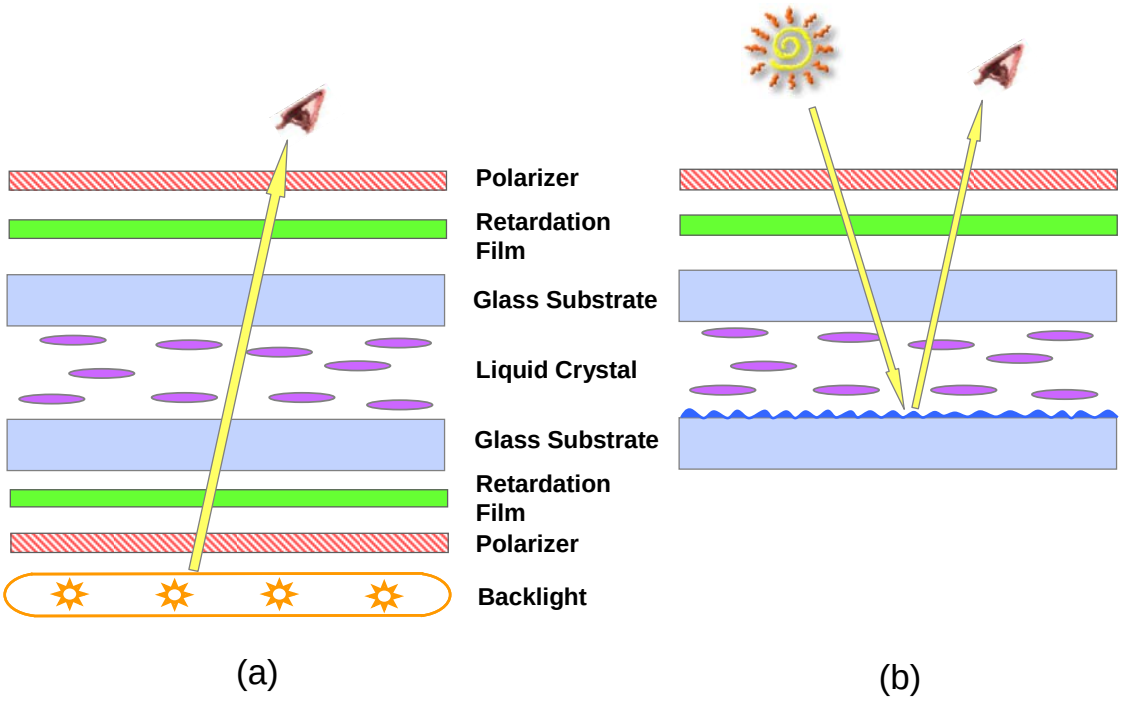

Figure 2.12: Schematic diagram of (a) a transmissive LCD and (b) a reflective LCD.

The optical modeling configurations for the transmissive and the reflective displays are shown in Figs. 2.13(a) and 2.13(b). The matrix based solver is based on the layered structure of the whole display system. To introduce the detailed optical theory to characterize these two type displays, we have explored a reflective display with asymmetric incident and exit angles as a benchmark. The detailed modeling can be found in Ref. 24. Here the optical methods related can be easily converted to transmissive LCDs.

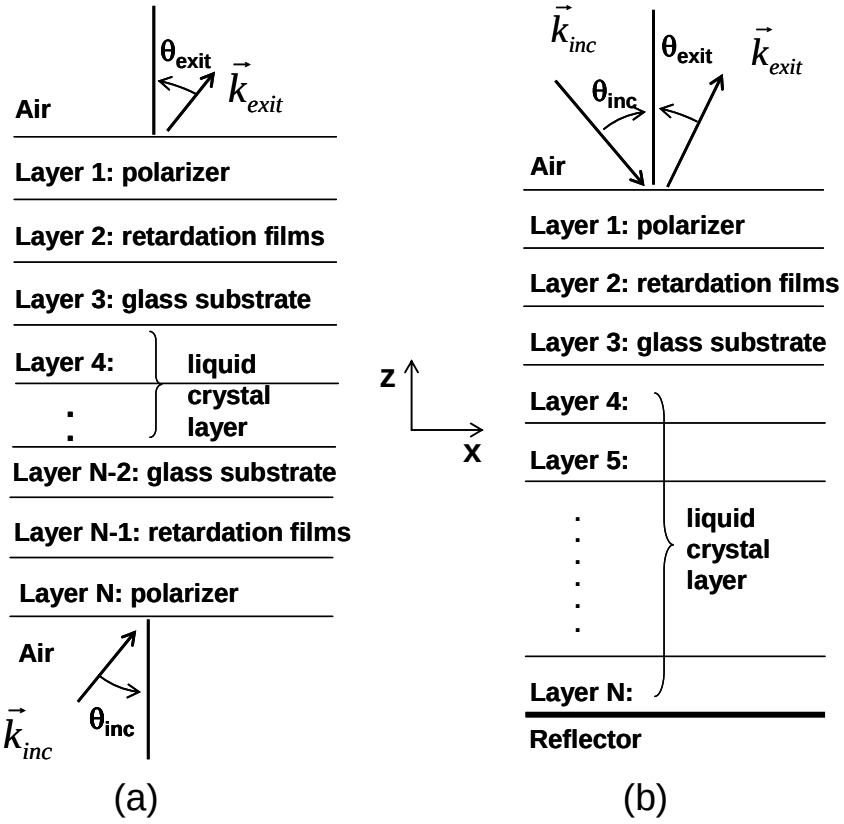

Figure 2.13: Optical schematic of (a) a transmissive LCD and (b) a reflective LCD.

2. 2. 2. Optical Methods for Diffractive Liquid Crystal Devices

Besides its application in displays, liquid crystal materials are also widely used for phase modulation, such as laser in beam steering devices. For the display calculations, a major assumption is that the variation of liquid crystal orientation is only along the vertical direction that is normal to the glass substrates, and there is sufficiently slow change along the transverse directions. However, this is no longer valid for beam steering devices where abrupt molecular variations usually occur in the transverse directions. Thus these matrix based 1D solvers are insufficient to model such devices.

A rigorous method for this kind of problem is the finite-difference-time-domain (FDTD) method[31, 32], which has been a general tool in electromagnetic simulations. However, the drawback of applying FDTD in simulation is its low computing efficiency. For a real device simulation, the FDTD method usually requires a fine mesh size (usually less than $\lambda/10$) for convergence, which requires a fine discretization of time step and results in quite a long computing time. Another alternative and highly successful method for guided wave optics is the beam propagation method (BPM), which is quite efficient tool. The detailed derivation of the BPM for liquid crystal optics is provided in Refs. 29-30, and introduction of BPM in modeling beam steering devices will be discussed in Chapter 4 in detail.

2. 3. Summary

We have derived a comprehensive dynamic LC director deformation calculation model based on FEM. The vector represented LC director is calculated by iteration between the

calculations of potential and director distributions. Weak form technology is introduced to simplify the derivation of director calculation formulations. Excellent agreement is obtained between this method and the commercial 2dimMOS software in calculating a 2D IPS structure. And the comparison of FEM and FDM in simulating a 3D super IPS structure also shows good agreement as well. This works provides an accurate tool for further designing and optimizing novel high performance devices based on LC material. In addition to the LC deformation modeling, the optical methods for display and laser beam steering devices are also investigated. These numerical methods provides us efficient theoretical basis and tools to study new LC devices oriented at different applications.

2. 4. References

1. J. Jin, “The Finite Element Method in Electromagnetics,” 2nd Edition, Wiley-IEEE Press, (2002).
2. M. Ohe and K. Kondo, “Electro-optical characteristics and switching behavior of the in-plane switching mode,” Appl. Phys. Lett., vol. 67, pp. 3895-3897, (1995).
3. Autronic-MELCHERS GmbH, available: http://www.autronic-melchers.com/index.htm
4. S. Endoh, M. Ohta, N. Konishi, and K. Kondo, ”Advanced 18.1-inch diagonal super-TFT-LCDs with mega wide viewing angle and fast response speed of 20 ms,” IDW’99, pp. 187-190, (1999).
5. D. W. Berreman, “Numerical modeling of twist nematic devices,” Phil. Trans. R. Soc. Lond., A 309, pp. 203-216, (1983).

6. J. E. Anderson, P. Watson, P. J. Bos, “LC3D: Liquid Crystal Display 3-D Directory Simulator, Software and Technology Guide,” Artech House Publishers, (1999).
7. G. Haas, S. Siebert, and D. A. Mlynski, “Simulation of inhomogeneous electric field effects in liquid crystal displays,” Proceedings of the Ninth International Display Conference, Society for Information Display and Institute of Television Engineers of Japan, vol.89, pp.524, (1989).
8. H. Mori, E. C. Gartland, Jr., J. R. Kelly, and P. J. Bos, “Multidimensional director modeling using the Q tensor representation in a liquid crystal cell and its application to the π cell with patterned electrodes,” Jpn. J. Appl. Phys., vol. 38, pp.135-146, (1999).
9. S. Dickmann, J. Eschler, O. Cossalter, and D. A. Mlynski, "Simulation of LCDs Including Elastic Anisotropy and Inhomogeneous Field," SID Dig. Tech Pap., vol. 24, pp. 638-641, (1993).
10. D. W. Berreman and S. Meiboom, “Tensor representation of Oseen-Frank strain energy in uniaxial cholesterics,” Phys. Rev. A, vol. 30, pp. 1955-1959, (1984).
11. P. G. De Gennes and J. Prost, “The physics of liquid crystals,” 2nd Edition, Oxford Science Publications, (1993).
12. W. Oseen, “The theory of liquid crystals,” Trans. Faraday Soc., vol. 29, pp. 883, (1933).
13. F. C. Frank, “On the theory of liquid crystals,” Discuss. Faraday Soc., vol. 25, pp. 19, (1958).
14. J. E. Anderson, C. Titus, P. Watson, and P. J. Bos, “Significant speed and stability increases in multi-dimensional director simulations,” SID Tech. Digest, vol. 31, pp. 906-909, (2000).
15. F. A. Fernandez, S. E. Day, P. Trwoga, H. F. Deng, and R. James, “Three-dimensional modeling of liquid crystal display cells using finite elements,” Mol. Cryst. Liq. Cryst., vol.

375, pp. 291-299, (2002).

16. A. Rapini and M. J. Papoular, “Distortion d’une lamelle nématique sous champ magnétique conditions d’ancrage aus parois,” J. Phys. Colloq. vol. 30, pp. C4, (1969).
17. D. Demus, J. Goddby, G. W. Gray, H-W. Spiess, “Handbook of liquid crystal,” vol. 1: Fundamentals edited by V. Vill, Wiley-VCH, (1998).
18. A. Takeda, S. Kataoka, T. Sasaki, H. Chida, H. Tsuda, K. Ohmuro, T. Sasabayashi, Y. Koike, and K. Okamoto, “A super-high image quality multi-domain vertical alignment LCD by new rubbing-less technology,” SID Tech. Digest, vol. 29, pp.1077-1080, (1998).
19. K. H. Kim, K. H. Lee, S. B. Park, J. K. Song, S. N. Kim, and J. H. Souk, “Domain divided vertical alignment mode with optimized fringe field effect”, in Proc. 18th Int’l Display Research Conference (Asia Display’98), pp. 383-386, (1998).
20. R. C. Jones, “A new calculus for the treatment of optical systems. I. Description and discussion of the calculus,” J. Opt. Soc. Am. 31, 488-500 (1941).
21. P. Yeh, “Extended Jones matrix method,” J. Opt. Soc. Am. 72, 507-513 (1982).
22. A. Lien, “Extended Jones matrix representation for the twisted nematic liquid-crystal display at oblique incidence,” Appl. Phys. Lett. 57, 2767-2769 (1990).
23. A. Lien, “A detailed derivation of extended Jones matrix representation for twisted nematic liquid crystal displays,” Liq. Cryst., 22, 171-175 (1997).
24. Z. Ge, X. Zhu, T. W. Wu, and S. T. Wu, “Reflective liquid crystal displays with asymmetric incidence and exit angles,” J. Opt. Soc. Am. A 22, 966 (2005).
25. D. W. Berreman, “Optics in stratified and anisotropic media: 4×4 matrix formulation,” J. Opt. Soc. Am. 62, 502-510 (1972).

26. H. Wohler, G. Hass, M. Fritsch, and D. A. Mlynski, “Faster 4×4 matrix method for uniaxial inhomogeneous media,” J. Opt. Soc. Am. A 5, 1554-1557 (1988).
27. K. Eidner, G. Mayer, M. Schmidt and H. Schmiedel, “Optics in stratified media - the use of optical eigenmodes of uniaxial crystal in the 4×4 matrix formalism,” Mol. Cryst. Liq. Cryst. 172,191-200 (1989).
28. S. Teitler and B. W. Henvis, “Refraction in stratified, anisotropic media,” J. Opt. Soc. Am. 60, 830-834 (1970).
29. E. E. Kriezis and S. J. Elston, “A wide angle beam propagation method for the analysis of tilted nematic liquid crystal structures,” J. Mod. Opt. 46, 1201–1212 (1999).
30. E. E. Kriezis and S. J. Elston, "Wide-angle beam propagation method for liquid-crystal device calculations," Appl. Opt. 39, 5707-5714 (2000).
31. E. E. Kriezis and S. J. Elston, "Light wave propagation in liquid crystal displays by the 2-D FDTD method," Opt. Commun. 177, 69-77 (2000).
32. X. Wang, B. Wang, P. J. Bos, J. E. Anderson, J. J. Pouch, and F. A. Miranda, "Finite-difference time-domain simulation of a liquid-crystal optical phased array," J. Opt. Soc. Am. A 22, 346-354 (2005).

CHAPTER 3: TRANSFLECTIVE LIQUID CRYSTAL DISPLAYS

The increasing demand for low power consumption and good outdoor readability mobile displays such as cell phones and personal digital assistants (PDA) drives a heated research and development of transflective liquid crystal displays[1]. In general, transflective LCDs can be divided into two categories based on the LC cell configurations: dual cell gap[2, 3] and single cell gap structures[4-8]. The dual cell gap transflective LCDs employ different cell gaps in the transmissive (T) region and the reflective (R) region to compensate their optical path difference. As a result, high transmittance and high reflectance are obtained and their voltage-dependent transmittance (V-T) and reflectance (V-R) curves overlap quite well. However, the fabrication process is rather complicated and the response time for the T and R modes is different. On the other hand, the single cell gap transflective LCDs use the same cell gap for both T and R regions. Its associated fabrication is easier and response time for the T and R modes is the same. Thus, this approach has attracted much research attention. The main technical challenges in single cell gap transflective LCDs are twofold: 1) it is difficult to obtain high T and R simultaneously, and 2) the grayscale matching between the T and R modes is usually poor.

Besides high light efficiency under a single cell gaped structure and a single gamma curve driving, wide viewing angle of transflective LCDs are also quite crucial. And two research directions can be usually explored for wide viewing angle: 1) introducing multi-domain vertically aligned (VA) LC structure, but requiring a fine design of compensation films, such as wide-viewing angle circular polarizers; and 2) using fringe-field switching mode for transmissive part without additional compensation films, but requiring a functional optical design for the

reflective part to obtain a good dark state. In the following section, we will first propose one transflective LCD configuration that employs a VA LC cell with special electrode design to achieve high light efficiency and good matching VT and VR curves, followed by a FFS based transflective LCD with inherent wide-viewing angle T mode, and good dark state by employing an internal wire grid polarizer as the reflector. In addition to the cell designs, we further investigate the development of wide-viewing angle circular polarizers, that greatly improve the performance of transflective LCDs using MVA technology.

3. 1. Transflective LCDs Using A Vertically Aligned Liquid Crystal Mode

We developed a normally black, single cell gap transflective LCD using a vertical alignment (VA) LC cell with special rubbing directions. This device uses commonly biased reflectors to generate different electric field distributions in the T and R regions. As a result, the device shows a high light efficiency and excellent match between V-T and V-R curves. In addition, the rubbing direction of the LC cell and the biased voltage on the reflectors are essential for achieving high light efficiency and good grayscale matching between T and R modes.

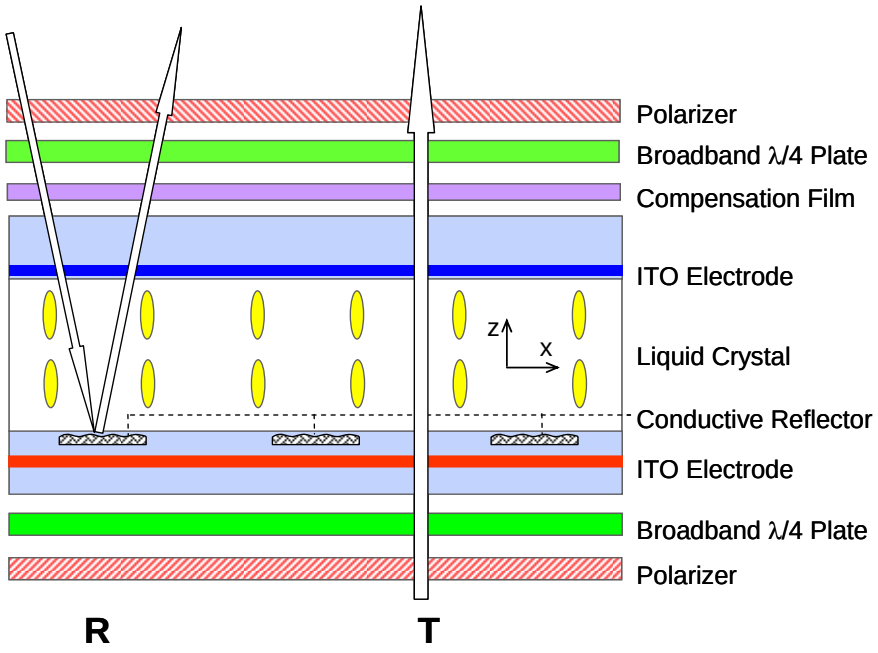

Figure 3.1: Schematic of the transflective LCD using commonly biased reflectors.

Figure 3.1 shows the schematic structure of the proposed transflective LCD device with commonly biased reflectors. On each side of the LC cell, a broadband quarter-wave plate[9] along with a linear polarizer work together as a circular polarizer. Within each pixel, the LC cell is repetitively divided into T and R regions. In the T region, the LC layer is sandwiched between the top transparent indium-tin-oxide (ITO) common electrode and the bottom ITO pixel electrode. In the R region, periodically patterned conductive layers are formed above the bottom pixel electrode as the reflectors, which are commonly biased to a certain voltage (below the threshold voltage) for all pixels. When no voltage is applied, all the LC directors are vertically aligned. Therefore, the light passing through the LC layer experiences no phase retardation and keeps its polarization state, resulting in a dark state for both T and R modes. On the other hand, as the

voltage exceeds a threshold (V_{th}), the LC directors are tilted and the phase retardation effect takes place. Ideally, the required phase retardation change is ~λ/2 for the T region and ~λ/4 for the R region in order to achieve maximum transmittance and reflectance.

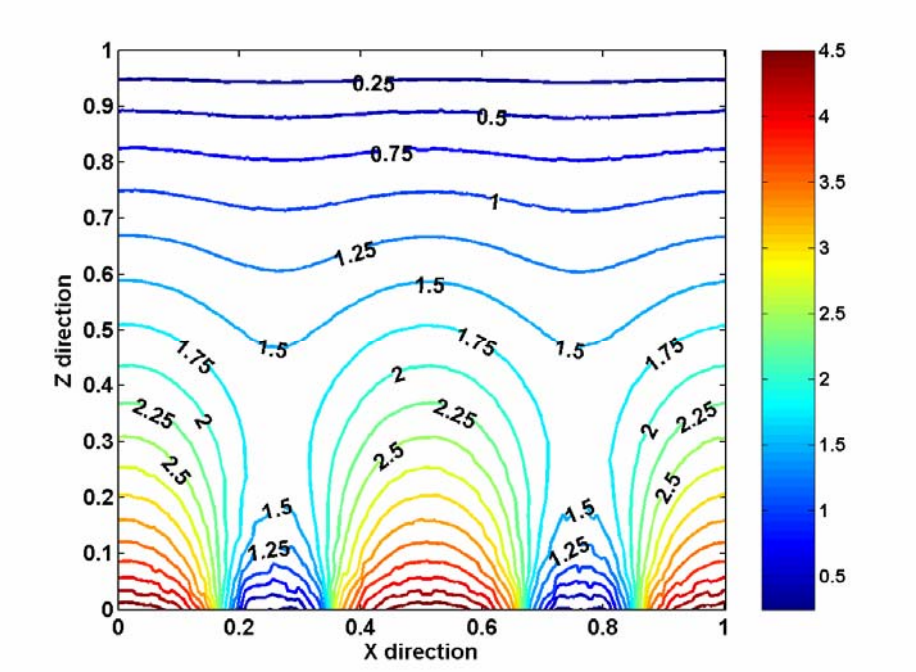

Figure 3.2: The potential distribution in the LC cell of the transflective LCD.

Figure 3.2 shows the calculated equal-potential line distribution in the LC layer within one repetitive period when V=6.5 V_{rms} is applied to the bottom pixel electrode while all the reflectors are biased at 0 V_{rms}. The potential difference between neighboring vertical lines is 0.25 V_{rms}. Here the LC material employed is a negative dielectric anisotropy (Δε) Merck mixture MLC-6608, with its extraordinary and ordinary refractive indices n_e=1.5578, n_o=1.4748 (at λ=589 nm), parallel and perpendicular dielectric constants $\varepsilon_{//}$ = 3.6, $\varepsilon_{\perp}$ = 7.8, and its elastic constants K_{11} = 16.7 pN and K_{33} = 18.1 pN. The cell gap of the LC layer is 5 μm, the reflector

width is 2 μm, and the horizontal gap between adjacent reflectors is 5 μm. In order to show the relative positions, both vertical and horizontal dimensions in Fig. 3.2 are normalized to their real lengths. In the T regions ($x \in [0, 0.18]$, [0.32, 0.68], and [0.82, 1]) in Fig. 3.2, the potential values decrease quite uniformly in the vertical directions, indicating a uniform distribution of vertical electric fields in those regions. However in the R regions ($x \in [0.18, 0.32]$ and [0.68, 0.82]), the regions with uniform potential changes in the vertical direction are located near the surfaces, e.g., from z = 0 to ~0.3 and from z = ~0.7 to 1.0. Correspondingly, strong vertical fields are only confined to the cell surface areas, and an area with ultra-low vertical field components in the bulk LC layer is generated. This type of field distribution originates mainly from the voltage shielding by the commonly biased reflectors. Here we call this phenomenon as surface field effect. Under this field distribution, the LC directors in the T region can tilt more than those in the R region. That means the effective phase retardation in the T region is more than that in the R region. This is what a transflective LCD needs.

Due to the existence of strong horizontal electric fields as shown in Fig. 3.2, the initial surface rubbing directions of the LC directors play a critical role in affecting the transmittance. Figure 3.3 shows the calculated time-dependent transmittance using extended Jones matrix method[10,11] for the cases with surface rubbing angle $\phi = 0°$ (parallel), $\phi = 50°$, and $\phi = 90°$ (perpendicular) with respect to the strip electrodes in the x-direction. In these cases, the pretilt angle is 88°, the pixel electrode voltage is 6.5 V_{rms}, and the reflectors are all biased at 0 V_{rms}. From Fig. 3.3, when $\phi = 50°$ and 90°, the transmittance increases monotonously from 0 to over 90% (normalized to the maximum light transmittance through two polarizers) and saturates when t >80 ms. This indicates the LC directors experience a smooth reorientation and finally reach at a

stable state. On the other hand, when ϕ= 0° (along the +x direction in Fig. 3.1) the maximum transmittance is lower those of ϕ= 50° and 90° below 100 ms, then two transition kinks occur at t ~90 ms and t ~120 ms and the transmittance further increases to a final saturation level. From Fig. 3.3, the LC reorientation mechanisms for these two cases are different.

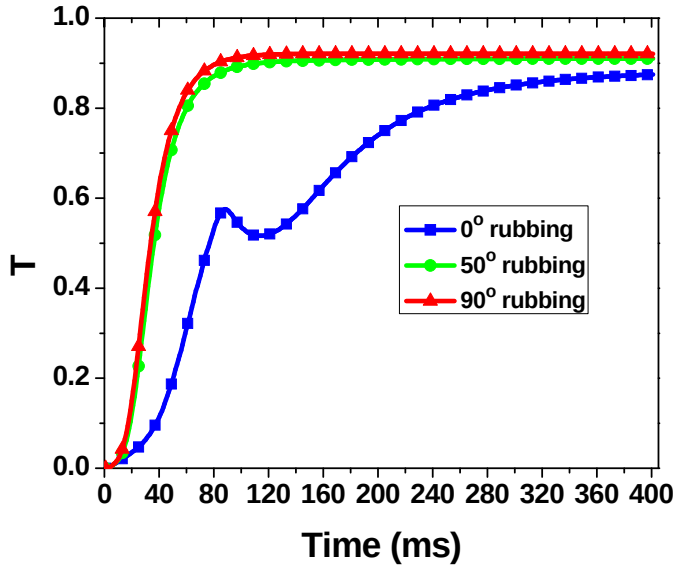

Figure 3.3: Dynamic transmittance response of the LC cell at different rubbing angles.

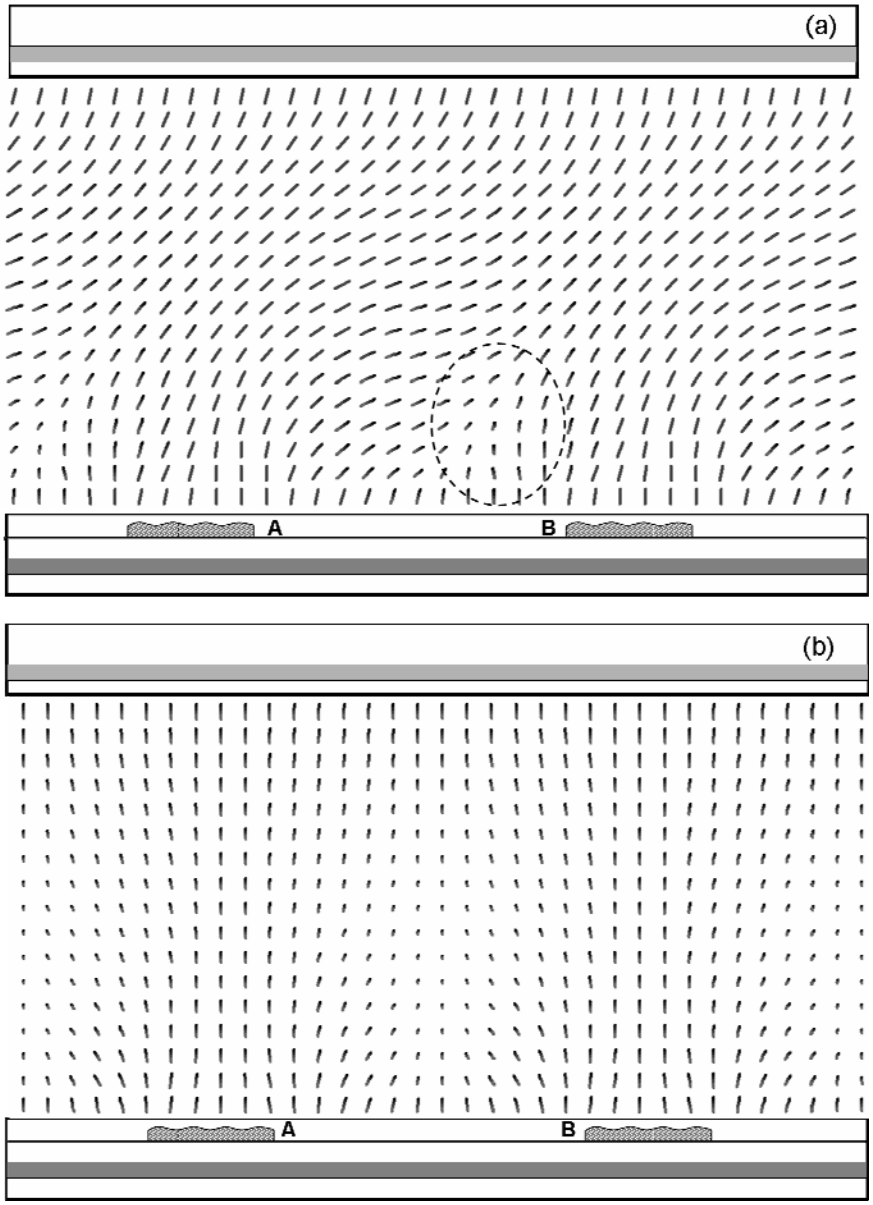

Figure 3.4: LC director profile of the cell with rubbing angle (a) at 0^o and (b) at 90^o.

To understand the rubbing angle effect, we need to know the LC directors distribution for both cases. Figure 3.4(a) shows the calculated LC director distribution using 2dimMOS software (from autronic- MELCHERS, Germany) at t~110 ms for the case of ϕ= 0°. When a high voltage

is applied, the vertical electric fields between the pixel and common electrodes and the horizontal fields at the right edge of the reflectors (position A in Fig. 3.4(a)) tend to tilt down the LC directors toward the +x direction due to the 2° pretilt angle. But the horizontal electric fields at the left edge of the reflectors (position B in Fig. 3.4(a)) tend to reorient the LC directors toward the –x direction. These two opposite torques push the $-\Delta\varepsilon$ LC molecules in their adjoining region (the circled region in Fig. 3.4(a)) to twist into the +y direction. Thus a twisted region is formed and the light efficiency is lowered as observed in Fig. 3.3 at t ~100 ms. The lower transmittance results from the twisted LC structure that exhibits a lower transmittance when sandwiched between two circular polarizers[3]. After 100 ms, all the LC directors start to twist into the +y direction and the transmittance increases again. However, this transition process takes a long time as shown in Fig. 3.3.

If the initial rubbing direction is far way from the x-direction, such as 90°, a smoother LC reorientation occurs. Figure 3.4(b) shows the director distribution at t =110 ms with ϕ= 90°. Once a high voltage is applied, the vertical electric fields will substantially tilt the directors down into the +*y* direction. Similarly, the horizontal field components at edges of the reflectors (positions A and B in Fig. 3.4(b)) tend to tilt the nearby LC directors toward the opposite directions. But because most of LC directors there have been tilted down into the +y direction, their competence can be balanced. Consequently, the change of transmittance with respect to time is smooth and it reaches saturation much faster than that with an initial rubbing direction set at 0°. Similarly, for the cell with rubbing angle ϕ= 50°, the pre-orientation by the surface rubbing also helps the LC directors tilt down smoothly and quickly into the rubbing direction by the vertical fields, as indicated in Fig. 3.3.

In the R regions the electric fields are mainly confined to the surface regions, the LC directors near the top and bottom surfaces are first tilted down to the +y direction when ϕ= 90°. Because the LC is a continuum, their reorientation will further perturb the molecules in the low field region. Because of the existence of this low field region, the overall tilt of LC directors there will be much lower than those in the T region. By optimizing the dimensions of reflector width, gap, rubbing angle, and the commonly biased voltages on the reflectors, it is possible to obtain a high optical efficiency for the T and R modes and a small disparity between the VT and VR curves.

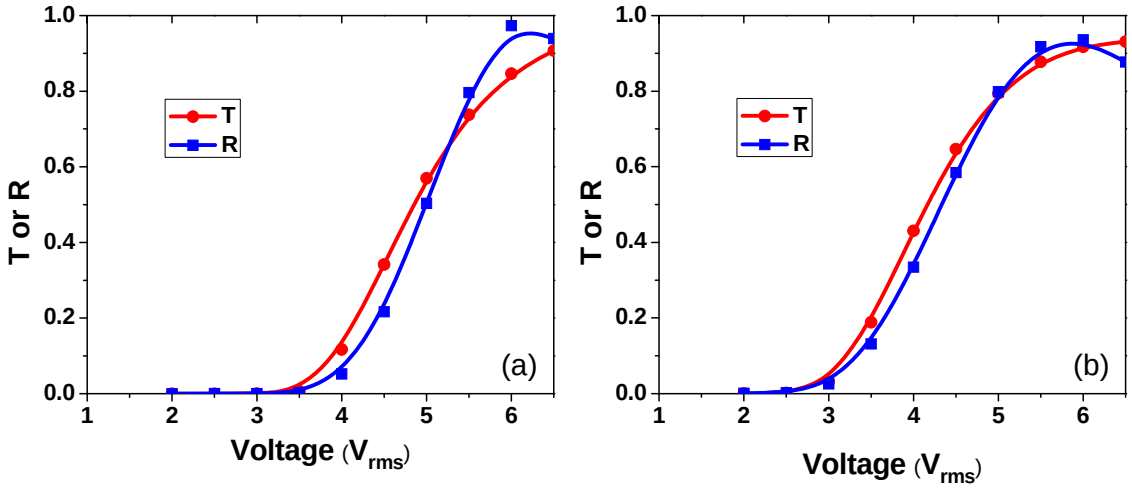

Figure 3.5: Voltage dependent light efficiency curves for the cell where the reflectors are biased to (a) 0 V_{rms} and (b) 1.5 V_{rms} with respect to the common electrode.

Figure 3.5(a) shows the calculated VT and VR curves for a single cell gap transflective LCD with 5 μm cell gap, 2 μm reflector width, and 5 μm reflector gap. The commonly biased voltage for the reflectors is V=0 V_{rms} for all pixels. The surface rubbing angle is at 90° and the

pretilt angle is 88°. Both VT and VR curves reach ~90% (T: ~91%, R: ~ 93%) light efficiency at V= 6.5 V_{rms}. Besides, the VT and VR curves also show a reasonably good overlap with each other. To estimate their match, we define the root-mean-square (RMS) difference as $\sqrt{\sum_{i=1}^{N}(T_i - R_i)^2 / N}$ to quantitatively characterize the T and R difference, where the Ti and Ri are the normalized transmittance and reflectance at the *i*-th gray level, and N is the total number of gray levels sampled. For example, if N=256 is sampled between 2.5 V_{rms} and 6.5 V_{rms} from the curves in Fig. 3.5(a), the RMS difference is ~7.5%. To further reduce the difference between VT and VR curves, a small voltage 1.5 V_{rms} (it is below threshold and will not affect the dark state) is applied to the commonly biased reflectors; the reflector width and gap are set at 3 μm and 6 μm, respectively, and the rubbing angle is set at 50° with respect to the x-axis. Figure 3.5(b) shows the corresponding VT and VR curves. Indeed, a better grayscale overlap with only ~4.7% RMS difference is obtained.

In a real LCD driving, the polarity of the voltage between the pixel and common electrodes is kept changing to avoid ion trapping on the cell surface. Therefore to keep the desired voltage difference (as the values discussed above) among the reflectors and the electrodes, the polarity of the commonly biased voltage (if it is not zero) on the reflectors also needs to be changed synchronously. In this case, frame inversion scheme can be employed to control the voltage polarity between the pixel and common electrodes, and the same control signal to inverse frames can be taken to shift the polarity of the commonly biased voltage on the reflectors throughout the whole panel. On the other hand, if the biased voltage on the reflectors is zero, other inversion schemes such as column inversion, row inversion, and dot inversion can

also be applied to the driving of this device.

In summary, we have demonstrated a single cell gap transflective LCD using a VA cell with commonly biased reflectors. In this transflective LCD, the maximum transmittance and reflectance both reach ~90% and their grayscales match quite well for a single driving circuit. Potential application of this transflective LCD for mobile displays, in which low power consumption and good outdoor readability are required, is foreseeable.

3. 2. Transflective LCDs Using Fringe Field Switching Mode and Internal Wire Grid Polarizer

Fringe-field switching (FFS) mode[12] LCD inherently has a wide viewing angle (small gamma curve dispersion and gray-scale inversion free), and its light efficiency has been continuously improved to be close to that of a TN cell. Thus it is quite suitable for small to medium LCD panels that require high brightness and wide viewing angle. However, because the LC molecules are initially homogeneously aligned in a FFS cell, it is quite difficult to achieve a dark state for a reflective FFS cell. To solve this problem, researchers developed in-cell retarder in the reflective part to obtain a common dark state between the transmissive and reflective modes when no voltage is applied[13-16]. However, a drawback of this approach is the complexity in real fabrication process and thus is hard to achieve a good yield. An alternative of this in-cell retarder method is to use internal wire grid polarizer as a polarization dependent reflector in the reflective part[17, 18].

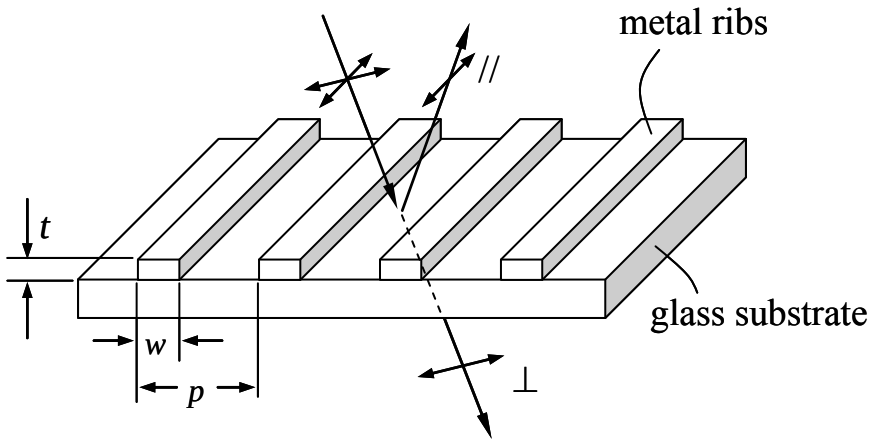

Figure 3.6: Schematic illustration of wire grid polarizer.

Figure 3.6 shows the typical structure of a wire grid polarizer where metal (e.g., aluminum) ribs are periodically formed on the glass substrate. For an unpolarized incident light, the light component whose electric field vector is parallel to the wire grids will be almost fully reflected by the WGP. Conversely, most of the light with electric field vector perpendicular to the wire grids will transmit through the WGP. Detailed explanation for this polarization-dependent reflection of the WGP in visible spectrum can be found in Refs. 19 and 20. Exploiting this unique polarization-dependent reflection, Hansen et al applied the WGP into the entire cell region and use an external controller to switch between the transmissive and reflective modes[21]. But an inversion between transmissive and reflective images is observed. To overcome this image inversion and obtain a wide-viewing angle display, we proposed a method using WGP in a FFS cell for a transflective LCD design as shown in Fig. 3.7. In this design, the LC cell is sandwiched between two crossed linear polarizers, and the WGP is formed on the lower substrate with its wire grids aligned with the transmission axis of the bottom polarizer.

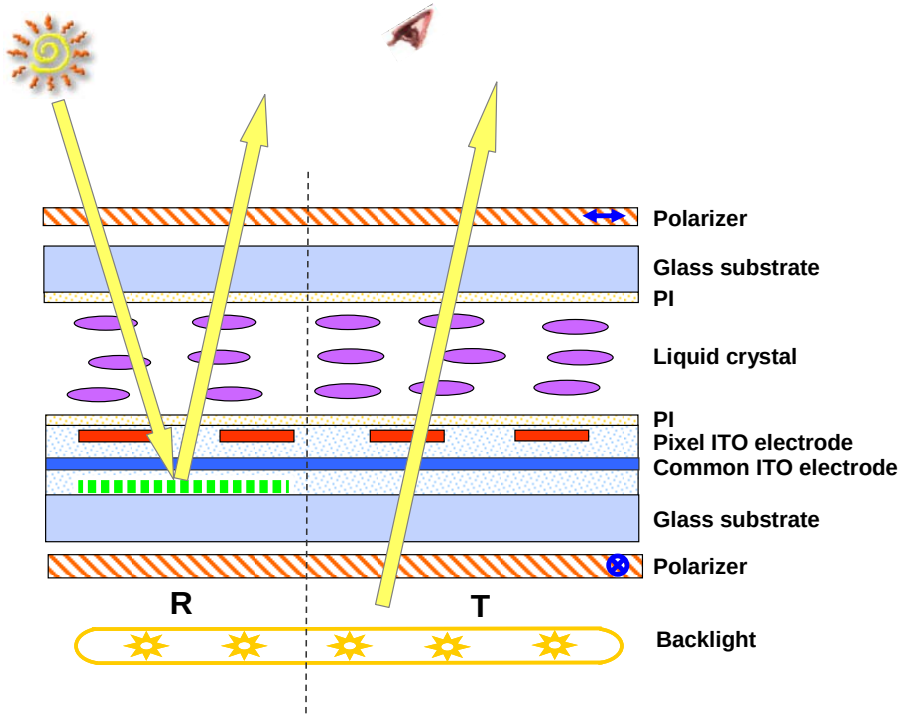

Figure 3.7: Schematic of transflective LCD using FFS mode and an internal WGP.

In the normally black FFS cell shown in Fig. 3.8, the boundary LC directors are initially rubbed at 0° (or 90°) with respect to the transmission axis of the top polarizer. At the voltage-off state, the linearly polarized ambient light from the top polarizer keeps its polarization after the homogeneous LC cell aligned parallel to (or perpendicular to) its polarization direction. With its polarization perpendicular to the wire grid, the light can pass through the WGP and is further absorbed by the bottom polarizer. For the transmissive part, the backlight passing the bottom polarizer maintains its polarization state through the LC layer, and is blocked by the crossed top polarizer. Consequently, a common dark state is achieved for both the transmissive and reflective modes.

On the other hand, after the applied voltage exceeds the threshold voltage, the LC directors are reoriented by the applied electric fields. Under proper reorientation (about 45° away from its initial orientation), the cell can be tuned to reach a state that is functionally equivalent to a λ/2 plate. In the reflective mode, the polarization axis of the incoming ambient light from the top polarizer is rotated 90° by the LC cell and becomes parallel to the wire grids, thus is reflected back into the LC cell by the WGP. It further transverses the λ/2 LC cell and gets another 90° rotation, thus exits the top polarizer. Similarly in the transmissive mode, the backlight from the bottom polarizer is also rotated by the LC cell to transmit the top polarizer. As a result, a common bright state is achieved.

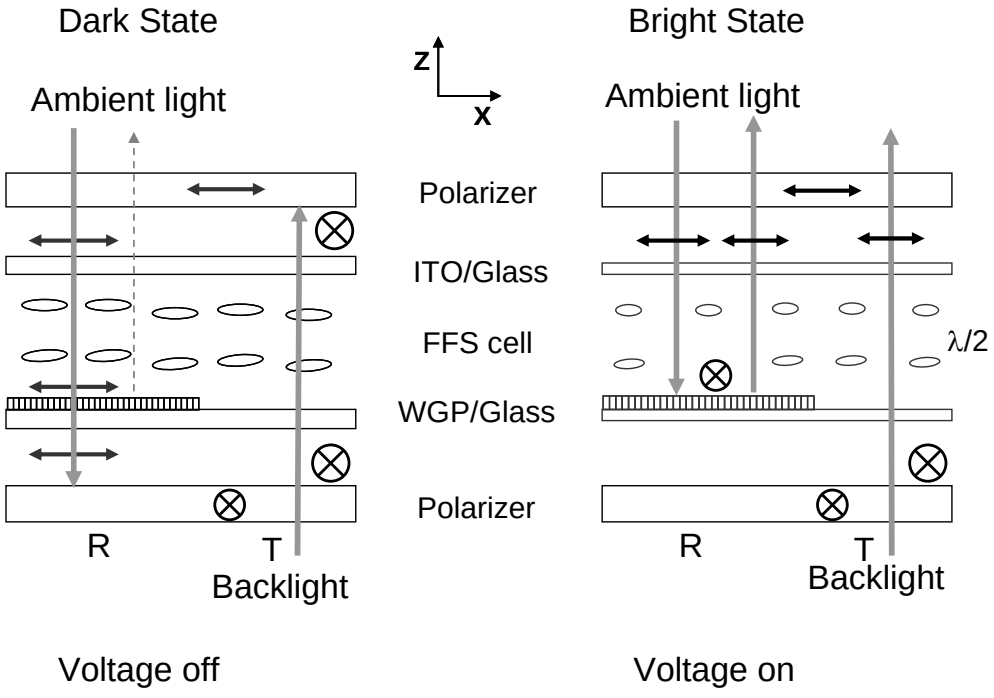

Figure 3.8: Illustration of the dark state and bright state.

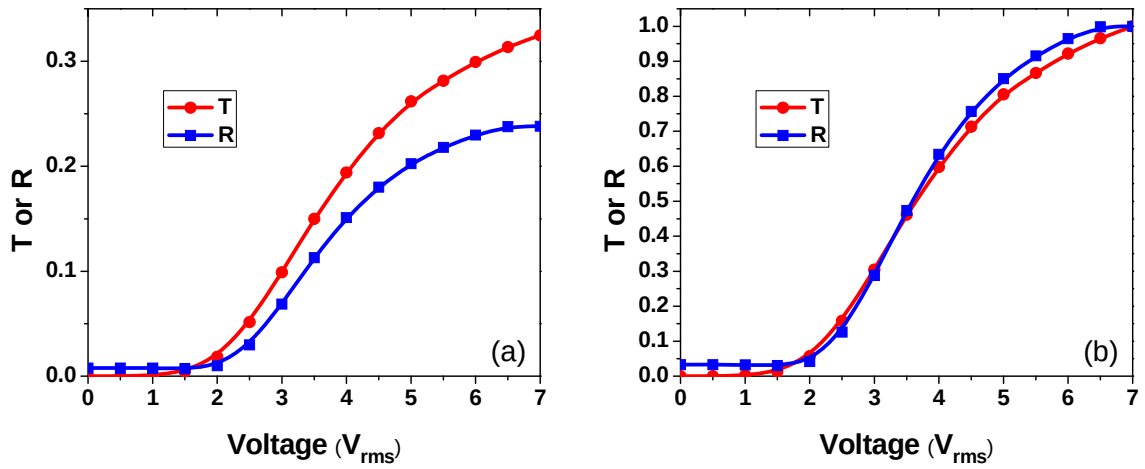

Figure 3.9: VT and VR curves (a) before normalization and (b) after normalization using a positive Δε LC material.

To validate this device concept and investigate its performance, the electro-optic performance such as voltage-dependent transmittance (VT) curve and voltage-dependent reflectance (VR) curve using a positive dielectric anisotropy (Δε) LC material are calculated in Figs. 3.9(a) and 3.9(b). For the FFS cell, a positive Δε Merck LC mixture MLC-6686 is used. Its physical properties are listed as follows: extraordinary and ordinary refractive indices n_e=1.5574, n_o=1.4824 (at λ=589 nm), parallel and perpendicular dielectric anisotropy $\varepsilon_{//}$ =14.5, $\varepsilon_{\perp}$=4.5, elastic constants K_{11}=8.8 pN, and K_{33} =14.6 pN. The surface pretilt angles in the FFS cell are set at 2°. In calculations, the extended Jones matrix method as discussed above is used for the transmissive mode and 4×4 matrix method is taken for the reflective mode. Here in the WGP surface plane, the direction perpendicular to the wires is defined as the x-axis, and that parallel to

the wires is set as the y-axis. Besides, the WGP is modeled as a uniaxial layer by the effective media theory[20] with its ordinary and extraordinary refractive indices as:

$$n_o^2 = n_1^2 \frac{w}{p} + n_2^2 (1 - \frac{w}{p}), \quad (1)$$

$$\frac{1}{n_e^2} = \frac{1}{n_1^2} \frac{w}{p} + \frac{1}{n_2^2} (1 - \frac{w}{p}). \quad (2)$$

For the current example, w/p is set as 0.2, the metal for wire grids is made of aluminum with refractive index n_1 = 0.95+6.69×i at 550 nm, and the gap is filled with dielectric material SiO_2 with refractive index n_2 = 1.48. For the FFS cell, the cell gap is set at 5μm, and both the electrode width W and electrode gap G in the transmissive region are set at 3 μm, and W = 3μm and G= 5μm are set for the reflective region. Here the smaller gap value in the transmissive region is designed to make the threshold voltage there a little bit larger for a good match of gray scales with the reflective mode. As shown in Figs. 3.9(a) and 3.9(b), the maximum transmittance is around 32% and the maximum reflectance is about 23.8%, while the maximum value possible from two parallel linear polarizers are about 36%. This reduced light efficiency results from the tilt of LC molecules induced by the fringe fields and the imperfect reflection from the wire grid polarizer.

The light efficiency can be further improved by employing a negative Δε LC material to suppress the tilt of LC molecules. The LC material used here is a negative Δε Merck LC mixture MLC-6608, with its physical properties listed as follows: extraordinary and ordinary refractive indices n_e=1.5578, n_o=1.4748 (at λ=589 nm), parallel and perpendicular dielectric anisotropy $\varepsilon_{//}$ =3.6, $\varepsilon_{\perp}$=7.8, elastic constants K_{11}=16.7 pN, and K_{33} =18.1 pN. The calculated VT and VR curves

are shown in Figs. 3.10(a) and 3.10(b). Because the rotation of LC molecules are more uniform (less tilt of LC molecules) than that in the cell using a positive $\Delta\varepsilon$ LC material, both the transmittance and reflectance are improved to T~ 35% and R~26.3%.

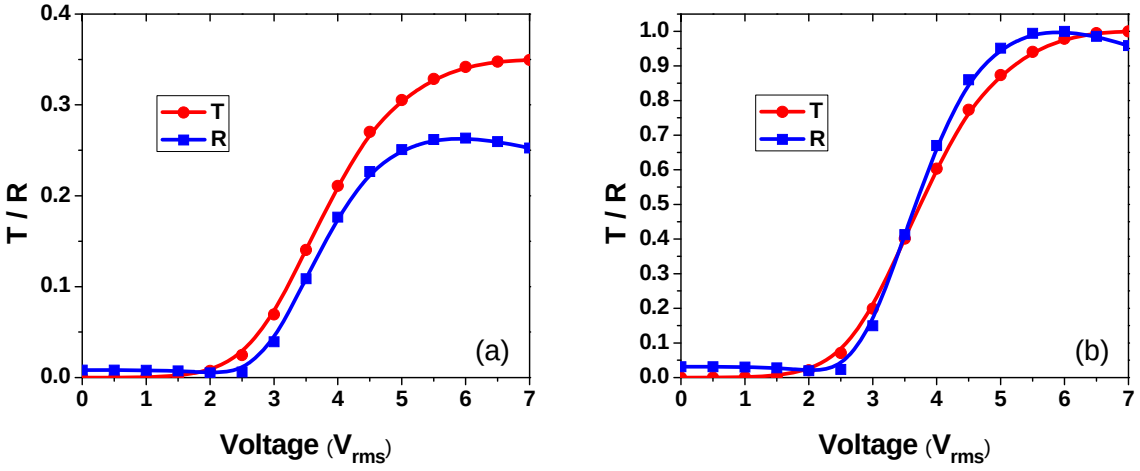

Figure 3.10: VT and VR curves (a) before normalization and (b) after normalization using a negative $\Delta\varepsilon$ LC material.

The viewing angle of above FFS cells in the transmissive mode are plotted in Figs. 3.11(a) and 3.11(b), where a contrast ratio of 10:1 can be obtained at over 60^{o} without using additional compensation films.

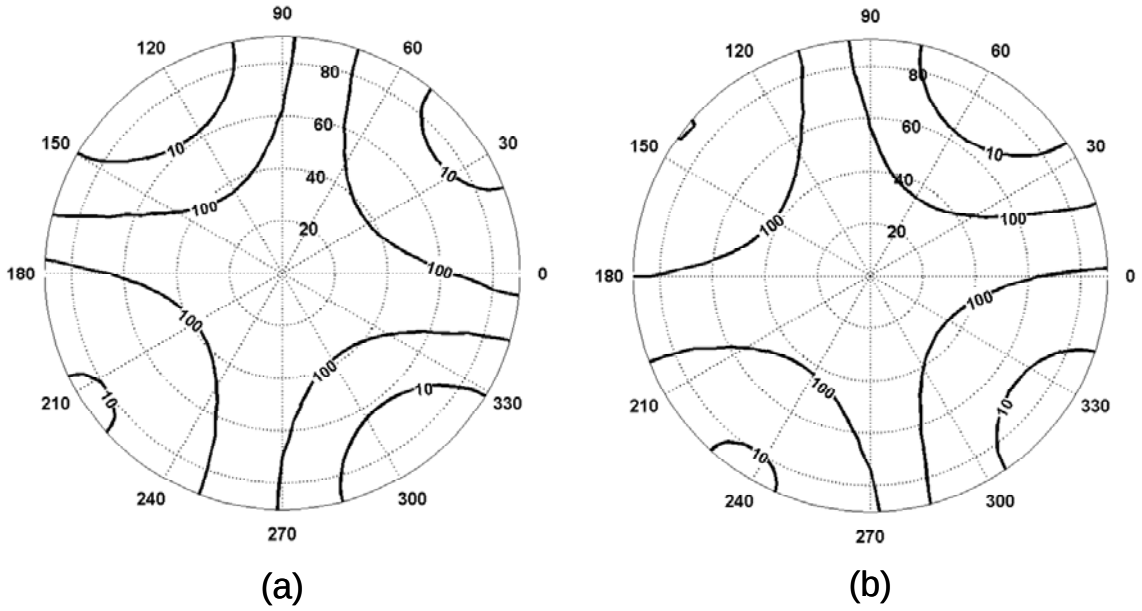

Figure 3.11: Iso-contrast plots for a FFS cell using (a) a positive Δε and (b) a negative Δε LC material.

3. 3. Broadband and Wide-view Circular Polarizers Using Self-compensated Positive and Negative Uniaxial A-plates

3. 3. 1. Motivations

Another approach to obtain wide-viewing angle (gray-scale inversion free) transflective LCDs is to use multi-domain vertically aligned (MVA) mode. However, in this method, it requires wide-viewing angle circular polarizers. In conventional MVA based transflective LCDs, the viewing angle of most transflective LCDs is fairly narrow because of the use of two crossed broadband circular polarizers (CPs). Although the recent progress in developing in-plane switching based transflective LCD enhances the viewing angle of the transmissive mode, the

challenge is its need for an in-cell phase retarder to assure a good dark state for the reflective mode [13-16]. On the other hand, it is very easy to obtain a common dark state for the transmissive (T) and reflective (R) modes in a VA LCD[22], but more researches are needed to improve its performance under circular polarizers.

A conventional cost-effective broadband circular polarizer consists of a linear polarizer, a uniaxial monochromatic half-wave plate, and a uniaxial monochromatic quarter-wave plate, with their optic axes aligned at certain angles[9]. To reduce cost, the employed retardation films are usually made of uniaxial positive A-plates. The produced polarization is circular only at normal incidence, while its off-axis light leakage is still quite evident. Replacing the uniaxial quarter-wave plate with a biaxial quarter-wave plate only slightly improves the acceptance angle[23, 24]. Optimizing both half-wave film and quarter- wave film by the combinations of uniaxial A-plates and C-plates[25] or two biaxial films[26] significantly widen the acceptance angle, but their device configurations are quite sophisticated. Recently, circular polarizers with two linear polarizers and a positive and a negative monochromatic quarter-wave A-plates are proposed for transmissive LCDs [27]. This configuration shows an excellent viewing angle for the transmissive mode, but has a limited bandwidth if applied for the reflective mode. Therefore, there is an urgent need to develop a simple low-cost circular polarizer for transflective LCDs with both wide viewing angle and broad spectral bandwidth.

Here, we have developed a cost-effective, wide-view, and broadband circular polarizer configuration for transflective LCDs, where two circular polarizers can compensate with each other. In this configuration, each circular polarizer has a linear polarizer, a monochromatic uniaxial half-wave A-plate, and a monochromatic uniaxial quarter-wave A-plate, but the two

half-wave plates (and two quarter-wave plates) from different circular polarizers are made of uniaxial A-films with opposite optical birefringence. As a result, the off-axis phase retardation is self-compensated and light leakage is greatly suppressed. Over the entire $\pm 90^{o}$ viewing cone, the light leakage of the two stacked circular polarizers is less than 1.5×10^{-2} (normalized to the maximum transmission over two parallel linear polarizers) and contrast ratio is over 10:1 using a MVA LC cell.

In our analysis, we trace the polarization state of the incident light on the Poincaré sphere [28, 29] by solving the electric fields using the 2×2 matrix method (as discussed in above chapters) to get optimized results. The absorptive linear polarizer is modeled as a lossy uniaxial material. The phase retardation of the protective Tri-Acetyl-Cellulose (TAC) films is ignored. If not negligible, we can always add a positive C plate to compensate the phase of the negative C plate from the TAC film. The refractive indices of the liner polarizer and the uniaxial retardation films are listed as follows: $n_{e\_pol} = 1.5 + i \times 2.208 \times 10^{-3}$, $n_{o\_pol} = 1.5 + i \times 3.222 \times 10^{-5}$, $n_{e\_p\_A} = 1.5902$, $n_{o\_p\_A} = 1.5866$, $n_{e\_n\_A} = 1.50$, and $n_{o\_n\_A} = 1.60$ (at 550 nm). And the material birefringence dispersion is characterized by the extended Cauchy equations[30]:

$$n_{e,o} = A_{e,o} + \frac{B_{e,o}}{\lambda^2} + \frac{C_{e,o}}{\lambda^4} \tag{3}$$

Figure 3.12 depicts the cell structure of a typical transflective LCD, where each pixel is divided into a sub-T and a sub-R region. To achieve a dark state for the reflective mode, a broadband circular polarizer placed above the LC cell is necessary, which further requires a second circular polarizer be placed below the LC cell to achieve a common dark state between the T and R modes.

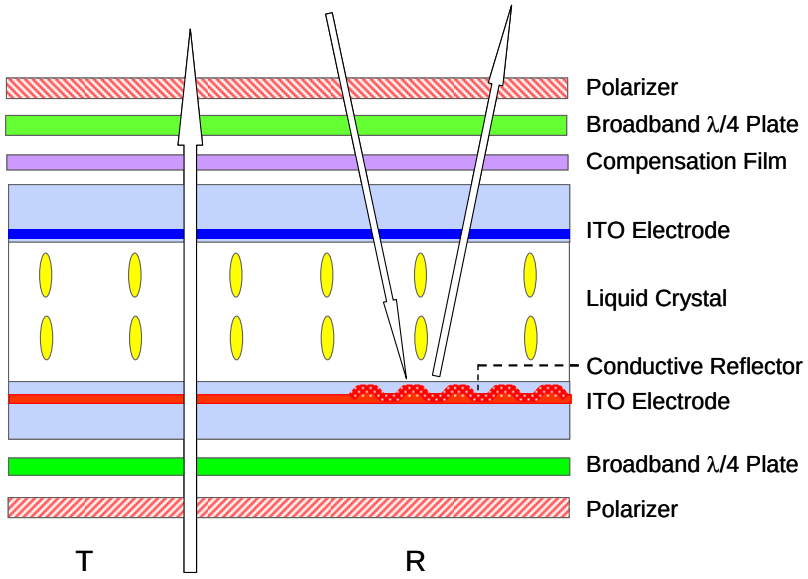

Figure 3.12: Schematic cell structure of a typical transflective LCD.

Figure 3.13(a) depicts the detailed configuration of the top and bottom conventional circular polarizers; each consists of a linear polarizer and two uniaxial positive birefringence A-films ($n_x > n_y = n_z$). Once the following condition is satisfied, the circular polarizer is a broadband device [9]:

$$2\varphi_{\lambda/4} - 4\varphi_{\lambda/2} = 90^{o}, \tag{4}$$

where $\varphi_{\lambda/2}$ and $\varphi_{\lambda/4}$ are the azimuthal angles between the optic axes of the half-wave plate and the quarter-wave plate and the transmission axis of the linear polarizer, respectively. If the transmission axis of a linear polarizer is along the x-axis, then $\varphi_{\lambda/2}$ is chosen to be 15° and $\varphi_{\lambda/4}$ =75°, as shown in Fig. 3.13(a) to minimize the light leakage of the crossed circular polarizers at different wavelengths.

Figure 3.13(b) depicts the polarization states on the Poincaré sphere when a light is

incident to the structure at normal direction. On the Poincaré sphere, the transmission axis of the bottom polarizer is represented by the point T, while point A represents the absorption axis of the top polarizer. Points T and A overlap with each other when the top and bottom polarizers are crossed. The incident light from the bottom polarizer is first rotated 30° from point T to another linear polarization state at point B (solid blue line) by the half-wave plate, then it is converted by the quarter-wave plate to a circular polarization on the north pole at point C (solid red line). This circularly polarized light at point C will be converted back to a linear polarization state at point A after traversing the top quarter-wave and half-wave plates, thus is blocked by the top linear polarizer, resulting in a dark state (their traces are overlapped with the previous lines). Here, $\varphi_{\lambda/2}$~15° is an optimal angle for minimizing the light leakage of a broadband light source. In Fig. 3.13(b), the arcs $\overline{TB}$ and $\overline{BC}$ can compensate with each other for the wavelength variation. The light leakage of these two crossed circular polarizers and the reflectance of the top circular polarizer alone are depicted in Fig. 3.13(c), where broad bandwidth is well maintained.

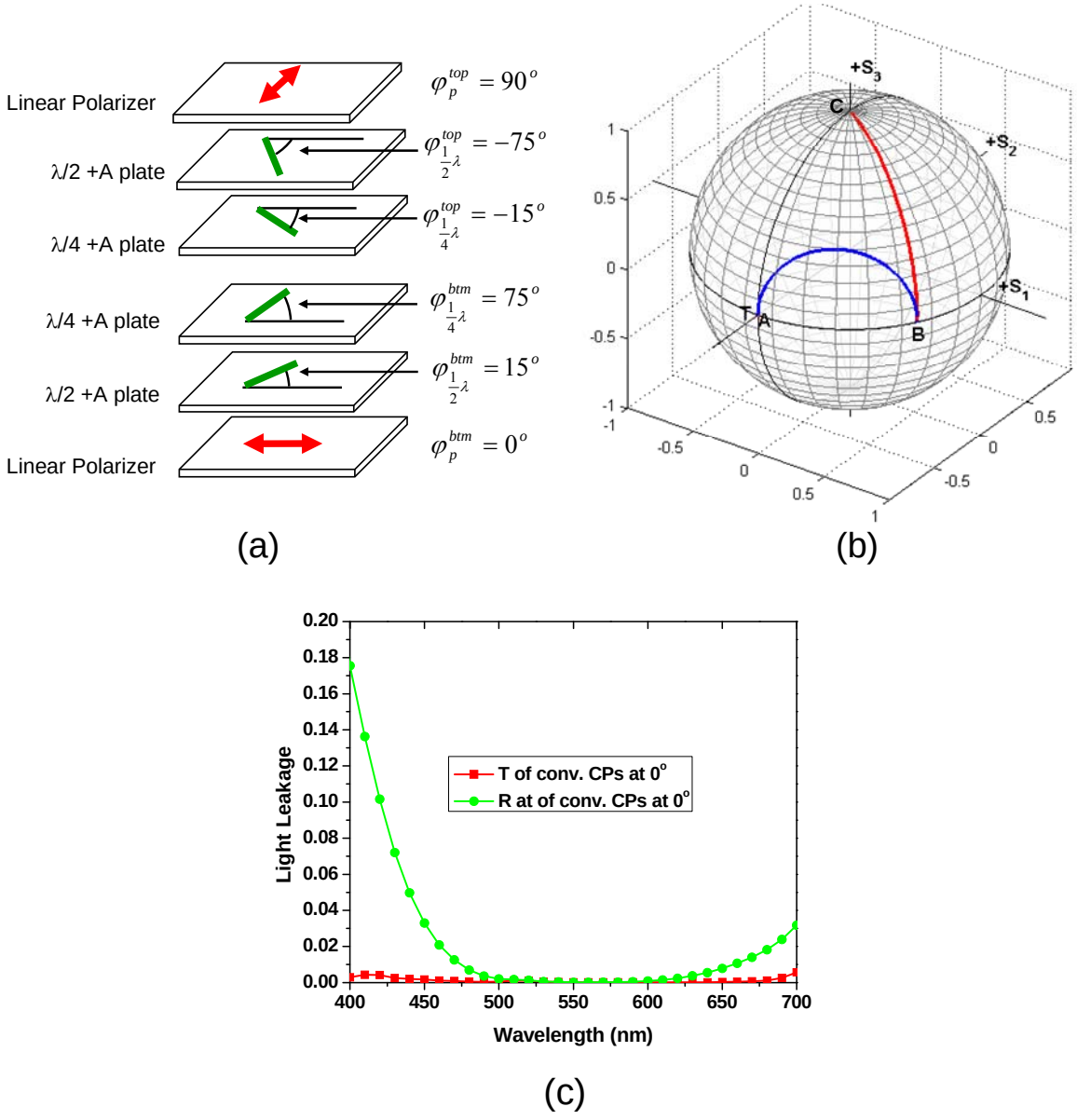

Figure 3.13: (a) Configuration of two crossed circular polarizers, (b) polarization state trace on the Poincaré sphere at $\theta_{inc} = 0°$, and (c) spectral light leakage.

However, at an oblique incident angle the phase retardations from these positive birefringence wave plates accumulate which separates the polarization traces from the bottom

and the top circular polarizers. Figure 3.14(a) shows the corresponding polarization state trace when incident angle θ_{inc} is equal to 40°. The final polarization state F just before the top linear polarizer departs far away from the absorption direction at point A, producing a large off-axis light leakage as Fig. 3.14(b) shows. Here the angular light leakages are normalized to the maximum transmittance of the two parallel linear polarizers at normal incidence. The light leakage at θ_{inc} ~40° is over 10%, which also indicates the viewing cone with contrast ratio over 10:1 is limited to ±40°, which is not enough for today's high performance transflective LCDs requiring wide-viewing angle. Here, the severe light leakage is attributed to two sources: 1) the disparity between the transmission axis of the top polarizer (point T) and the absorption axis of the bottom polarizer (point A) when viewed from an oblique direction, and 2) the off-axis phase retardation accumulation from the four positive A-plates.

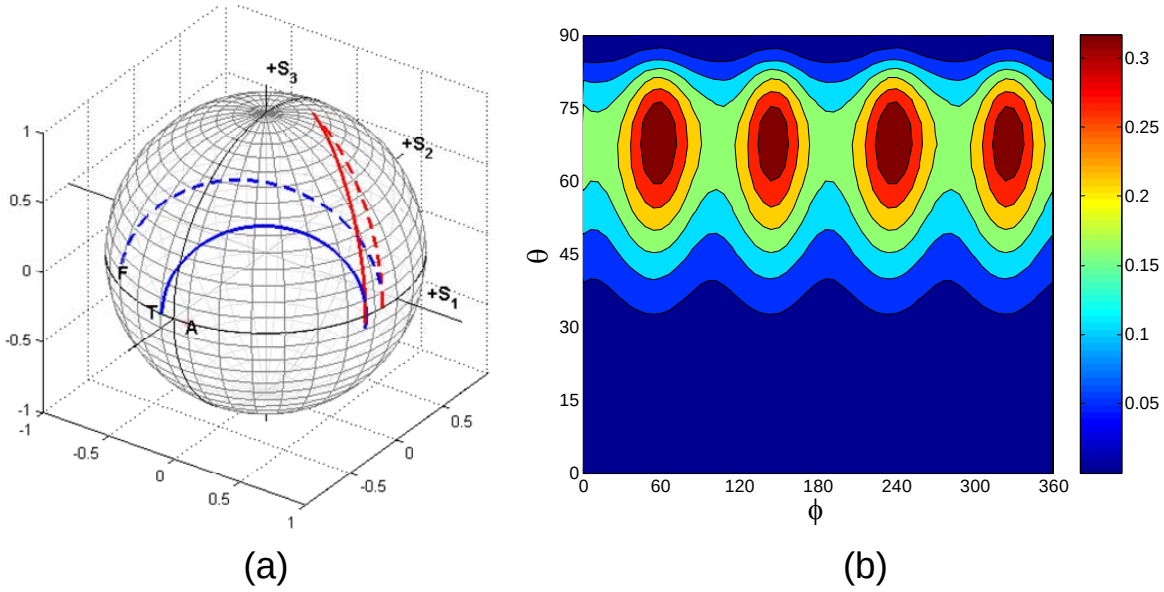

Figure 3.14: (a) Polarization state traces on the Poincaré sphere at θ_{inc} = 40° when viewed at φ_{inc} = -45° and (b) a plot of angle dependent light leakage.

3. 3. 2. Alternating Positive and Negative A-plates for Self-compensation

3. 3. 2. 1. General Design Principles

To minimize light leakage at oblique angles, we propose here to use opposite birefringence materials for the two half-wave and two quarter-wave plates. These positive and negative birefringence films will self-compensate the off-axis phase retardations and thus suppress the light leakage. From Fig. 3.13(a), different film combinations can be used from bottom to top, but they can be grouped into two categories: 1) same typed wave plates are employed within each circular polarizer, e.g., the bottom circular polarizer uses both positive (or negative) A-plates, and both negative (or positive) A-plates are employed in the top circular polarizer; and 2) opposite typed wave plates are employed within each circular polarizer, e.g., the bottom circular polarizer uses one positive (or negative) A-plate as its half-wave plate and one negative (or positive) A-plate as its quarter-wave plate, and the top circular polarizer correspondingly uses one negative (or positive) A plate as the half-wave plate and one positive (or negative) A plate as the quarter-wave plate.

To maintain the wide-view and broadband properties, three major requirements determine the orientation of their optic axes among these retardation films: 1) to compensate the off-axis phase retardation between two half-wave plates (or two quarter-wave plates) with opposite sign of birefringence, their optic axes need to be aligned close to each other; 2) to achieve broadband properties of each circular polarizer, the optic axis orientation of each half-wave plate and its adjacent quarter-wave plate need to satisfy a similar relationship to Eq. (4), as to be discussed

later; and 3) the top circular polarizer must be broadband to guarantee the spectral performance of the reflective mode, i.e., the angle between the optic axis of the top half-wave plate and the transmission axis of the top linear polarizer needs to be close to ±15° (or ±75°). In the following sections, we will use the Poincaré sphere to derive their angular relations according to different film combinations. For convenience, the transmission axis of the bottom linear polarizer is set along x-axis, and the top polarizer is always crossed to the bottom one. Here the discussion is based on the two main categories of wave plate combinations and the angle between the optic axis of the top half-wave plate and the top linear polarizer is taken to be close to ±15°.

3. 3. 2. 2. Same Typed Wave Plates within Each Circular Polarizer

Figure 3.15(a) shows the film configuration of a wide-view and broadband circular polarizer, where the top half-wave plate is a negative A-plate with its optic axis aligned at $\varphi_{\lambda/2}^{btm} = 75^o$ with respect to the x-axis, which is also -15o away from the transmission axis of the top polarizer. Accordingly, the angle $\varphi_{\lambda/2}^{btm}$ of the bottom half-wave positive A-plate is at ~75°. The orientation of the optic axis of the quarter-wave plate can be determined with assistance of the Poincaré sphere.

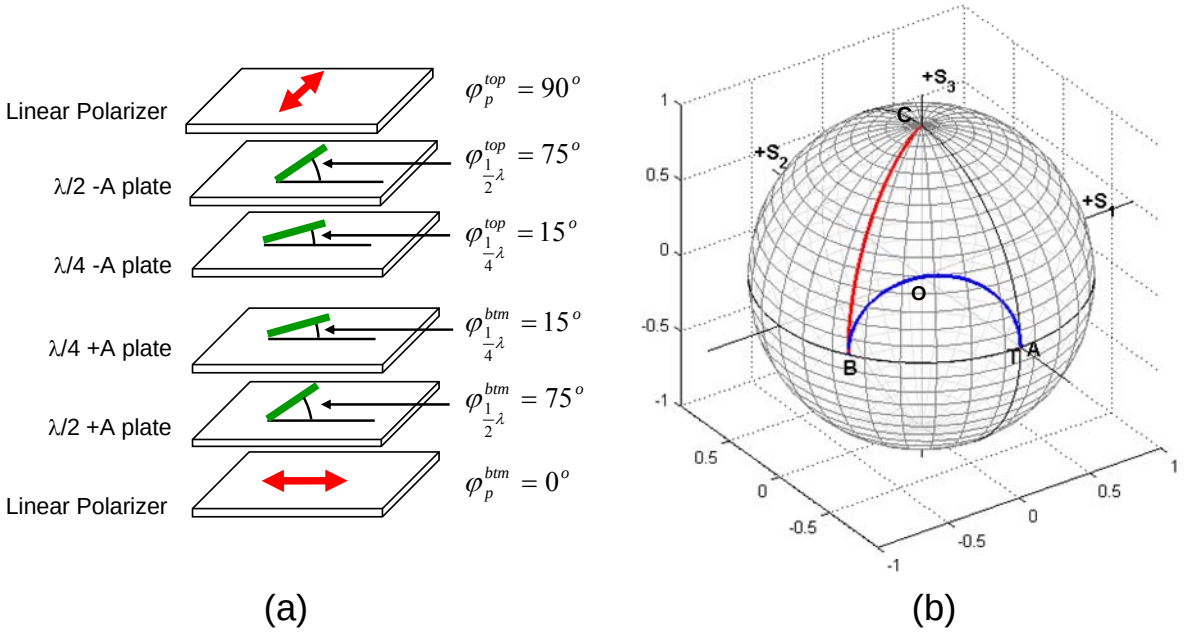

Figure 3.15: (a) Crossed wide-view and broadband circular polarizers using positive and negative A-plates, and (b) Polarization state traces on the Poincaré sphere at $\theta_{inc} = 0°$.

Figure 3.15(b) shows the polarization state traced on the Poincaré sphere at normal incidence, where the transmission axis of the bottom polarizer (point T) overlaps with the absorption direction (point A) of the top polarizer. On the Poincaré sphere, the optic axes of the bottom half-wave plate and quarter-wave plate are at $2\varphi_{\lambda/2}^{btm}$ and $2\varphi_{\lambda/4}^{btm}$ with respect to the axis OT on the equator [29] The linearly polarized light from the bottom polarizer is first rotated by the bottom half-wave plate to point B by $4\varphi_{\lambda/2}^{btm}$ ($\angle$BOT = 300°). In order to assure the broadband property, the following quarter-wave plate made of a positive A-film must transfer the polarization from point B to the north pole C into the upper semi-sphere, making the arc $\overline{TB}$ and arc $\overline{BC}$ compensate to each other. From the geometry relations on the equator, the optic axis of

the bottom quarter-wave positive A-plate at $2\varphi_{\lambda/4}^{btm}$ needs to be 90° ahead of the axis OB at $4\varphi_{\lambda/2}^{btm}$. Thus, a general relation between these angles is derived as follows:

$$2\varphi_{\frac{1}{4}\lambda} - 4\varphi_{\frac{1}{2}\lambda} = 90^o + 2m\pi, \tag{5}$$

where m is an integer which could be 0, and ±1. For the angles plotted in Fig. 3.15(a), m=-1. The circularly polarized light at point C is transferred back to point A by the top half-wave and quarter-wave plates, and blocked by the top linear polarizer. As a result, a good dark state is obtained.

On the other hand, if $\varphi_{\lambda/2}^{top} = -75^o$, or the optic axis of the top half-wave plate +15° ahead of the transmission axis of the top polarizer, as shown in Fig. 3.16(a). The general relation between the optic axes of the half-wave positive A-plate and quarter-wave positive A-plate within each circular polarizer needs to satisfy the following relation:

$$2\varphi_{\frac{1}{4}\lambda} - 4\varphi_{\frac{1}{2}\lambda} = -90^o + 2m\pi, \tag{6}$$

where m is an integer which could be 0, and ±1. In Fig. 3.16(a), we show the films configuration for $m=1$. In this case, all the traces are confined to the bottom semi-sphere, as shown in Fig. 3.16 (b) to maintain a broadband operation.

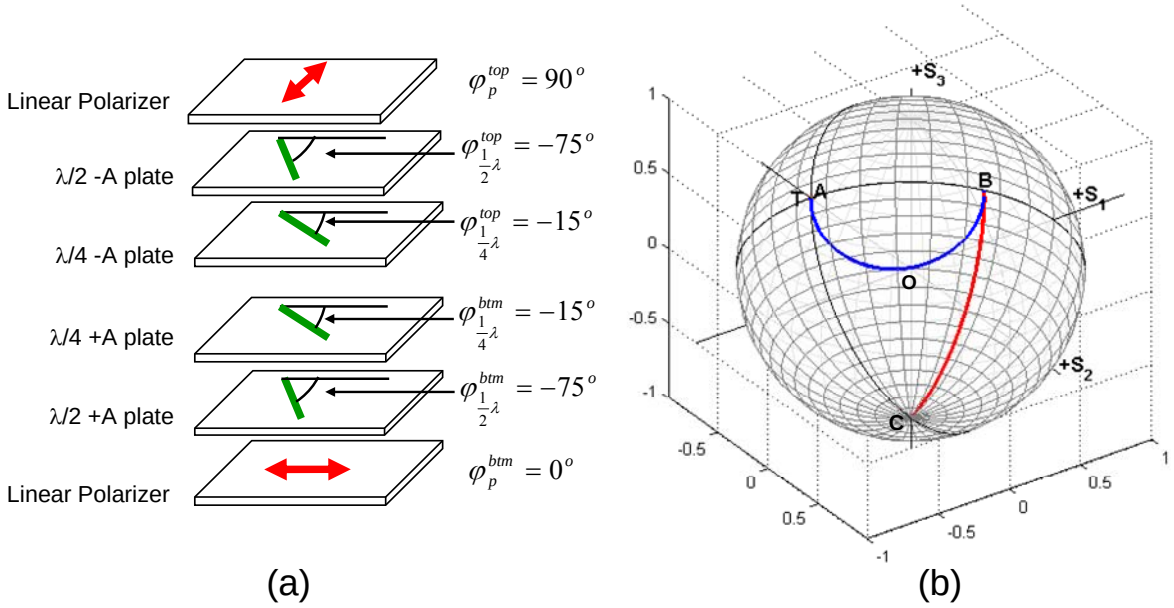

Figure 3.16: (a) Films configuration of two crossed wide-view and broad band circular polarizers, and (b) polarization state traces on the Poincaré sphere at $\theta_{inc} = 0°$.

3. 3. 2. 3. Opposite Typed Wave Plates within Each Circular Polarizer

Figures 3.17(a) and (b) show another two possible configurations for the wide-view and broadband circular polarizers with alternating positive/negative uniaxial A-plates. To maintain broadband in the entire visible spectral region, when the optic axis of the top half-wave plate is at -15° from the transmission axis of the top polarizer, i.e., $\varphi_{\lambda/2}^{top} = 75^o$ with respect to the x-axis, the optic axes of the half-wave plate and quarter-wave plate need to satisfy Eq. (6). On the other hand, these axes need to satisfy Eq. (5) when the top half-wave plate has its optic axis aligned at $\varphi_{\lambda/2}^{btm} = -75^o$ to the x-axis, which is also +15° ahead of the transmission axis of the top polarizer.

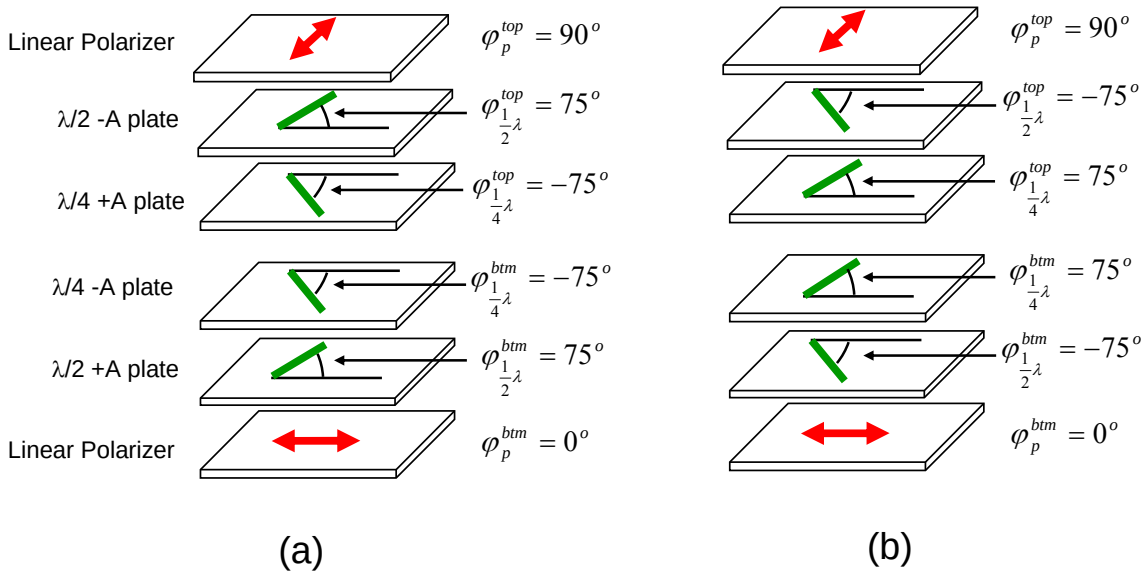

Figure 3.17: Films configuration of wide-view and broad band circular polarizer with top half-wave plate having its optic axis at (a) -15° and (b) 15° from the transmission axis of the top polarizer.

Although there are several configurations, the two in Figs. 3.17(a) and 6(b) would have better off-axis performance for the reflective mode than those in Figs. 3.15(a) and 3.16(a), because self-compensation from the opposite sign of birefringence between the two wave plates also exist in the top circular polarizer. Therefore, in the following sections only the configuration in Fig. 3.17(a) will be used as examples for illustrating our design principles. Other designs including the configurations shown in Figs. 3.15(a) to 3.17(b) also work as broadband and wide-view circular polarizers for a transflective LCD. However, their analysis is similar so that their results are not included here.

3. 3. 3. Results and Discussion

3. 3. 3. 1. Spectral Bandwidth and Off-axis Light Leakage

Figure 3.18 shows the simulated wavelength-dependent light leakage for configuration in Fig. 3.17(a) at normal (Fig. 3. 18(a)) and off-axis (Fig. 3. 18(b)) viewing directions. The spectral performance for both T and R modes in the new design at normal incidence are quite similar to those in the conventional circular polarizers as shown in Fig. 3.13(c), but their mechanisms are different. For the transmissive mode, in the conventional one the broad bandwidth is achieved by setting the top and bottom half-wave plates orthogonal to each other. But in the new design, positive and negative A-plates are employed to compensate each other.

The difference in their off-axis performances is quite evident. The new design in Fig. 3.17(a) using opposite birefringence A-plates has much better off-axis compensation. The light leakages viewed at polar angle $\theta_{inc} = 80°$ and azimuthal angle $\varphi_{inc} = 0°$ are almost identical to the one from the normal direction at $\theta_{inc} = 0°$. The conventional circular polarizer, on the other hand, produces a ~5% light leakage in the whole visible spectrum, when viewed even from $\theta_{inc} = 40°$. For R mode, the new design shows a lower light leakage in most of the visible spectrum than the conventional one when viewed at $\theta_{inc} = 40°$, as shown in Fig. 3.18(b). For the R mode, through its double passing of the top circular polarizer, the light always views a same typed half-wave plate and a same typed quarter-wave plate. Although there is still self-compensation by opposite birefringence between the half-wave and quarter-wave plates, that cannot cancel each other as well as that for the transmissive mode, which can be clearly seen from Figs. 3.18(a) and 3.18(b).

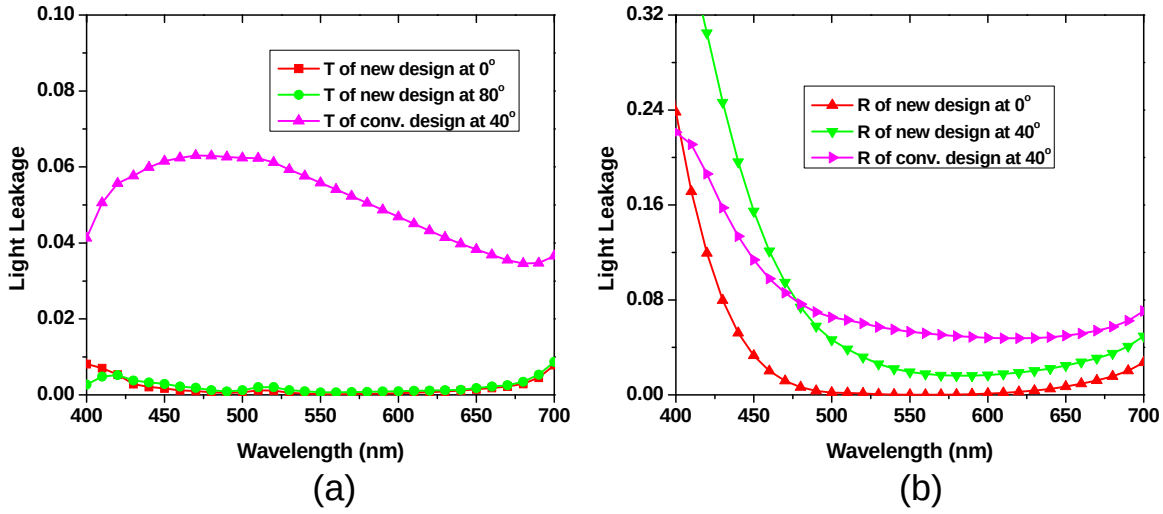

Figure 3.18: Spectral light leakage from (a) T mode and (b) R mode viewed at $\varphi_{inc} = 0°$.

Figure 3.19(a) shows the polarization trace on the Poincaré sphere when viewed at $\theta_{inc} = 70°$ and $\varphi_{inc} = -45°$. It demonstrates a self-compensation by opposite birefringence in the uniaxial A-plates, indicating by the fact the final polarization state goes back to the initial polarization state at point T. Consequently, the off-axis light leakage only results from the disparity between the top and the bottom polarizers viewed from an oblique angle. As shown in Fig. 3.19(b), the maximum light leakage mainly occurs at the bisector direction at $\varphi_{inc} \sim \pm 45°$ and $\pm 135°$. Over the entire viewing cone, the maximum light leakage is suppressed to below ~3.5% which is much better than that in the conventional circular polarizer.

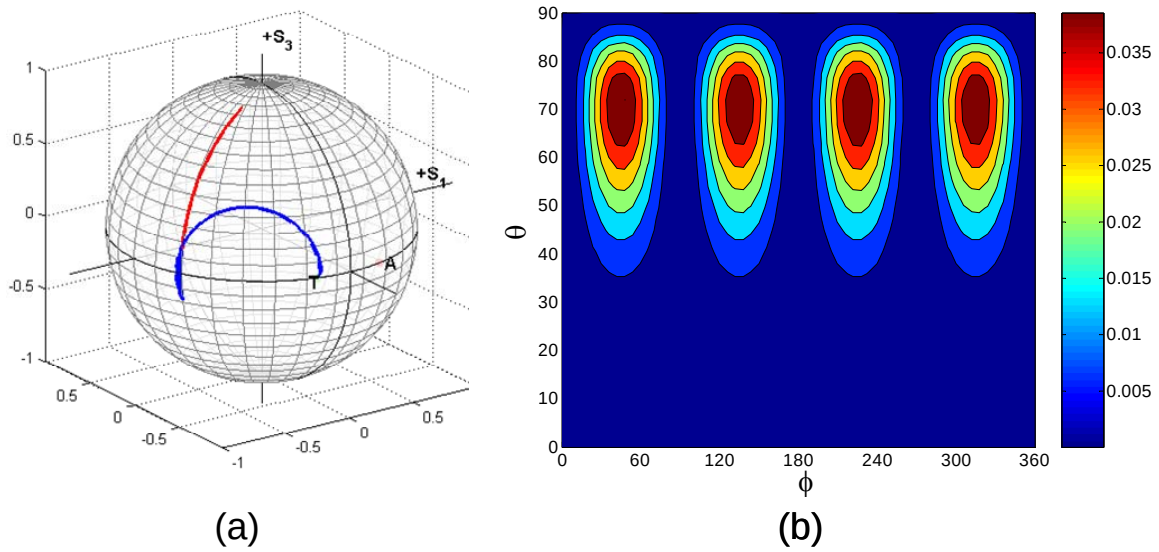

Figure 3.19: (a) Polarization state trace on the Poincaré sphere when viewed at θ_{inc} = 70° and φ_{inc}= -45° and (b) light leakages.

Nevertheless, the off-axis light leakage can be further reduced by optimizing the film parameters. Detailed discussion is given in the following section for a case study using the designed circular polarizers in conjunction with a normally black VA cell.

3. 3. 3. 2. Viewing Angle Including a Liquid Crystal Cell

The aforementioned circular polarizer configuration is applied to a transflective LCD using a vertically aligned LC cell. The structure is shown in Fig. 3.20(a) where a negative C-plate is added to compensate the LC phase retardation at oblique angles. The LC material employed is Merck MLC-6608 with ordinary and extraordinary refractive indices n_o = 1.4789 and n_e = 1.5622 at λ = 546 nm [31], and the cell gap is set at 4 μm. The negative C-plate has its

ordinary and extraordinary refractive indices n_e = 1.5028 and n_o = 1.4929 at λ = 550 nm. The overall light leakage from Fig. 3.19(b) can be further suppressed by optimizing the film parameters, which involves a minimization of light leakage at two directions: the bisector direction with $\varphi_{inc} = \pm 45°$ and the one with $\varphi_{inc} = 0°$ and 90°. The optimization mechanism will be described in the following paragraph. For an optimized configuration shown in Fig. 3.20(a), we found the thicknesses of the half-wave and quarter-wave plates needs to be designed at a shorter wavelength with λ ~ 470 nm, the phase retardation value of the negative C film is set at dΔn ~ -368 nm at λ = 550 nm, and the optic axes of the top and bottom half-wave plates are aligned ±2° apart from their initial values, while two orientation angles still satisfy Eq. (5) within each circular polarizer. Accordingly, as shown in Fig. 3.20(b), a light leakage less than 1.5×10^{-2} is obtained throughout the entire viewing cone for the parameters shown in Fig. 3.20(a).

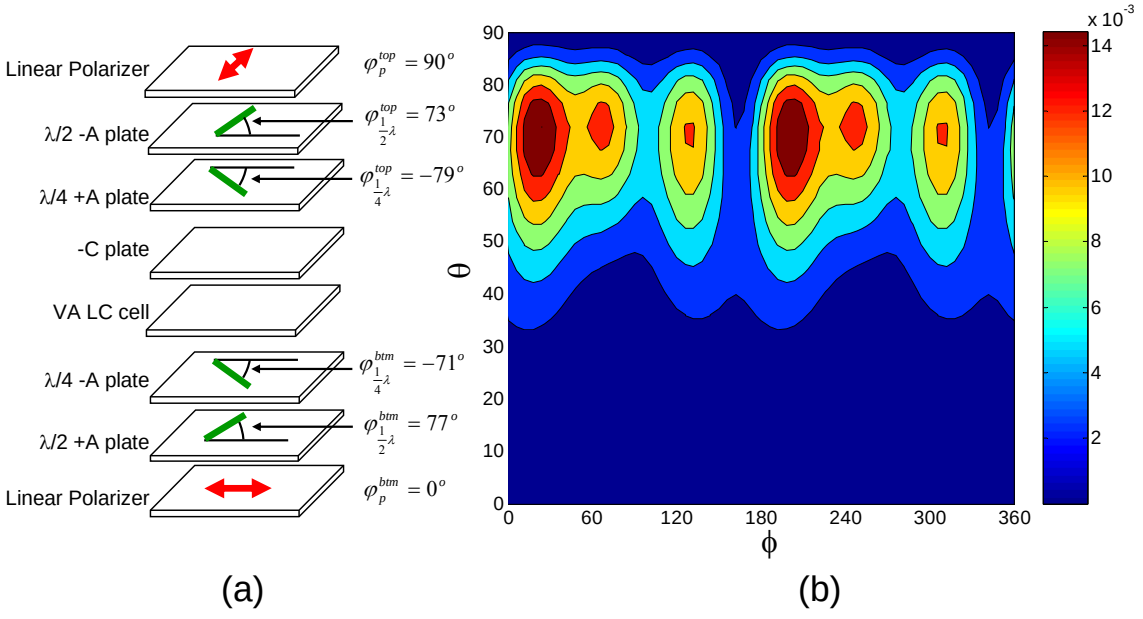

Figure 3.20: (a) Device configuration of the optimized VA transflective LCD and (b) its corresponding light leakages.

The compensation mechanism involved in Fig. 3.20(a) for achieving small global light leakage is illustrated by Figs. 3.21(a) and (b), where the polarization of the incident light is traced on the Poincaré sphere when viewed at both (θ_{inc} = 70°, φ_{inc} = -45°) and (θ_{inc} = 70°, φ_{inc} = 0°). At φ_{inc} = -45° (the bisector direction), the absorption axis of the top polarizer (at point A) and transmission axis of the bottom polarizer (at point T) departs from each other. The incident light from the bottom linear polarizer is first moved from point T to point B by the bottom half-wave and quarter-wave plates. After passing the LC cell which performs like a positive C plate, it moves to point C. The following negative C-plate moves it to point D in an opposite direction, which is intentionally designed to be away from point B. Subsequently, the top quarter-wave plate and half-wave plates further move the light from point D to point F, which is much closer to point A than that in Fig. 3.19(a).

On the other hand, when viewed at φ_{inc} = 0° where point T and point A overlap, the separation between points B and D makes the final polarization at point F away from point A (while F goes back to point A at φ_{inc} = 0° in Fig. 3.16(a) as indicated by Fig. 3.18(a), if no LC layer and additional C film are included). In other words, the compensation at these two directions contradicts each other, and a trade-off between them needs to be considered, which results in the configuration in Fig. 3.20(a).

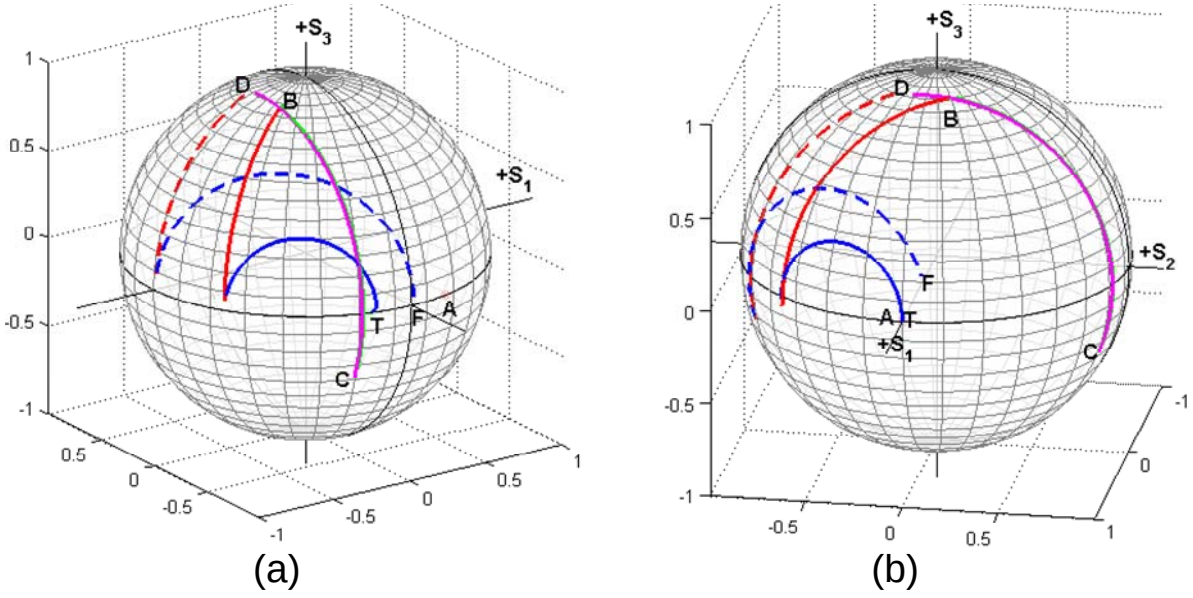

Figure 3.21: Polarization state trace on the Poincaré sphere at $\theta_{inc} = 70°$ when viewed at (a) $\varphi_{inc} = -45°$ and (b) $\varphi_{inc} = 0°$.

The spectral performance is shown in Fig. 3.22(a), where a shifted design central wavelength to λ = 470 nm improves the performance of the reflective mode. With a less light leakage, the viewing angle of a two-domain VA cell would extend the 10:1 contrast ratio to the entire viewing cone, as depicted in Fig. 3.22(b). Without introducing additional uniaxial films (two uniaxial films in each broadband circular polarizer) or biaxial films, this design greatly enhances the viewing angle of a transflective MVA LCDs while maintaining a broadband operation for both T and R modes. This design produces further possibility for MVA technology to be applied in high-end mobile displays.

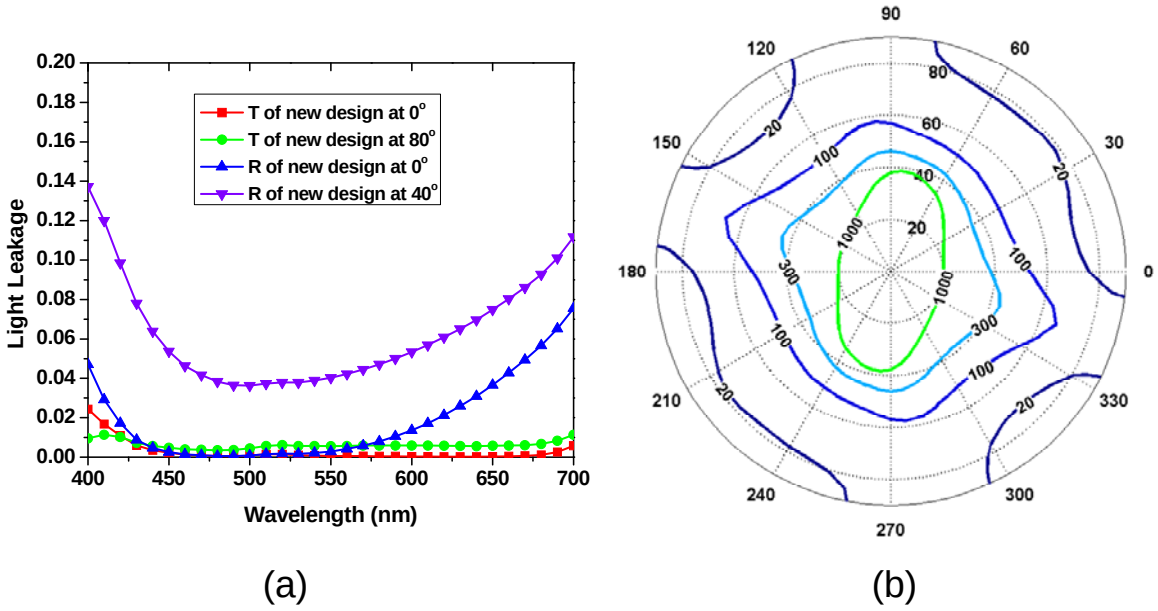

Figure 3.22: (a) Simulated spectral light leakages and (b) viewing angle.

In summary, we developed a simple and cost-effective circular polarizer configuration to achieve wide viewing angle and broad bandwidth for transflective liquid crystal displays. The alternating positive and negative birefringence uniaxial A-plates within the half-wave plate pair and the quarter-wave plate pair help to compensate the off-axis phase retardation. From our analysis, a normally black VA transflective LCD using our design could suppress the off-axis light leakage less than 1.5×10^{-2} and obtain a contrast ratio over 10:1 throughout the entire viewing cone. Its application into wide-viewing angle transflective LCDs is foreseeable.

3. 4. Wide-view Circular Polarizers Using Uniaxial Quarter-wave Plates and One Biaxial Plate

3. 4. 1. Motivations

Multi-domain vertically aligned liquid crystal display has been widely used in LCD TVs and monitors, owing to its inherently high contrast ratio and rubbing free process. A typical MVA cell is depicted in Figs. 3.23(a) (dark-state) and 3.23(b) (bright state). In the LC cell, protrusions on the top substrate and slits in the bottom substrate are formed periodically. When no voltage is applied to the pixel electrodes, all the liquid crystal molecules are substantially perpendicular to the substrate, resulting in a dark state with extremely low light leakage in the normal incidence. When a high voltage is applied between the electrodes, electric fields like the dashed lines will be generated in the cell, which tilt the LC molecules to exhibit a bright state under a two-domain distribution. The number of domains can further increased by forming chevron typed protrusions and slits in the x-y plane, as shown in Fig. 3.23(c). With 4 domains in this cell, the viewing angle of this display can be widely expanded compared to that of a single domain structure.

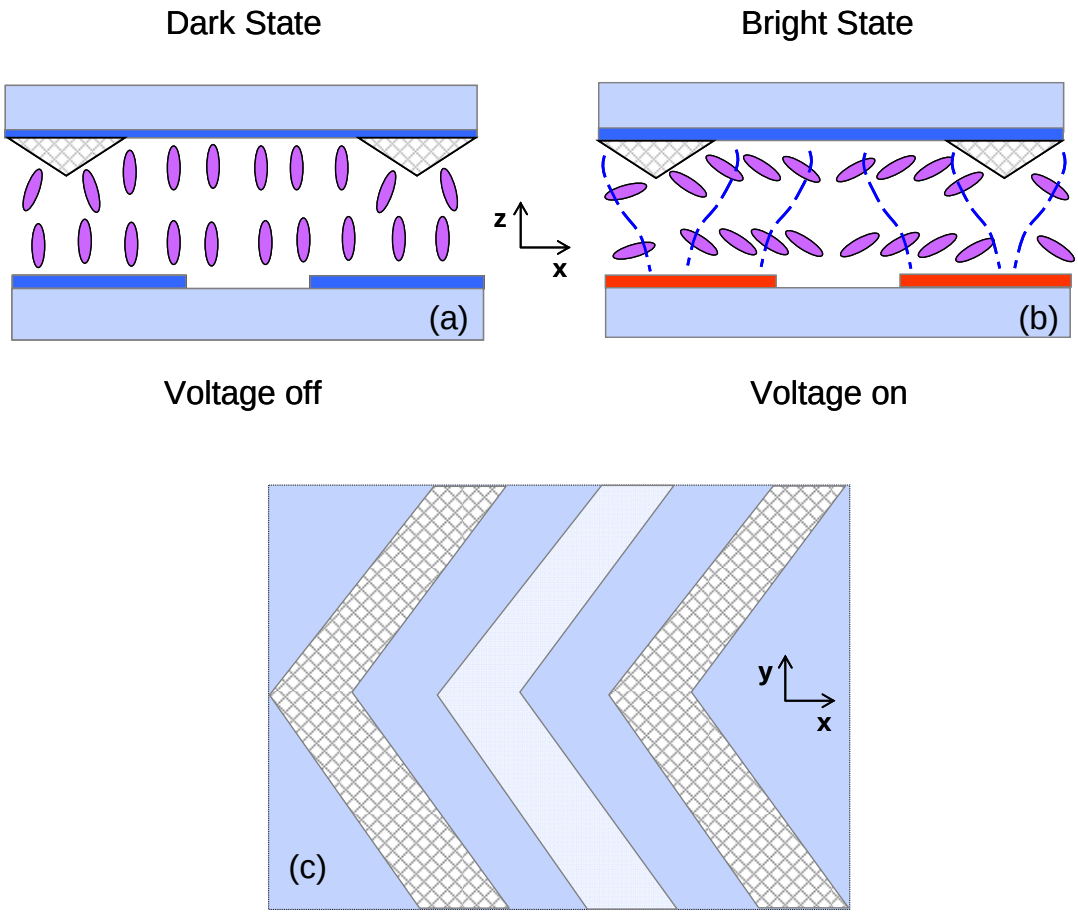

Figure 3.23: (a) cross-section of a MVA cell at voltage-off state, (b) cross-section of a MVA cell at voltage-on state, and (c) top view of the MVA cell

However, an issue related to this multi-domain structure is the reduced light efficiency under crossed linear polarizers. In a conventional MVA cell, the bottom and top linear polarizers are usually aligned at the x-axis and the y-axis, respectively. Ideally, the light efficiency can be maximized if all the LC molecules fully tilt down to four bisect directions ($\pm 45^{o}$ and $\pm 135^{o}$). Because the electric fields near the protrusion and slit regions are not uniform, the azimuthal angle of the LC molecules there deviates away from these four bisect directions, resulting in a

light loss under crossed linear polarizers. And the light efficiency can be calculated by the following equation, which is dependent on both phase retardation δ of the LC cell and the azimuthal direction ϕ.

$$T = \sin^2(2\phi)\sin^2(\frac{\delta}{2}). \quad (7)$$

Using circular polarizer can remove the dependence on the azimuthal directions, where the light efficiency is equal to:

$$T = \sin^2(\frac{\delta}{2}). \quad (8)$$

The corresponding transmittance is plotted in Fig. 3.24(a) (under linear polarizers) and Fig. 3.24(b) (under circular polarizers). And an improvement of about 30% is obtained.

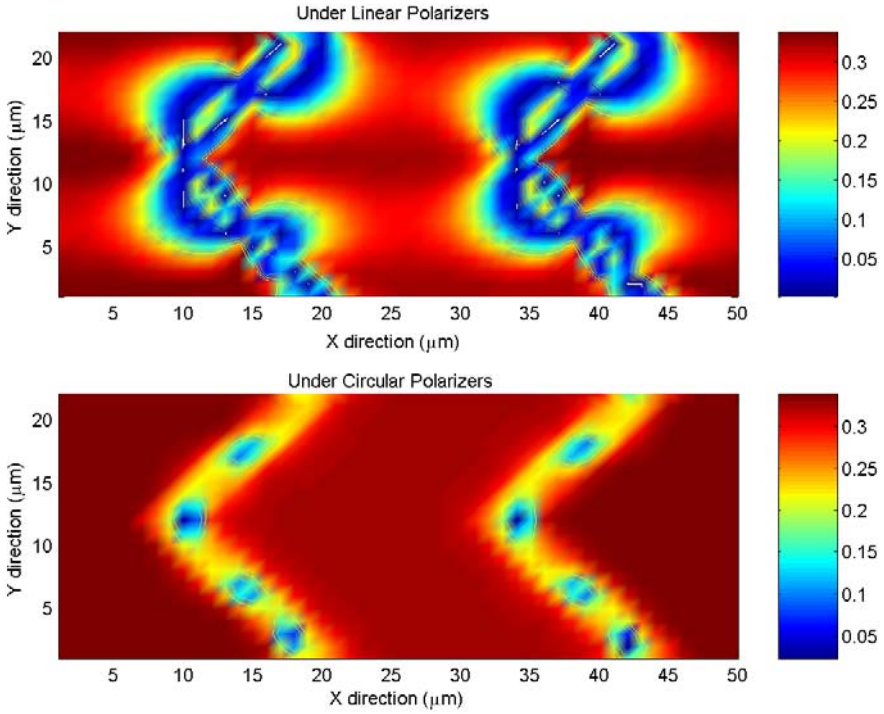

Figure 3.24: Brightness of a MVA cell under (a) linear polarizers and (b) circular polarizers.

However, the viewing angle of MVA cells under circular polarizer is inferior to that under linear polarizers. Thus there is an urgent need to design high performance circular polarizers that can make the MVA cells have comparable performance as they are used under linear polarizers. The simplest conventional circular polarizer consists of a linear polarizer and a quarter-wave plate, where the optic axis of the quarter-wave plate is set at 45^{o} away from the transmission axis of the linear polarizer, as shown in Fig. 3.25. Besides, negative C-plates are always required to compensate the phase retardation of the liquid crystal layer. A drawback is its narrow viewing angle when applied in LCDs.

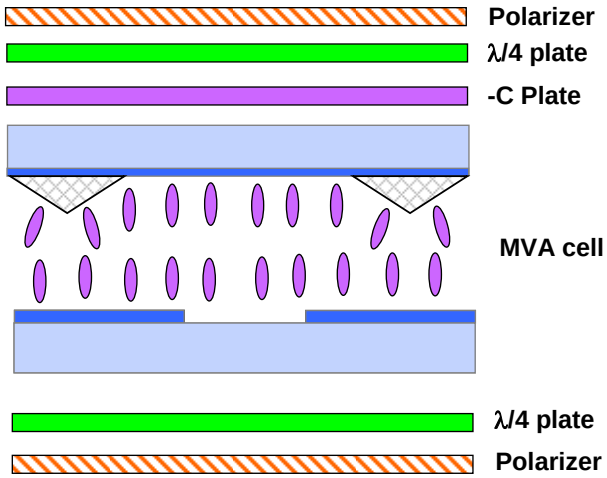

Figure 3.25: Configuration of a MVA cell

3. 4. 2. Design Concept and Theoretical Analysis

In order to understand the origins for large off-axis light leakage, the change of polarization state of the incident light through the LC system is traced on the Poincaré sphere.

Figures 3.26(a) and (b) represent two different azimuthal directions of the incident light at φ_{inc} = 0° and φ_{inc} = 45°, while the incident polar angle θ_{inc} are kept at 70° for both cases. At φ_{inc} = 0° and θ_{inc}=70° in Fig. 3.26(a), the transmission axis of the bottom polarizer at point T overlaps the absorption direction of the top linear polarizer at point A. The light that transmits the first linear polarizer will have an initial linear polarization at point T, then it is moved to the point B by the bottom quarter-wave plate; because here the phase of the LC layer is fully compensated by the negative C film (so they are not included in the calculations), the light at point B will then be converted back to point F by the top quarter-wave plate. As a result, a large light leakage occurs at this direction. At φ_{inc} = -45° and θ_{inc}=70°, the point T and point A depart from each other, but the final light polarization at F is still quite far away from the absorption direction at point A, leading a light leakage there as well.

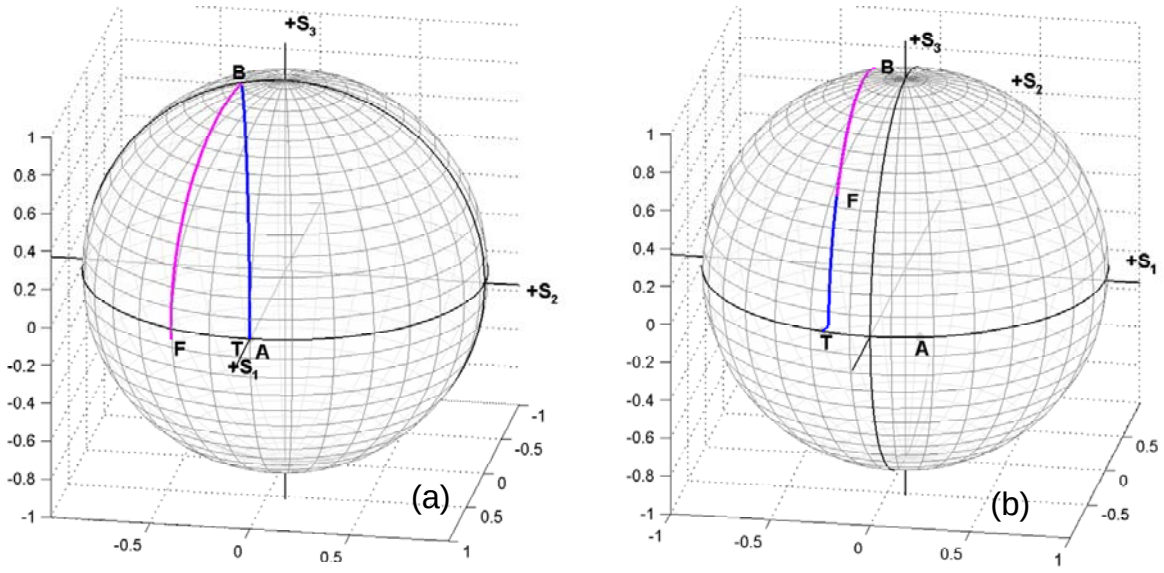

Figure 3.26: (a) Polarization state trace on the Poincaré sphere at θ_{inc} = 70° when viewed at (a) φ_{inc} = 0° and (b) φ_{inc} =-45°.

As is discussed in above section, using alternating positive and negative uniaxial A-plates to replace monochromatic quarter-wave plate can the greatly suppress the light leakage of the MVA LCD under circular polarizers, but at these two directions, a trade-off of compensation still exists. Thus it is not the optimum result. Nevertheless, off-axis light leakage can be fully suppressed if a biaxial plate is used. Figure 3.27 shows the compensation film schemes for the MVA cell using two circular polarizers. Here the two quarter-wave plates are both made of uniaxial A-plates, and are perpendicular to each other. The negative C plate is designed at a value to *partially* compensate the phase retardation of the LC layer. And the biaxial plate is inserted between the top linear polarizer and the quarter-wave plate, with its n_x axis aligned at a direction parallel to the absorption direction of the top linear polarizer.

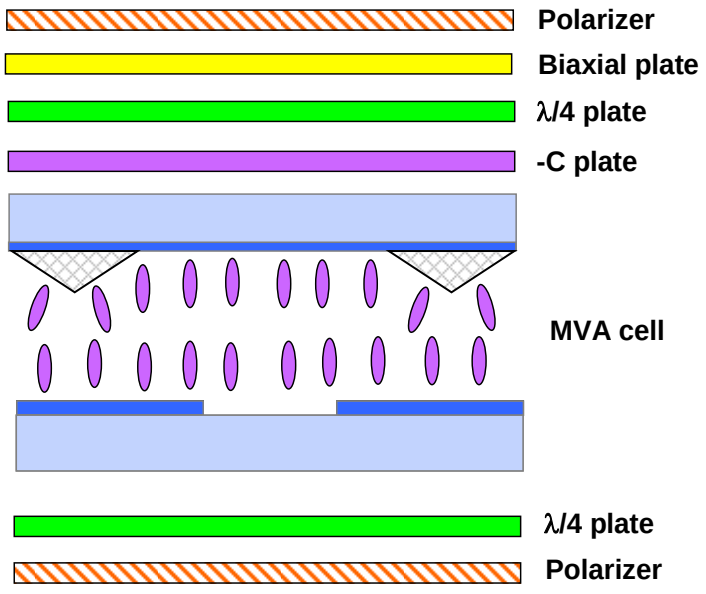

Figure 3.27: Schematic of MVA cell under the new circular polarizer with one more biaxial film.

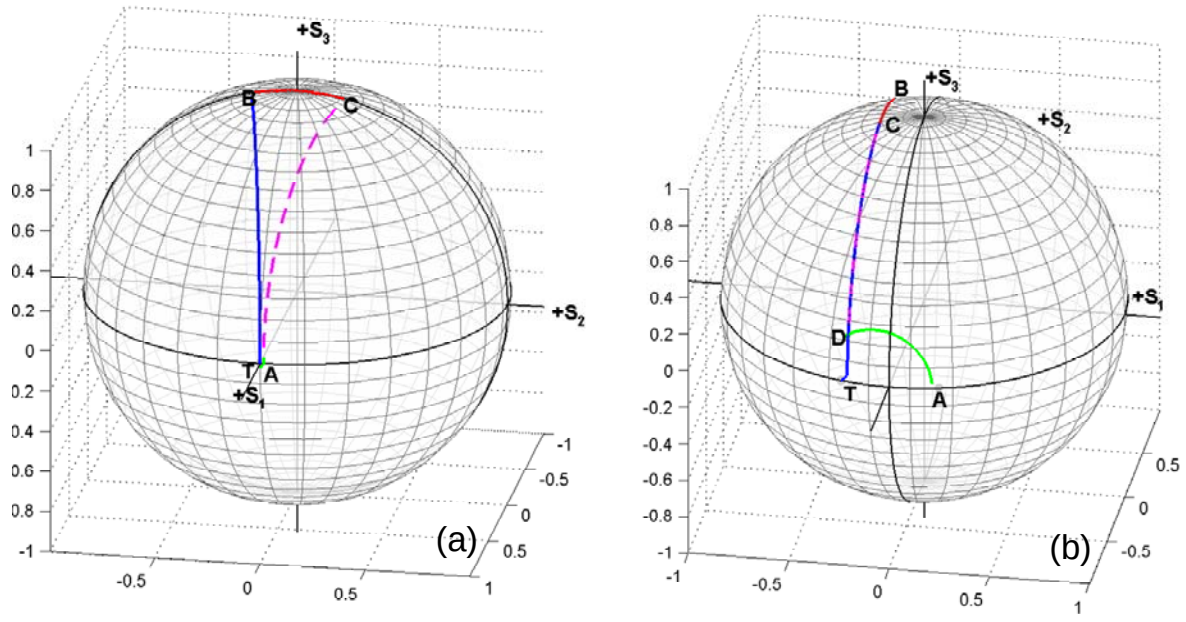

Figure 3.28: (a) Polarization state trace on the Poincaré sphere at $\theta_{inc} = 70°$ when viewed at (a) $\varphi_{inc} = 0°$ and (b) $\varphi_{inc} = -45°$.

The compensation mechanism is illustrated in Figs. 3.28(a) and (b), where the polarization change of the incident light is traced on the Poincaré sphere. Figure 3.28(a) shows the compensation at $\varphi_{inc} = 0^o$ and $\theta_{inc}=70^o$ by taking advantage of the overall positive C-plate effect from the LC layer and the negative C-plate. After passing the bottom linear polarizer, the light with a polarization state at point T will be moved to point B by the bottom quarter-wave plate; then by proper designing the negative C-plate, we can make the LC layer and its following negative C-plate to behave together like a positive C-plate, which can move the light from point B to point C; and then the following quarter-wave plate moves the light from point C to point A;

because the biaxial film has its n_x axis aligned at a direction parallel to the absorption direction of the top linear polarizer, it does not change the light polarization at point A, thus a perfect dark state at this direction (φ_{inc} = 0^o and θ_{inc}=70^o) can be obtained.

At the other direction with φ_{inc} = -45^o and θ_{inc}=70^o as shown in Fig. 3.28(b), the point T representing the transmission axis of the bottom polarizer departs from the point A representing the absorption axis of the top linear polarizer. The light passing the bottom linear polarizer will move from point T to point B after transmitting the bottom quarter-wave plate; then the overall positive C plate from the LC layer and the negative C plate thereafter further moves the light from point B to point C; and the top quarter-wave plate then moves it to point D; here the top biaxial film impacts and works to convert the light from point D to point A, leading a perfect compensation at this direction as well.

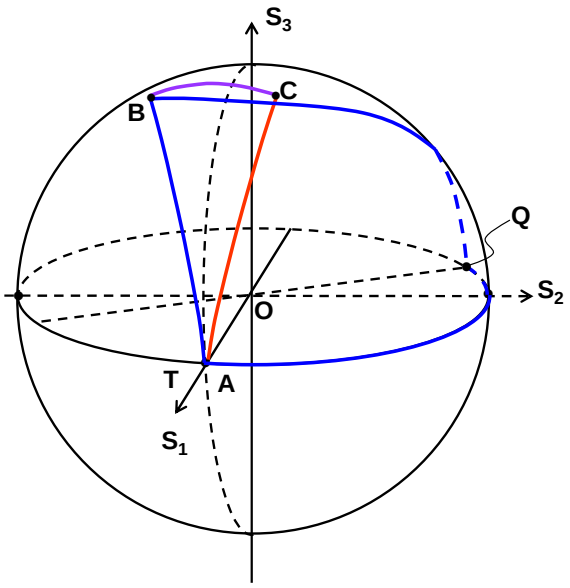

Figure 3.29: Spherical angle relations on the Poincaré sphere

From Fig. 3.28(a), we can analytically determine the phase retardation value of the negative C-plate, as the arc length of $\overline{TB}$ and $\overline{CA}$ are determined by the phase retardation value and related optic axis orientation of the two quarter-wave plates. The retardation value of this positive C-plate can be determined both analytically and numerically, if the arc $\overline{BC}$ can be determined. Figure 3.29 plots their spherical angle relations on the Poincaré sphere. Point T and point A stand for the main transmission axis of the bottom polarizer and the main absorption axis of the top polarizer, and they overlap with each other at $\varphi_{\text{inc}} = 0^{\text{o}}$ and $\theta_{\text{inc}}=70^{\text{o}}$. Point Q stands for the optic axis of the bottom quarter-wave plate, where $\angle$TOQ can be expressed by the following equation [29]:

$$\angle TOQ = \cos^{-1}\left[\frac{\sqrt{2}}{2}\frac{\sqrt{1-\sin^2(\theta_{inc})/n_p^2}}{\sqrt{1-\sin^2(\theta_{inc})/(2n_p^2)}}\right], \tag{9}$$

where $\theta_{\text{inc}}=70^{\text{o}}$ and n_{p} is the refractive index in the media, which can usually be taken as 1.5. From the parameters above, $\angle$TOQ = 52.07$^{\text{o}}$ and here the angle is in the xyz coordinate, not on the Poincaré sphere (a relation of 2X). In the spherical tri-angle QBT, arc $\overline{QB}$ is equal to arc $\overline{QT}$, and they are both equal to 2$\angle$TOQ (~1.817). The spherical angle $\angle$TQB is equal to the phase retardation of the quarter-wave plate, which can be obtained as:

$$\Gamma_a = \frac{2\pi}{\lambda}d\left[n_{e,A}\sqrt{1-\frac{\sin^2\theta_{inc}\sin^2(\phi_n-\phi_{inc})}{n_{e,A}^2}-\frac{\sin^2\theta_{inc}\cos^2(\phi_n-\phi_{inc})}{n_{o,A}^2}}-n_{o,A}\sqrt{1-\frac{\sin^2\theta_{inc}}{n_{o,A}^2}}\right], \tag{10}$$

where ϕ_{n} is the alignment angle of the quarter-wave plate that is equal to 45$^{\text{o}}$, and ϕ_{inc} is the incident azimuthal angle that is at 0$^{\text{o}}$; and $n_{\text{e,A}}$ and $n_{\text{o,A}}$ are the refractive indices for the quarter-

wave A-plate, which are set at 1.5902 and 1.5866, respectively. Therefore we can obtain the spherical angle ∠TQB about 92.08°. From spherical trigonometry, we can obtain the arc length of $\overline{BT}$ as follows

$$\overline{BT} = \cos^{-1}\left[\cos(\overline{QT})\cos(\overline{QB}) + \cos(\Gamma_a)\sin(\overline{QT})\sin(\overline{QB})\right], \quad (11)$$

And we can get $\overline{BT}$ as 1.5453. We can further obtain the spherical angle ∠BTQ to be around 104.21°. Because arc $\overline{TB}$ and arc $\overline{AC}$ are symmetric to each other, we can obtain ∠BAC as

$$\angle BAC = 2\angle BTQ - \pi, \quad (12)$$

which is equal to 28.41° and determines the required phase retardation value of the negative C-film. The phase retardation of the C-film can be determined by

$$\Gamma_c = \frac{2\pi}{\lambda} n_{o,C} d\left[\sqrt{1-\frac{\sin^2\theta_{inc}}{n_{e,C}^2}} - \sqrt{1-\frac{\sin^2\theta_{inc}}{n_{o,C}^2}}\right], \quad (13)$$

Therefore, if the refractive indices $n_{e,C}$ and $n_{o,C}$ for the positive C-plate are also set at 1.5902 and 1.5866, we can obtain the $\frac{d(n_{e,c}-n_{o,c})}{\lambda}$ value of the C plate is about 0.18. Besides, we found this value maintains almost a constant as the θ_{inc} changes from 1° to 89°. From our numerical simulation, we find that when $\frac{d(n_{e,c}-n_{o,c})}{\lambda}$ is close to 0.16 (due to the non-ideal linear polarizers), the overall compensation effect is the best, which match well with the analytical solution.

At the other incident direction at φ_{inc} = -45° and θ_{inc}=70°, with the fixed phase retardation value of the LC and negative C-plate, the polarization state of the incident light before it impinges on the top biaxial film is solely determined as the point D in Fig. 3.28(b). Therefore,

we can tune the N_z factor $\frac{n_x - n_z}{n_x - n_y}$ and the in-plane phase retardation $d(n_x - n_y)$ value of the biaxial film to convert the polarization to the absorption direction at point A. We find when the N_z is about 0.35 and $d(n_x - n_y)$ is about 0.34, the leakage is minimized.

3. 4. 3. Results and Discussion

For a 4-domain MVA cell using the above configured circular polarizers, the angular dependent light leakage is shown in Fig. 3.30(a), where the maximum value is about 4.5×10^{-4}. As a result, the viewing angle of this display in Fig. 3.30(b) is greatly enhanced to have contrast ratio 200:1 over the entire 80° viewing cone. Besides, as discussed above, the overall light efficient is improved by a factor of 30%.

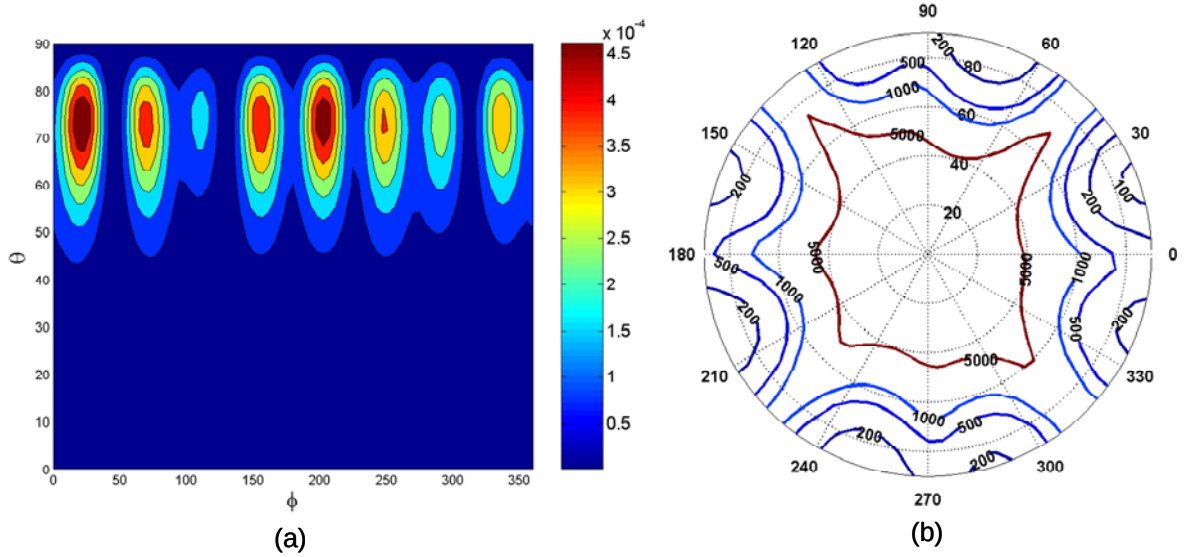

Figure 3.30: (a) angular dependent light leakage of the MVA using this new circular polarizer and (b) its iso-contrast plot

Because of the top circular polarizer (linear polarizer + a quarter-wave plate), this design can also be applied to the transflective LCDs, where part of each pixel region will have a reflector for the reflective functions. In this case, the MVA cell can easily generate a dark state under the circular polarizers.

In summary, we have developed a new circular polarizer that only includes two uniaxial quarter-wave plate one biaxial film for wide-viewing angle. The compensation principle of this circular polarizer has been discussed and the results match well with the numerical calculation. We believe this configuration is simplest design that shows excellent results for circular polarizers applied in MVA structure.

3. 5. Summary

In this chapter, we have developed a transflective LCD that use commonly biased reflectors in a VA cell to achieve high light efficiency. We further investigated the wide-viewing angle technology in transflective LCDs, which follows the two directions for achieving wide-viewing angle transflective LCDs: 1) designing transflective LCDs without circular polarizers, which employ a wide-viewing angle transmissive mode LC mode, like a FFS mode; and 2) developing wide-viewing angle circular polarizers, that can enhance viewing angle of transflective LCDs using MVA technology. Our designs in the TFT cell structure and optical configurations will have evident impacts in the transflective LCD technologies.

3. 6. References

1. X. Zhu, Z. Ge, T. X. Wu, and S. T. Wu, "Transflective liquid crystal displays," J. Display Technology 1, 15 (2005).
2. M. Okamoto, H. Hiraki, and S. Mitsui, "Liquid crystal display," U.S. patent 6,281,952 (2001).
3. S. J. Roosendaal, B. M. I. van der Zande, A. C. Nieuwkerk, C. A. Renders, J. T. M. Osenga, C. Doornkamp, E. Peeters, J. Bruinink, J. A. M. M. van Haaren, and S. Takahashi, "Nolve high performance transflective LCD with a patterned retarder," SID Symposium Digest 34, 78 (2003).
4. Y. J. Lee, H. R. Kim, T. H. Lee, J. W. Jung, J. H. Kim, and J. S. Choi, "Transflective LCD in a patterned vertically aligned mode with a single cell gap," SID Symposium Digest 37, 821 (2006).
5. Y. C. Yang, J. Y. Choi, J. Kim, M. Han, J. Chang, J. Bae, D. J. Park, S. I. Kim, N. S. Roh, Y. J. Kim, M. Hong, and K. Chung, "Single cell gap transflective mode for vertically aligned negative nematic liquid cyrstals," SID Symposium Digest 37, 829 (2006).
6. S. H. Lee, H. W. Do, G. D. Lee, T. H. Yoon, and J. C. Kim," A Novel Transflective Liquid Crystal Display with a Periodically Patterned Electrode," Jpn. J. Appl. Phys., Part 2, 42, L1455 (2004).
7. Y. J. Lim, J. H. Song, Y. B. Kim, and S. H. Lee, "Single Gap Transflective Liquid Crystal Display with Dual Orientation of Liquid Crystal," Jpn. J. Appl. Phys., Part 2, 43, L972 (2004).
8. J. H. Song, Y. J. Lim, M.-H. Lee, and S. H. Lee, and S. T. Shin, "Electro-optic characteristics and switching principle of a single-cell-gap transflective liquid-crystal display associated

with in-plane rotation of liquid crystal driven by a fringe-field," Appl. Phys. Lett. 87, 011108, (2005).

9. S. Pancharatnam, "Achromatic combination of birefringent plates. II. An achromatic quarter-wave plate," Proceedings of the Indian Academy of Science, A 41, 137-144 (1955).
10. A. Lien, "Extended Jones matrix representation for the twisted nematic liquid-crystal display at oblique incidence," Appl. Phys. Lett. 57, 2767 (1990).
11. Z. Ge, X. Zhu, T. W. Wu, and S. T. Wu, "Reflective liquid crystal displays with asymmetric incidence and exit angles," J. Opt. Soc. Am. A 22, 966 (2005).
12. S.H. Lee, S. L. Lee, and H. Y. Kim, "Electro-optic characteristics and switching principle of a nematic liquid crystal cell controlled by fringe-field switching," Appl. Phys. Lett. 73, 2881 (1998).
13. J. H. Song, Y. J. Lim, M.-H. Lee, S. T. Shin and S. H. Lee, "Electro-optic characteristics and switching principle of a single-cell-gap transflective liquid-crystal display associated with in-plane rotation of liquid crystal driven by a fringe-field," Appl. Phys. Lett. 87, 011108 (2005).
14. J. B. Park, H. Y. Kim, Y. H. Jeong, S. Y. Kim and Y. J. Lim, "Novel transflective display with fringe-field switching mode," Jpn. J. Appl. Phys. 44, 7524 (2005).
15. S. Hirota, S. Oka, and O. Itou, "Transflective LCD Combining Transmissive IPS and Reflective In-Cell Retarder ECB," Soc. Inform. Display Symposium Digest 38, 1661 (2007).
16. H. Imayama, J. Tanno, K. Igeta, M. Morimoto, S. Komura, T. Nagata, O. Itou and S. Hirota, "Novel pixel design for a transflective IPS-LCD with an in-cell retarder," Soc. Inform. Display Symposium Digest 38, 1651 (2007).
17. S. T. Wu, "Reflective and transflective liquid crystal display using a wire grid polarizer," U. S. Patent 6,977,702 B2 (2005).

18. Z. Ge, X. Zhu, and S. T. Wu, "A transflective liquid crystal display using an internal wire grid polarizer," J. Display Technology 2, 102 (2006).
19. R. T. Perkins, D. P. Hansen, E. W. Gardner, J. M. Thorne, and A. A. Robbins, "Broadband wire grid polarizer for the visible spectrum," U.S. Patent 6,122,103, (2000).
20. X. J. Yu and H. S. Kwok, "Optical wire-grid polarizers at oblique angles of incidence," J. Appl. Phys., 93, pp. 4407-4412 (2003).
21. D. P. Hansen and J. E. Gunther, "Dual mode reflective/transmissive liquid crystal display apparatus," U.S. Patent 5,986,730, (1999).
22. Z. Ge, X. Zhu, R. Lu, T. X. Wu, and S. T. Wu, "Transflective liquid crystal display using commonly biased reflectors," Appl. Phys. Lett., 90, 221111 (2007).
23. T. Ishinabe, T. Miyashita, and T. Uchida, "Design of a quarter wave plate with wide viewing angle and wide wavelength range for high quality reflective LCDs," Soc. Inf. Display Tech. Digest 32, 906-909 (2001).
24. H. Yoshimi, S. Yano, and Y. Fujimura, "Optical Films for Reflective LCDs to Achieve High Image Quality," Soc. Inf. Display Tech. Digest 33, 862-865 (2002).
25. Q. Hong, T. X. Wu, X. Zhu, R. Lu, and S. T. Wu, "Designs of wide-view and broadband circular polarizers," Opt. Express 13, 8318-8331 (2005).
26. Q. Hong, T. X. Wu, R. Lu, and S. T. Wu, "Wide-view circular polarizer consisting of a linear polarizer and two biaxial films," Opt. Express 13, 10777-10783 (2005).
27. C. H. Lin, "Extraordinarily wide-view and high-transmittance vertically aligned liquid crystal displays," Appl. Phys. Lett. 90, 151112 (2007).
28. S. Huard, *Polarization of Light* (Wiley, New York, 1997).

29. X. Zhu, Z. Ge, and S. T. Wu, “Analytical solutions for uniaxial-film-compensated wide-view liquid crystal displays,” J. Display Technology 2, 2-20 (2006).
30. J. Li and S. T. Wu, “Extended Cauchy equations for the refractive indices of liquid crystals,” J. Appl. Phys. 95, 896-901 (2004).
31. J. Li, C. H. Wen, S. Gauza, R. Lu, and S. T. Wu, “Refractive indices of liquid crystals for display applications,” J. Display Technology 1, 51-61 (2005).

CHAPTER 4: MODELING OF BEAM STEERING DEVICES

Liquid crystal material has also been widely applied in photonics devices, owing to its capability to provide variable phase profiles with the application of non-mechanical control means such as electrical voltages, thus making the device compact size, light weight, high resolution, and low power consumption. Dorschner, Resler, and McManamon et al[1-4] proposed to use liquid crystal materials into optical phased array (OPA) structures for laser beam steering. In this type device as shown in Fig. 4.1, the unfolded phase profile across the aperture can be approximated by a series of stair-step ram phase delays. The phase ramp, or its equivalent mod-2π saw-tooth profile, further can be approximated by a series of discrete phase steps, as long as the steps are small [1]. Figure 4.2 depicts each small ramp or period, where the LCs are sandwiched between two substrates, a transparent plane common electrode is coated on the top substrate, and patterned electrodes are formed on the bottom substrate periodically. By applying a gradient voltage on the bottom driving electrodes, the LC director orientation at each electrode can be controlled to form a gradient of refractive index of the LCs, achieving the phase profile of a 2π ramp in each single period. The incident linearly polarized light then experience different phase velocities at each electrode across the cell region. Thus this periodic phase delay at different positions will deflect the light away from its initial incident direction.

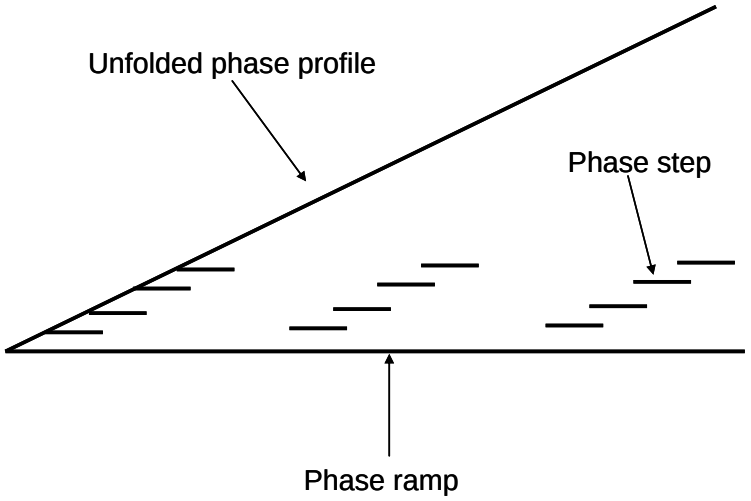

Figure 4.1: Unfolded phase profile achieve by saw-tooth like ramps

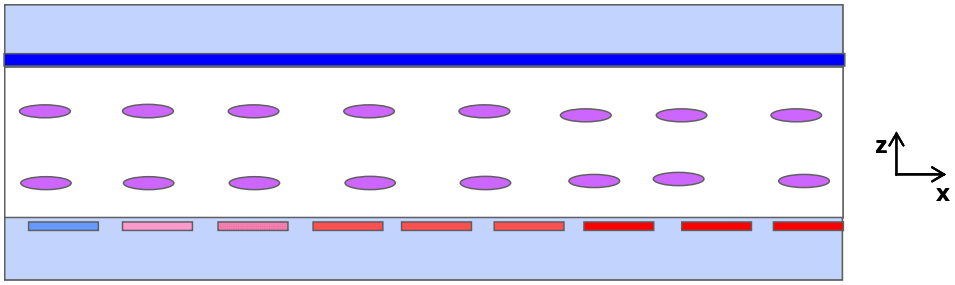

Figure 4.2: One period of LC based phase ramp

One of the key performance factors of these devices is the maximum diffraction efficiency at a specific deflection angle. For a fixed period length, the first order deflection angle can be determined from this mod 2π phase ramp is determined by $\sin\theta = \lambda / L$, where λ is the incident wavelength, and L is the length of each single ramp period. Ideally, the steering efficiency, η, of a grating with a stair-step blaze, for the first order can be given by:

$$\eta = \sin c^2(\pi / q), \qquad (1)$$

where q is the number of stairs in each repetitive ramp. For example, for an 8-stair ramp, the maximum diffraction efficiency can be around 95%. However, in real devices, practical factors such as fly-back region formation[1-4] resulting from fringe fields can make the final phase profile deviate from the desired one, thus practical steering efficiency from such a LC based device is reduced.

The modeling and mechanisms of such LC based beam steering devices have been extensively investigated, such as combining LC director calculation by finite difference method and optical modeling by finite difference in time domain[2]. And both publications and real experiments show that besides the reduced diffraction efficiency, there is also a diffraction asymmetry[5, 6]. However, the connection between these modeling efforts and methods to improve both the efficiency and diffraction symmetry was not made. In our work, we will first discuss the modeling of the beam steering device, i.e., a spatial light modulator, then analyze the formation mechanism of disclinations in high-low-voltage-transition regions, and finally corresponding methods are proposed to suppress the disclinations and enhance both efficiency and symmetry.

4. 1. Modeling of Spatial Light Modulator

4. 1. 1. Director Simulation

The detailed director calculation has been discussed in Chapter 2, which is based on the Continuum theory[7]. The equilibrium LC director configuration is obtained by minimizing the Gibbs free energy in the presence of external electrical fields.

4. 1. 2. Beam Propagation Method Simulation

Provided the LC director configuration is given, the diffraction of this device is calculated by the beam propagation method (BPM)[8]. BPM is a highly successful tool for the numerical simulations of guided wave optics, where two required approximations of BPM, paraxiality and slow refractive-index variation, can be justified in the guiding nature of these guided wave optical structures. However, for the simulation of LC optics, it lacks a strong light-guiding mechanism and the LC director reorientation in the transverse and longitudinal directions are usually rapid, resulting in a complex interaction between the dielectric tensor and field components. Therefore, the contribution of all dielectric tensor elements for the LC optics needs to be retained. On the other side, based on the Padé rational approximations[8, 9], the paraxiality assumption that limits the incident angle of the beam can be solved within a large range of incident angles. Kriezis and Elston extended the conventional BPM for the calculations of liquid crystal devices to an angle about 30^{o} in the glass substrate (about 50^{o} in the free space)[8], which makes this BPM preferable for SLM simulations.

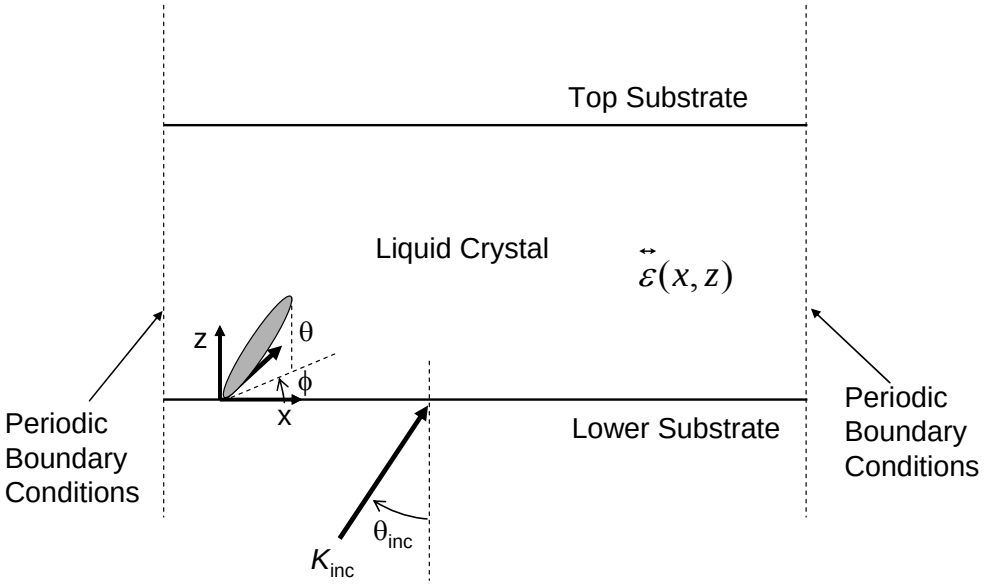

Figure 4.3: Schematic of the simulation system.

For the spatial light modulator structure in Fig. 4.2, it is a two-dimensional structure, that can be depicted in the following coordinate and certain operation satisfies ($\frac{\partial}{\partial y} = 0$). Under such a configuration, the BPM starts with the solving of the following Maxwell's curl equations:

$$\nabla \times \mathbf{E} = j\omega \overleftrightarrow{\varepsilon} \mathbf{H}, \tag{2}$$

$$\nabla \times \mathbf{H} = j\omega u_0 \mathbf{E}, \tag{3}$$

Where the tensor $\overleftrightarrow{\varepsilon}$ has the following form:

$$\overleftrightarrow{\varepsilon} = \begin{bmatrix} n_o^2 + \Delta\varepsilon_r \cos^2\theta\cos^2\phi & \Delta\varepsilon_r \cos^2\theta\sin\phi\cos\phi & \Delta\varepsilon_r \sin\theta\cos\theta\cos\phi \\ \Delta\varepsilon_r \cos^2\theta\sin\phi\cos\phi & n_o^2 + \Delta\varepsilon_r \cos^2\theta\sin^2\phi & \Delta\varepsilon_r \sin\theta\cos\theta\sin\phi \\ \Delta\varepsilon_r \sin\theta\cos\theta\cos\phi & \Delta\varepsilon_r \sin\theta\cos\theta\sin\phi & n_o^2 + \Delta\varepsilon_r \sin^2\theta \end{bmatrix}. \tag{4}$$

With the relation of $\frac{\partial}{\partial y} = 0$, they can be further expanded into six coupled equations. From these

six equations, we can obtain two coupled partial equations that involve only the transverse electric and magnetic field components (E_y and H_y) as follows:

$$\frac{\partial^2 E_y}{\partial x^2}+\frac{\partial^2 E_y}{\partial z^2}+k_0{}^2(\varepsilon_{yy}-\varepsilon_{yz}\frac{b}{a}-\varepsilon_{yx}\frac{c}{a})E_y-\frac{j\omega u_0}{a}(b^*\frac{\partial H_y}{\partial x}-c^*\frac{\partial H_y}{\partial z})=0\,, \tag{5}$$

$$\begin{aligned}&j\omega\varepsilon_0[\frac{\partial}{\partial z}(\frac{c}{a})-\frac{\partial}{\partial x}(\frac{b}{a})]E_y+j\omega\varepsilon_0[(\frac{c}{a})\frac{\partial E_y}{\partial z}-(\frac{b}{a})\frac{\partial E_y}{\partial x}]+\\&\frac{\varepsilon_{xx}}{a}\frac{\partial^2 H_y}{\partial x^2}+\frac{\varepsilon_{zz}}{a}\frac{\partial^2 H_y}{\partial z^2}+2\frac{\varepsilon_{xz}}{a}\frac{\partial^2 H_y}{\partial x\partial z}+\\&[\frac{\partial}{\partial x}(\frac{\varepsilon_{xx}}{a})+\frac{\partial}{\partial z}(\frac{\varepsilon_{xz}}{a})]\frac{\partial H_y}{\partial x}+[\frac{\partial}{\partial z}(\frac{\varepsilon_{zz}}{a})+\frac{\partial}{\partial x}(\frac{\varepsilon_{zx}}{a})]\frac{\partial H_y}{\partial z}+k_0^2H_y=0\end{aligned}\,, \tag{6}$$

where $a=\varepsilon_{xx}\varepsilon_{zz}-\varepsilon_{zx}\varepsilon_{xz}$, $b=\varepsilon_{xx}\varepsilon_{zy}-\varepsilon_{zx}\varepsilon_{xy}$, $c=\varepsilon_{xy}\varepsilon_{zz}-\varepsilon_{zy}\varepsilon_{xz}$, $b^*=\varepsilon_{yz}\varepsilon_{xx}-\varepsilon_{yx}\varepsilon_{xz}$, and $c^*=\varepsilon_{yx}\varepsilon_{zz}-\varepsilon_{yz}\varepsilon_{zx}$.

According to a common procedure of BPM, the field components E_y and H_y can be assumed to be represented by a product of a fast varying reference phase term and a spatial filed envelope as

$$E_y=\mathcal{E}_y(x,z)\exp(-jk_{ref}z)\,, \tag{7}$$

$$H_y=\mathcal{H}_y(x,z)\exp(-jk_{ref}z)\,. \tag{8}$$

Replacing these two forms into the above coupled equations, we can obtain a parabolic form coupled equations of $\mathcal{E}_y$ and $\mathcal{H}_y$. We can apply the Padé recurrence relation to approximate the parabolic forms by first-order differential equations with respect to the axial z-direction (they are still second-order differential equations in the transverse x-direction) without losing accuracy within a large angle. Finally, by applying the Nicolson finite-difference scheme[5] to simply to differential forms in both x- and z-directions and combing all the discrete node components,

these two coupled equations on the spatial envelopes can be converted into a matrix form:

$$\begin{bmatrix} [M_{11}] & [M_{12}] \\ [M_{21}] & [M_{22}] \end{bmatrix} \begin{bmatrix} \mathcal{E}_y^{r+1} \\ \mathcal{H}_y^{r+1} \end{bmatrix} = \begin{bmatrix} [B_1] \\ [B_2] \end{bmatrix}. \tag{9}$$

In addition, as to remove the pseudo reflections on the boundaries at the transverse directions and considering the natural properties of a LCD device, periodic boundary condition (PBC) is a good choice[5].

Once the near field out of the top LC surface, we can apply the Floquet analysis to conduct Fourier transformation to analyze its far field diffraction patterns. More specifically, the calculated near field F can be expanded by a series of distinct fields:

$$\begin{aligned} F &= \sum_{-\infty}^{+\infty} F_m \exp(-jk_x^m x)\exp(-jk_z^m z) \\ k_x^m &= k_x^0 + \frac{2\pi m}{L} \\ (k_z^m)^2 + (k_x^m)^2 &= k^2 \end{aligned} \quad . \tag{10}$$

Therefore, we can determine its corresponding diffraction angle and intensity for each non-evanescent mode.

4. 2. Numerical Examples

4. 2. 1. Conventional Driving of SLM

A multi-electrode SLM with 5 μm electrode width and 1 μm electrode gap as shown in Fig. 4.2 is taken as a numerical example. Here the surface pretilt angle is 7^o and the rubbing direction is at 45^o with respect to the x-axis. The LC material is UCF-2 with its elastic constants K_{11}=13.9 pN and K_{33} =37.8 pN, dielectric constants $\varepsilon_{//}$ = 13.4 and $\varepsilon_{\perp}$ = 3.3, and Δn=0.319 at

λ=1.064 μm. The desired voltage on each electrode is determined by an iteration procedure. Their preliminary values can be determined by matching the phase change value from a 1D LC phase modulator from 1D program with that from the following equation

$$phase(m) = const. + \frac{2\pi \cdot \mathrm{mod}(m, N)}{N}. \quad (11)$$

Here *m* is the number index of each electrode, *N* is the total number of electrodes in one period, and const. is the initial phase value. For example, for a 12-electrode SLM, its initial phase value can be set as 1/6π, and the phase values are from 1/6π to 2π with an increasing step of 1/6π.

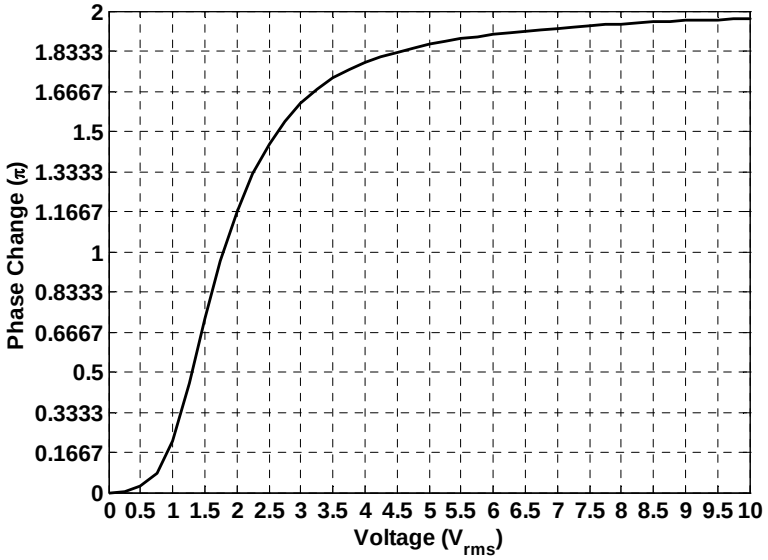

Figure 4.4: Voltage dependent phase change profile

Figure 4.4 depicts the calculated voltage-dependent phase change curve for a 3.6 μm LC cell with abovementioned cell configuration. From this figure we can obtain a preliminary voltage profile for this device, which is listed in the following Table 1. Here we intentionally put

the electrode with the highest voltage ($10V_{rms}$) in the middle of the period for a better study of the associated disclinations nearby.

Table 1: Preliminary voltage profile by 1D LC simulator

Index m	6	7	8	9	10	11	12	1	2	3	4	5
Volts (V_{rms})	2.0	2.3	2.7	3.2	4.5	10	0.9	1.1	1.3	1.5	1.6	1.8

However, due to the interaction between adjacent electrodes, the phase profile deviate from its optimum value severely if the above simplified voltage profile is employed. Figure 4.5(a) shows the calculated position dependent phase change profile using 2D simulator with above voltages. It can be seen that there is a distorted region near the high voltage electrode where its x = ~30 μm, which comes from the reverse tilt of LC directors (Fig. 4.5(b)). Both the distorted phase region and fly-back region at about 36 μm result in a reduced diffraction efficiency that is only about 75% at its first diffraction order that is about -0.84^{o} (Fig. 4.5(c)).

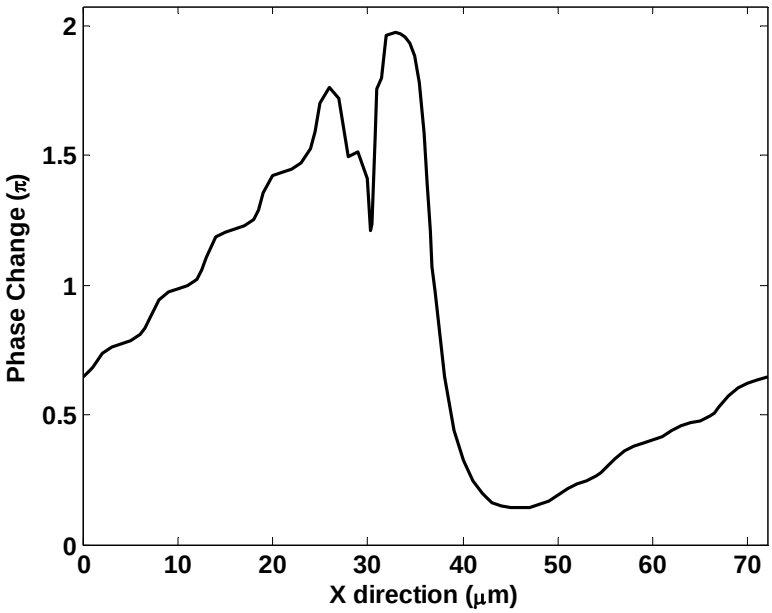
Phase Change (π)
X direction (μm)
0
0.5
1
1.5
2
0
10
20
30
40
50
60
70

(a)

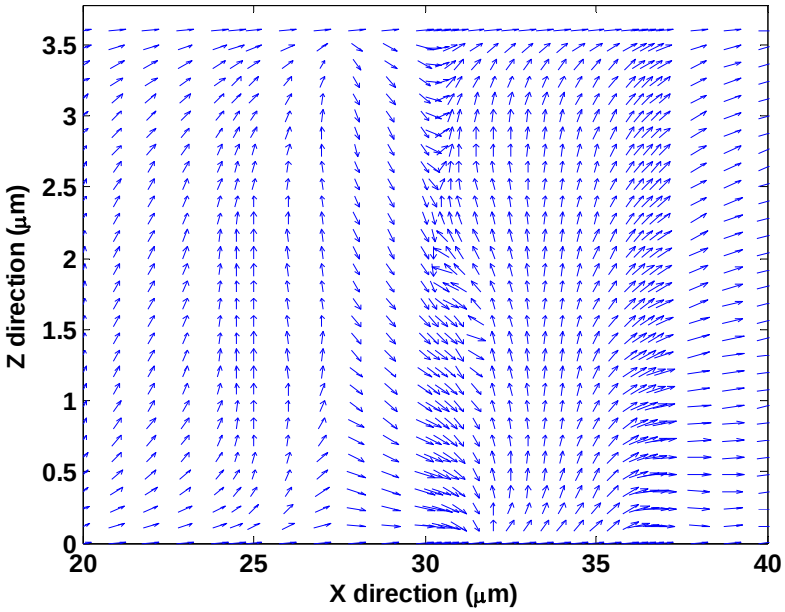
Z direction (μm)
X direction (μm)
0
0.5
1
1.5
2
2.5
3
3.5
20
25
30
35
40

(b)

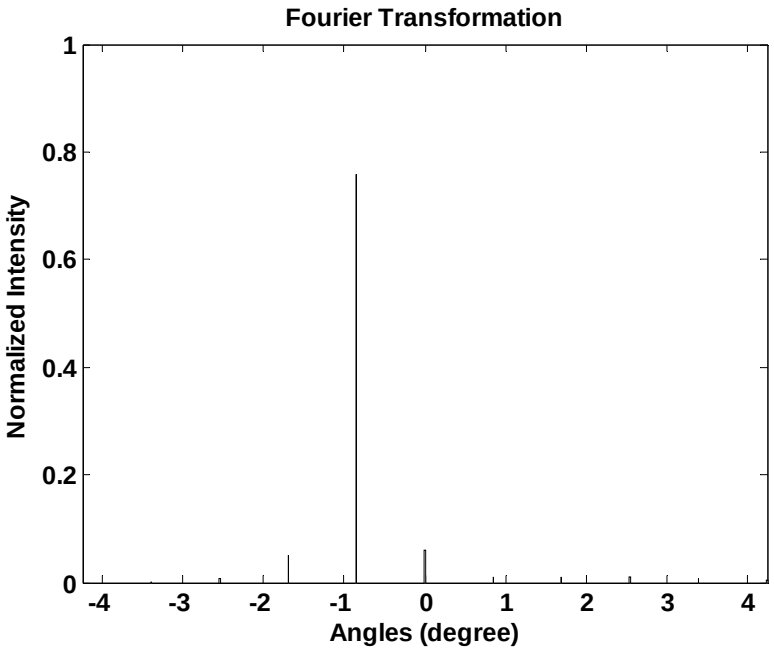

(c)

Figure 4.5: (a) Phase profile, (b) LC director profile, and (c) diffraction pattern

We can further increase the diffraction efficiency by adjusting the voltage on each electrode. The update procedure for an optimized efficiency can be described as follows in Fig. 4.6.

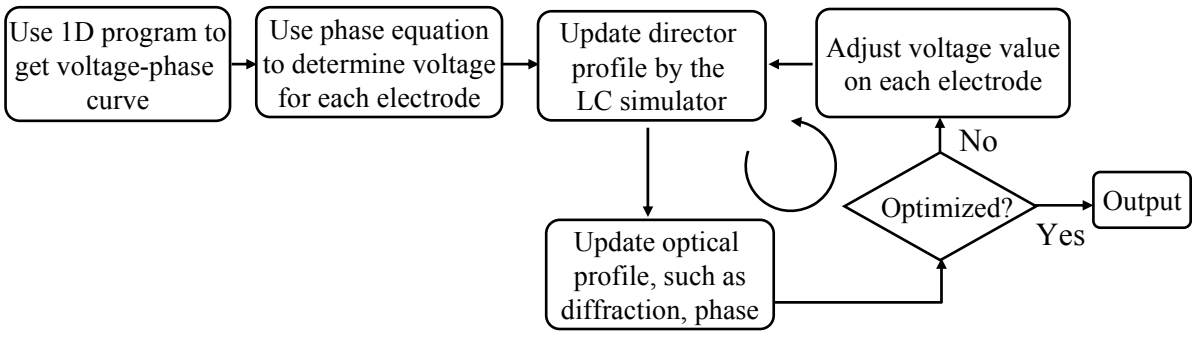

Figure 4.6: LC director optimization flowchart for SLM

With this process, we can obtain a voltage profile listed in Table 2 for optimized diffraction. The new results are shown from Figs. 4.7 (a) to (c), and its maximum diffraction efficiency is boosted up to about 89%. As we can see from the director distribution in Fig. 4.7(b), a reverse tilt region occurs at x= ~29 μm, which generates a kink in the phase profile near that region, but is much weaker than the previous case.

Table 2: Voltage profile by the optimization flow chart

Index m	6	7	8	9	10	11	12	1	2	3	4	5
Volts (V_{rms})	2.4	2.7	3.1	3.65	5.4	10	0.0	1.4	1.6	1.8	2.0	2.2

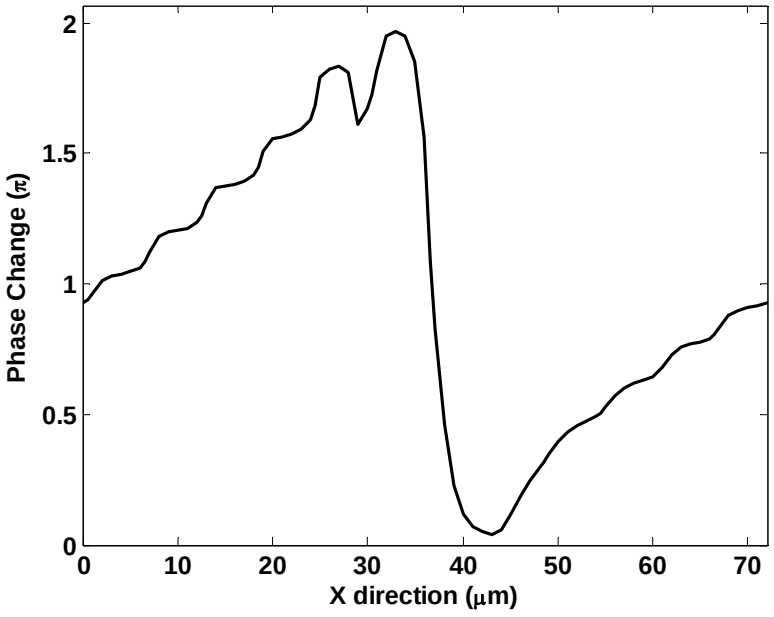

(a)

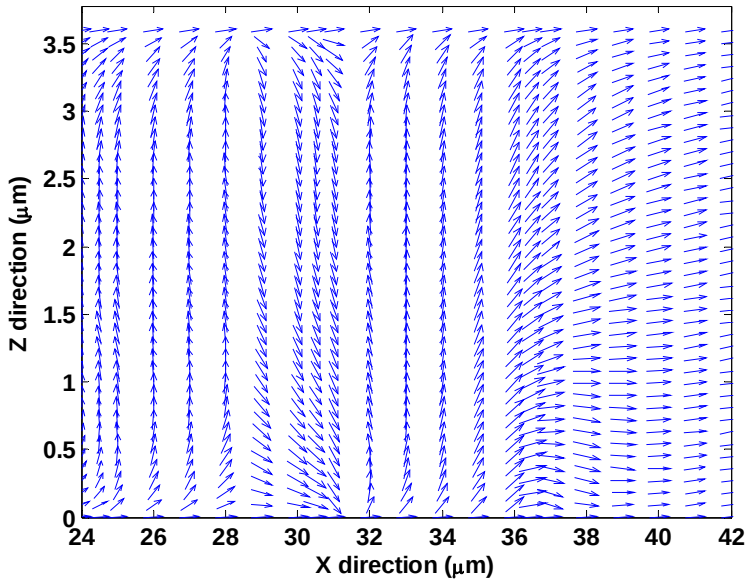

(b)

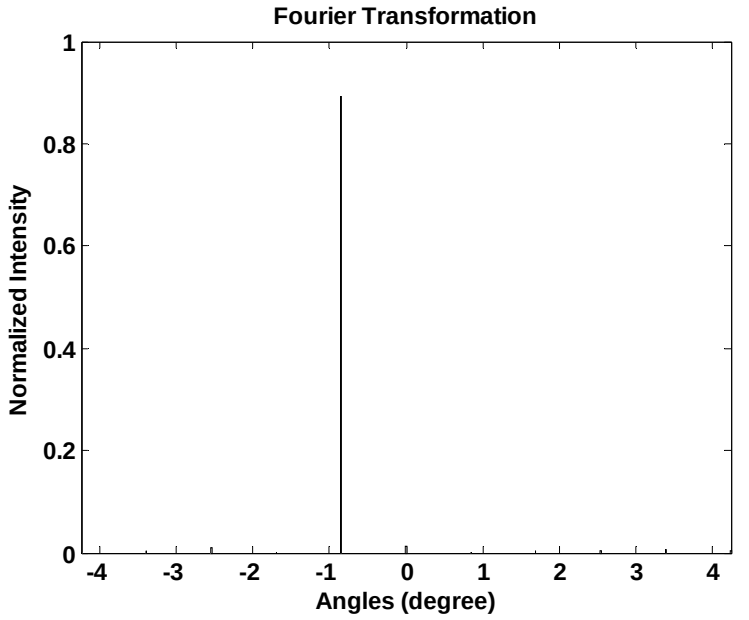

(c)

Figure 4.7: (a) Phase profile, (b) LC director profile, and (c) diffraction pattern of a 12-electrode SLM

Table 3: Optimized diffraction pattern

Angle(deg.)	-1.27	-1.02	-0.85	-0.73	-0.64	0	0.64	0.73	0.85	1.02	1.27
Intensity	0.80	0.86	0.89	0.91	0.92	1.0	0.92	0.91	0.90	0.87	0.82
$Re(E_{\perp}/E_{//})$	0.96	0.94	0.94	0.91	0.91	1.0	0.82	0.81	0.80	0.79	0.78

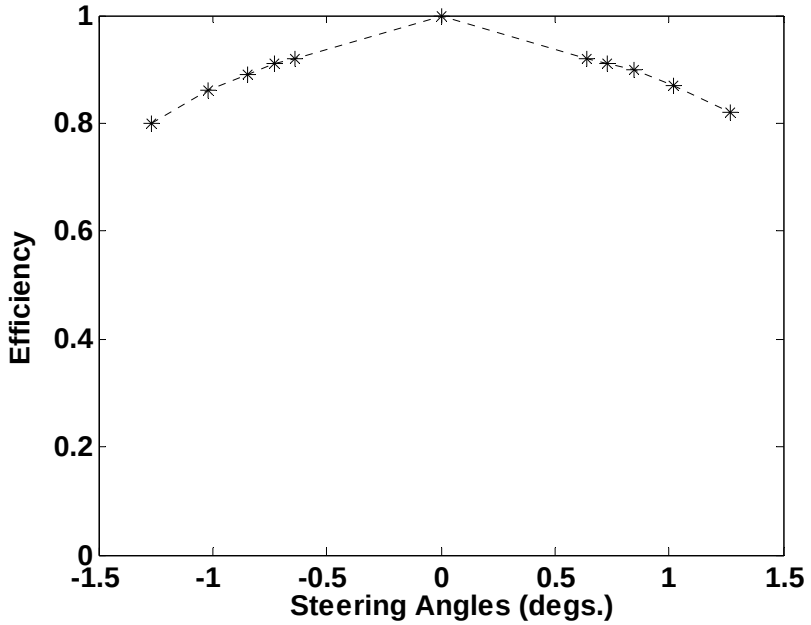

Figure 4.8: Angular diffraction pattern

Following this scheme, we can calculate the different diffraction patterns of SLMs with 8- to 16 electrodes. Results are summarized in Table 3 and Fig. 4.8. From Fig. 4.8, the diffraction (especially the output polarization) is not symmetric between positive and negative directions. The 7^{o} pretilt angle accounts for this asymmetry. Figures 4.9(a) and 4.9(b) show the phase and

director profiles of a 12-electrode SLM steering at a positive angle. As we can see from the phase profile, there is a "touch down" region near the maximum voltage electrode. This "touch down" in the phase profile results from an unperturbed region of LC directors (at x ~24 μm), as shown in Fig. 4.9(b). Compared to the negative diffraction case, the region with phase change close to zero is larger for the positive diffraction case, which mainly comes from the direction of the surface pretilt angle. As a result, its polarization direction deviates more from its original one than that of negative case.

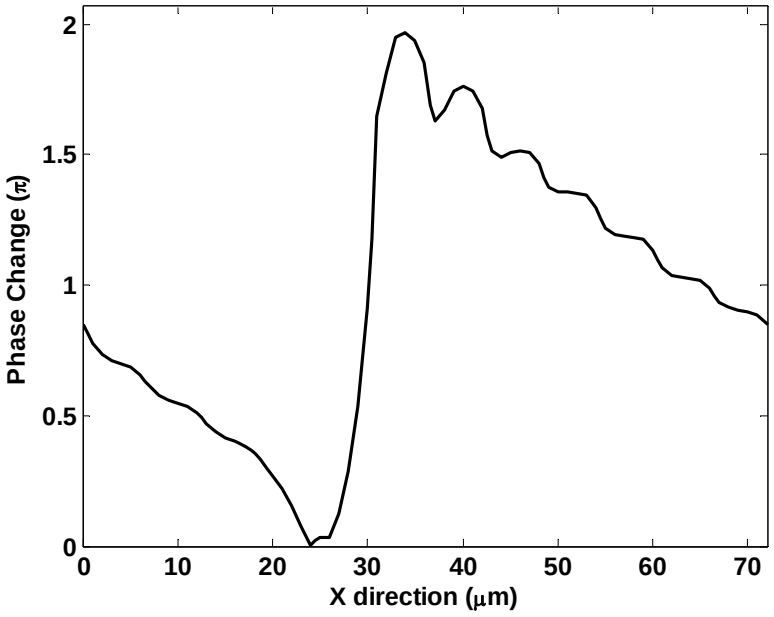

(a)

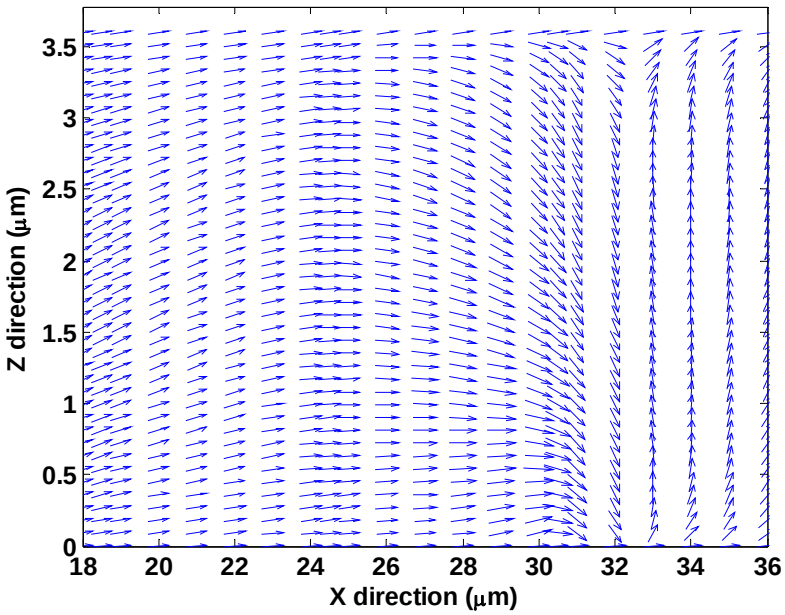

(b)

Figure 4.9: (a) Phase profile and (b) LC director profile

4. 2. 2. Pre-Driving of SLM

From above analysis, we can see that the strong fringe fields near the maximum voltage electrode, causing evident disclinations of LC molecules there that account for the formation of fly-back region and diffraction efficiency reduction. In the real beam steering systems, usually more than one SLM will be cascaded for omni-directional steering. Therefore the efficiency of a single is SLM is critical.

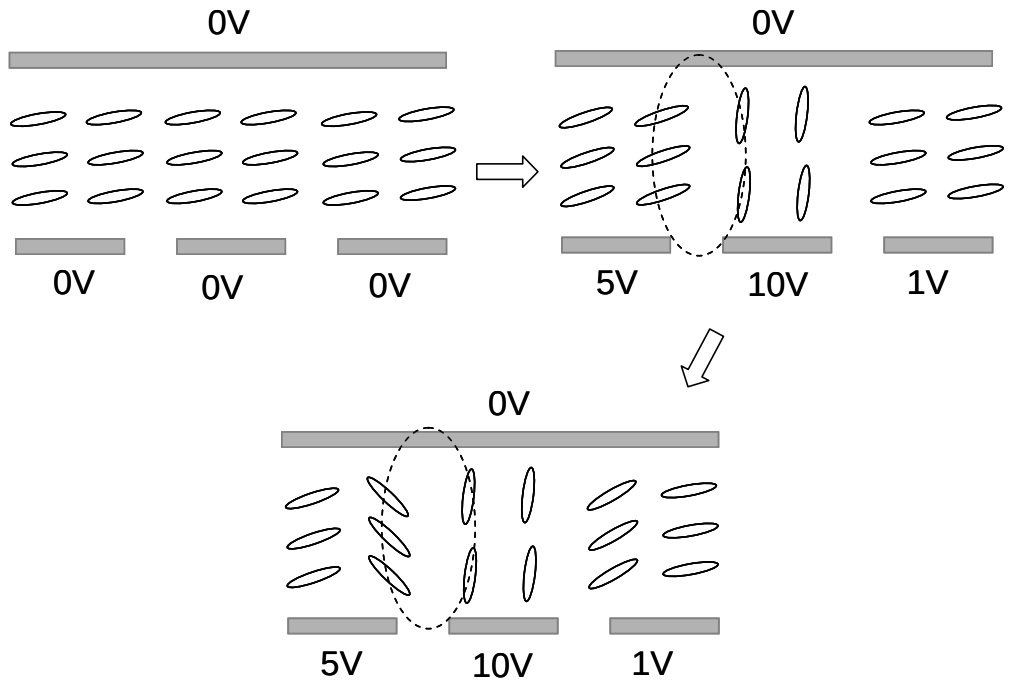

Figure 4.10: Dynamic LC director deformation under conventional driving method

This dynamic formation of LC disclinations strongly depends on the start-up LC distributions. Figure 4.10 illustrates the mechanism that works for the disclination formation under a conventional driving scheme. Initially, all the LC molecules are homogeneously aligned with certain pretilt angle. Once the voltage profile is applied to the electrodes, the LC molecules above the 10 V_{rms} electrode respond most quickly to become instantly vertically aligned. But those molecules above low voltage electrodes nearby retard from them and a transition region with abrupt molecular orientations forms, which produces disclination cores there. While the voltage is held on the electrode, the LC molecules near this region form a reverse tilt pattern.

From above analysis, we can see that the formation of disclinations mainly originates

from the abrupt transition region that comes from the large voltage difference thereby. Here we propose a new driving scheme for this problem, which applies a pre-driving high voltage to all the electrodes for a very short time, and then goes back to another desired voltage profile thereafter. The mechanism is illustrated in the Fig. 4.11. By this driving scheme, when a high voltage, like 10 V_{rms}, is applied to all electrodes for a very short time, all the LC molecules will tilt up. Since the time for this pulse is very short, it will not make all the LC molecules tilt fully up. Then when the final profile is added, the start-up difference in the circle at the border of the electrodes with 5 V_{rms} and 10 V_{rms} is reduced. As a result, the core for disclination formation is removed, and further development of LC molecules under voltages will guide them to a more reliable voltage profile.

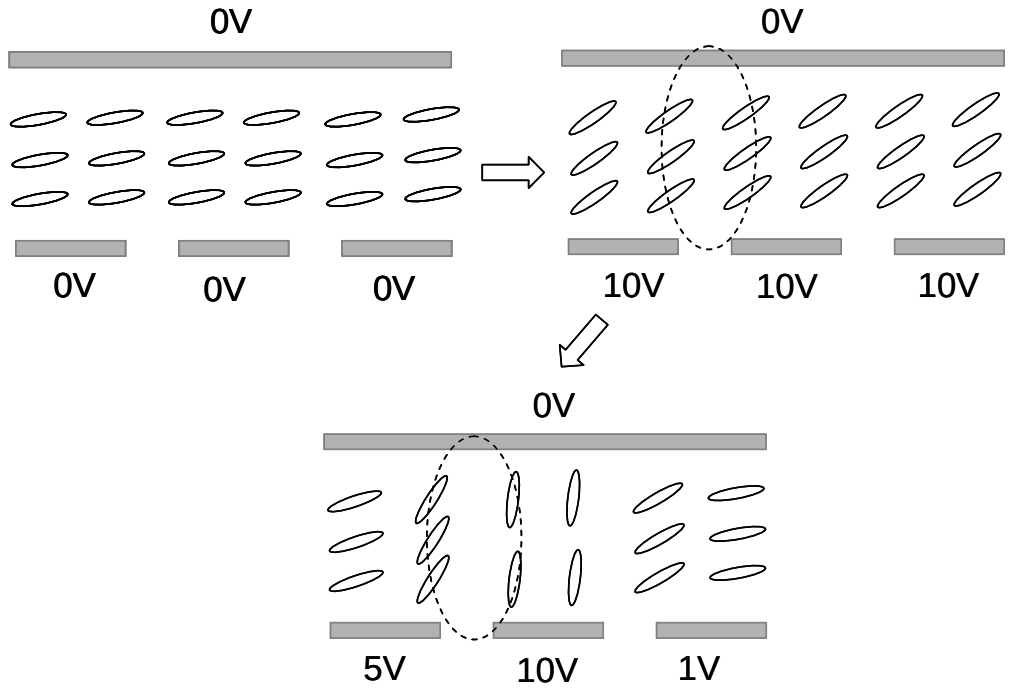

Figure 4.11: Dynamic LC director deformation under pre-driving method

For example, if T_{pre}= 0.5 ms, the newly calculated diffraction pattern for SLMs with 8- to 16 electrodes are shown in Table 4 and Fig. 4.12. From these data, it can be observed that the diffraction efficiency increases for the both directions at large angles, where the disclination is severer. Figures 4.13(a) and (b) show the director distributions of an 8-electrode SLM from both the conventional driving method and the pre-driving method. Under the pre-driving method, the LC molecules do undergo a different reorientation, generating a smaller reverse tilt region in the phase profile that comes from a weaker reverse tilt region (comparing the Figs. 4.13(a) and (b)). This can also be seen from the phase profiles plotted in Fig. 4.13(c). Thus diffraction efficiency is improved. Here this pre-driving method has evident impacts for the large deflection angles, where the ratio of reverse tilt region impacts more than those with a large period. In addition, the pre-driving time and voltage can be adjusted according to different diffraction angles.

Table 4. Diffraction pattern from pre-driving method

Angle(deg.)	-1.27	-1.02	-0.85	-0.73	-0.64	0	0.64	0.73	0.85	1.02	1.27
Intensity	0.84	0.88	0.90	0.92	0.93	1.0	0.93	0.92	0.92	0.89	0.86
$Re(E_{\perp}/E_{//})$	0.98	0.96	0.94	0.92	0.91	1.0	0.81	0.80	0.79	0.79	0.78

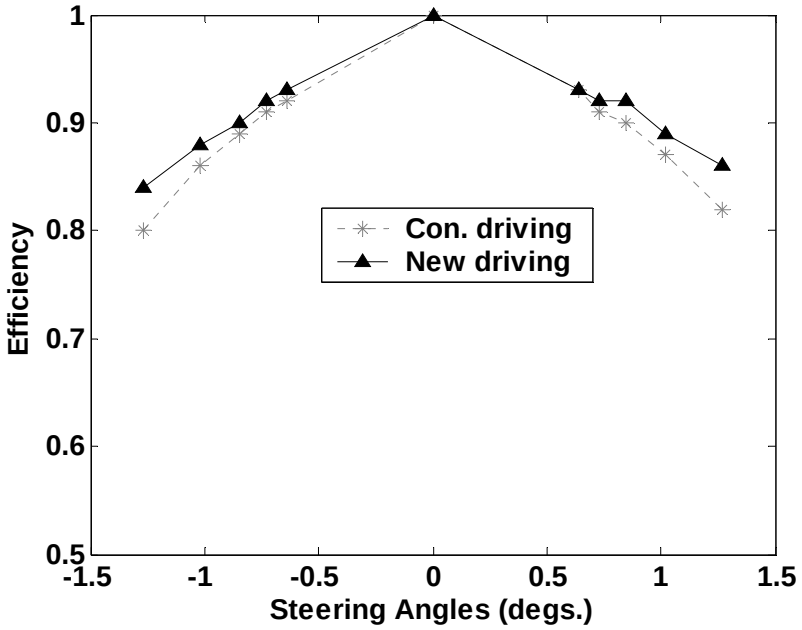

Figure 4.12: Angular diffraction pattern

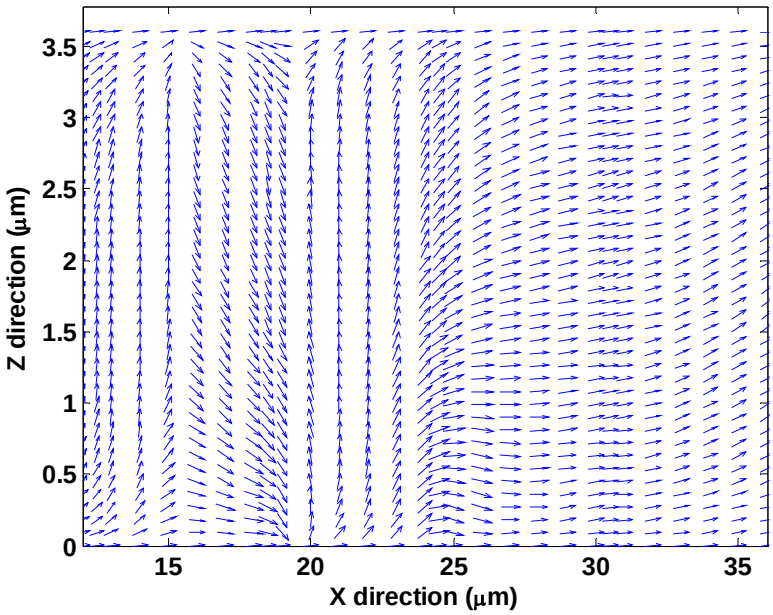
Z direction (μm)
X direction (μm)
0
0.5
1
1.5
2
2.5
3
3.5
15
20
25
30
35

(a)

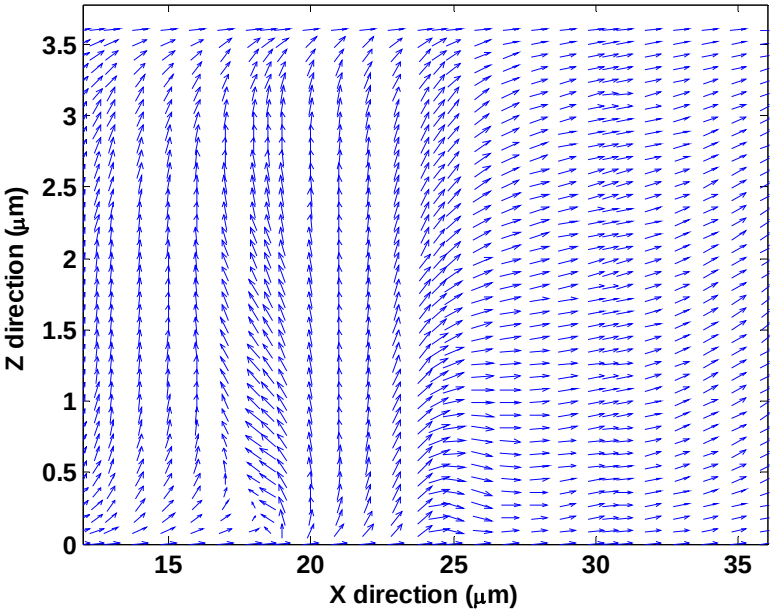
Z direction (μm)
X direction (μm)
0
0.5
1
1.5
2
2.5
3
3.5
15
20
25
30
35

(b)

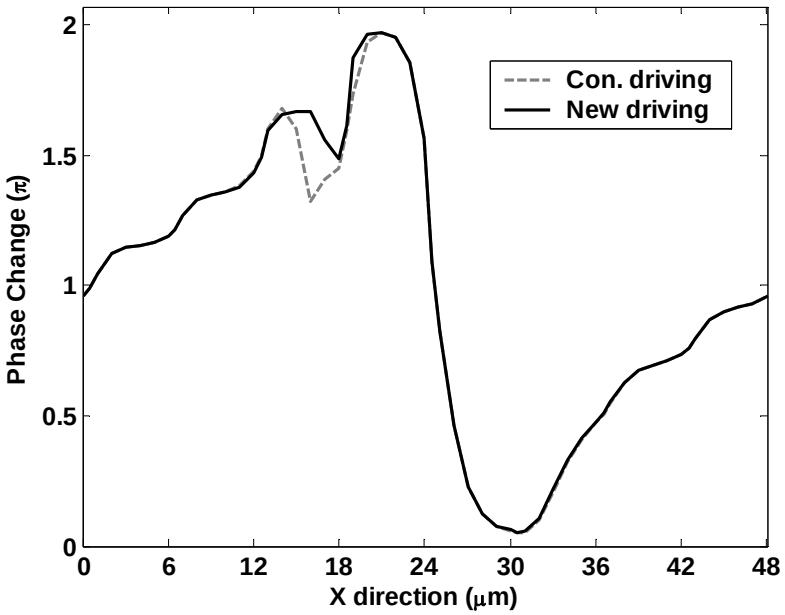

(c)

Figure 4.13: LC molecule distribution from (a) conventional driving method, (b) new driving method, and (c) phase profiles from both methods for an 8-electrode SLM.

4. 3. Summary

We have successfully developed a modeling for multi-electrode SLM structures using nematic LC materials. The optical performance and its underlying physics are studied to make a better understanding the roots of the low diffraction. We propose a new driving method that employs a short-pulse to universally pre-perturb the whole device which reduces the chances of forming disclinations, thus enhances the diffraction efficiency dramatically. The cost of this method is a simple pre-driving controller for every diffraction angle.

4. 4. References

1. T. A. Dorschner and D. P. Resler, “Deflector for an optical beam,” US Pat. No. 4,964,701, (Oct. 1990).
2. T. A. Dorschner et al, “Liquid crystal beam steerig: an optical phase array for lasers,” presented at the *1991 Meet. IRIS Specialty Group on Active Syst.*, (Oct. 1991).
3. D. P. Resler, D. S. Hobbs, R. C. Sharp, L. J. Friedman, and T. A. Dorschner, “High-efficiency liquid-crystal optical phased-array beam steering,” Opt. Lett. 21, 689 (1996).
4. P. F. McManamon, T. A. Dorschner, D. L. Corkum, L. J. Friedman, D. S. Hobbs, M. Holz, S. Liberman, H. Q. Nguyen, D. P. Resler, R. C. Sharp, and E. A. Watson, "Optical phased array technology," Proc. IEEE 84, 268-298 (1996).
5. X. Wang, B. Wang, P. J. Bos, J. E. Anderson, J. J. Pouch, and F. A. Miranda, "Finite-difference time-domain simulation of a liquid-crystal optical phased array," J. Opt. Soc. Am. A 22, 346-354 (2005).
6. C. M. Titus, J. R. Kelly, E. C. Gartland, S. V. Shiyanovskii, J. A. Anderson, and P. J. Bos, "Asymmetric transmissive behavior of liquid-crystal diffraction gratings," Opt. Lett. 26, 1188-1190 (2001).
7. P. G. De Gennes and J. Prost, “The Physics of Liquid Crystals” (Oxford Press, Oxford, UK, 1993).
8. E. E. Kriezis and S. J. Elston, "Wide-Angle Beam Propagation Method for Liquid-Crystal Device Calculations," Appl. Opt. 39, 5707-5714 (2000).
9. G. R. Hadley, “Wide-angle beam propagation using Padé approximant operators,” Opt. Lett. 17, 1426–1428 (1992).

CHAPTER 5: SUMMARY

In this thesis, we have discussed the modeling of liquid crystal devices for display and beam steering applications. Generally, the modeling consists of two procedures: 1) calculation of LC directors' distribution under certain external voltages, and 2) calculation of the optical performance thereafter. The LC director deformation is modeled by minimizing the system's Gibbs's free energy, which is a combination of the LC elastic energy and the electric energy. However due to the complicated equations associated with these energy forms, people usually take approximations in these equations for simplification. Therefore, the modeling of LC dynamic behavior lacks accuracy. Better modeling methods and the related numerical derivation are highly preferable. In our studies, we have employed the finite element method and finite difference method to solve this problem. With the assistance of computer-aided derivation (such as from MAPLE software), full forms of the energy equations can be obtained without any simplification. Besides, we also introduced the Galerkin's method and weak form technique into our modeling, which successfully degrades the high order non-linear derivative terms in the energy equations into forms that are treatable by first order interpolation function. As a result, the accuracy of the modeling is improved. And numerical examples of this part are also provided and discussed.

In addition, once the LC deformation is obtained, optical methods for charactering the associated electro-optical properties are also investigated according to the unique characteristics of different devices. For example, for liquid crystal display devices, the LC cell usually works as an amplitude modulator, and the change of polarization of the incident light throughout the

display system is of prior importance. We studied and developed matrix based methods, such as new Jones matrix method for these kinds of devices, which can be further taken to trace the polarization change of the light. On the other hand, for beam steering devices, the LC cell functions as a phase modulator and the change of phase profile in such devices are critical. Accordingly, we studied and employed the beam propagation method that can account for the spatial LC molecular variation and Fourier transformation techniques to calculate the near and far fields of such kind of diffractive devices.

Afterwards, these numerical modeling methods are employed to better understand and develop new LC devices and systems. For display part, several transflective LCD devices and their related optical compensation films for wide viewing angle are developed and studied. In transflective LCDs, high light efficiency and wide viewing angle are two critical requirements. One example we developed and studied is a single cell gap transflective LCD configuration that employs commonly biased reflectors in the cell to match the optical path for the transmissive and reflective regions. This display shows a high light efficiency and a good match between the VT and VR curves, which can be driven by a single gray scale control circuit. For the wide viewing angle, we developed a transflective LCD structure using a wide viewing angle FFS cell and internal wire grid polarizer as the reflector. This device works under only two linear polarizers and the wire grid polarizer works as a polarization dependent reflector that makes a single cell gap workable in this device. Another approach for wide viewing angle is developing better circular polarizers. We employed the Poincaré sphere as an effective tool to understand of the change of polarization of light through the structures and guide new designs. From our study, we proposed using alternating birefringence uniaxial A-plates in broadband circular polarizers to

suppress the light leakage from off-axis directions. Besides, we also introduced biaxial film into the circular polarizers along with a partially compensated VA LC cell to minimize the light leakage at all viewing directions. Our results show that this circular polarizer can obtain the comparable viewing angle properties for MVA cells as they are used between two linear polarizers, while using circular polarizers can greatly boost the brightness and can also obtain workable reflective modes in transflective LCDs. Finally, the developed LC deformation methods and beam propagation method for optical characterization are employed to study the spatial light modulator structure using LC materials. The modeling helps to better understand the origins and formations of the disclinations associated with the fringe fields, which further result in reduced steering efficiency and output asymmetric polarizations between positive and negative diffractions. Besides the understanding of the physics underneath, our proposed new driving methods to guide the orientation of LC molecules successfully boosted the diffraction efficiency.

This study covers a wide range of LC device modeling. The developed methods greatly assist us to better understand the physics of LC devices, optimize their performance, and design new ones. We believe our work has a big impact in the display and photonics areas.